



Retrieval of microphysical cloud properties:
a novel algorithm for decomposing
cloud radar spectra.

Sabrina Melchionna



Hinweis

Die Berichte zur Erdsystemforschung werden vom Max-Planck-Institut für Meteorologie in Hamburg in unregelmäßiger Abfolge herausgegeben.

Sie enthalten wissenschaftliche und technische Beiträge, inklusive Dissertationen.

Die Beiträge geben nicht notwendigerweise die Auffassung des Instituts wieder.

Die "Berichte zur Erdsystemforschung" führen die vorherigen Reihen "Reports" und "Examensarbeiten" weiter.



Notice

The Reports on Earth System Science are published by the Max Planck Institute for Meteorology in Hamburg. They appear in irregular intervals.

They contain scientific and technical contributions, including Ph. D. theses.

The Reports do not necessarily reflect the opinion of the Institute.

The "Reports on Earth System Science" continue the former "Reports" and "Examensarbeiten" of the Max Planck Institute.

Anschrift / Address

Max-Planck-Institut für Meteorologie
Bundesstrasse 53
20146 Hamburg
Deutschland

Tel.: +49-(0)40-4 11 73-0
Fax: +49-(0)40-4 11 73-298
Web: www.mpimet.mpg.de

Layout:

Bettina Diallo, PR & Grafik

Titelfotos:

vorne:

Christian Klepp - Jochem Marotzke - Christian Klepp

hinten:

Clotilde Dubois - Christian Klepp - Katsumasa Tanaka

Retrieval of microphysical cloud properties:
a novel algorithm for decomposing cloud radar spectra

Sabrina Melchionna

aus Bari, Italien

Hamburg 2011

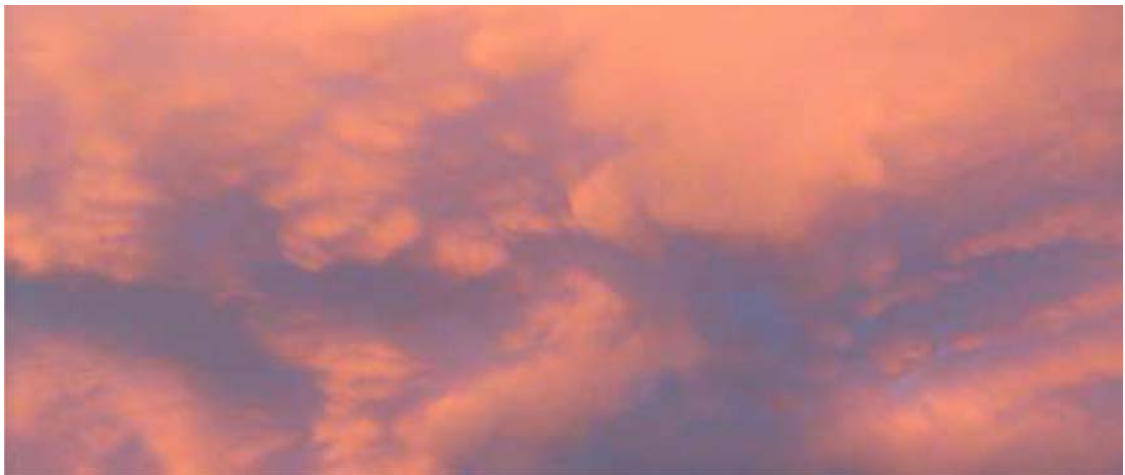
Sabrina Melchionna
Max-Planck-Institut für Meteorologie
Bundesstrasse 53
20146 Hamburg
Germany

Als Dissertation angenommen
vom Department Geowissenschaften der Universität Hamburg

auf Grund der Gutachten von
Prof. Dr. Bjorn Stevens
und
Dr. Gerhard Peters

Hamburg, den 1. Juli 2011
Prof. Dr. Jürgen Oßenbrügge
Leiter des Departments für Geowissenschaften

Retrieval of microphysical
cloud properties:
a novel algorithm for decomposing
cloud radar spectra



Sabrina Melchionna

Hamburg 2011

Cover picture sources

Clouds over home at Christmas sunset, S. Melchionna

Contents

| | |
|----------------------------------------------------------------|-----------|
| Abstract | 1 |
| 1 Motivation | 3 |
| 2 Description of cloud microphysics | 7 |
| 2.1 Introduction | 7 |
| 2.2 Warm-clouds microphysics | 10 |
| 2.2.1 Droplets formation | 10 |
| 2.2.2 Droplets growth by condensation | 10 |
| 2.2.3 Droplets growth by coalescence | 10 |
| 2.3 Cold-clouds microphysics | 11 |
| 2.3.1 Ice crystals formation - primary nucleation | 11 |
| 2.3.2 Ice crystals growth by deposition | 12 |
| 2.3.3 Ice crystals growth by collection | 13 |
| 2.4 Mixed-phase cloud microphysics | 14 |
| 2.4.1 Ice crystals formation - secondary nucleation | 14 |
| 2.4.2 Ice crystals growth - ice crystal theory | 15 |
| 2.5 Precipitation | 19 |
| 2.6 Particle size spectra | 19 |
| 2.7 Size, shape and fall velocity of cloud particles | 20 |
| 2.8 Liquid and Ice Water Content | 25 |
| 3 Cloud radars | 27 |
| 3.1 Introduction | 27 |
| 3.2 The radar equation | 28 |
| 3.3 Radar cross section for meteorological targets | 34 |
| 3.3.1 Equivalent reflectivity factor | 39 |
| 3.4 Attenuation | 42 |
| 3.5 Doppler radar | 43 |
| 3.6 Gaussian spectra | 46 |
| 3.7 Polarimetric radar | 47 |
| 3.8 Phase noise | 51 |
| 3.9 Moments of the Doppler spectrum | 53 |
| 3.9.1 The spectral reflectivity factor | 55 |

| | | |
|----------|-----------------------------------------------------------------------------------------|------------|
| 3.10 | Graphical representation of measurements by vertically pointing radar systems | 57 |
| 3.11 | Radar specifications of MIRA-36 | 60 |
| 4 | Development of the decomposition algorithm | 61 |
| 4.1 | Introduction | 61 |
| 4.2 | Overview of the decomposition algorithm | 62 |
| 4.3 | The spectral model | 64 |
| 4.4 | Noise level detection | 67 |
| 4.5 | Fitting procedure | 71 |
| 4.6 | Calibration | 77 |
| 5 | Microphysical retrievals | 79 |
| 5.1 | Introduction | 79 |
| 5.2 | Mixed-phase recognition | 81 |
| 5.3 | Vertical velocity of cloud particles assessed by Doppler radar measurements | 86 |
| 5.4 | Diameter and IWC | 95 |
| 5.5 | Rate of increasing of fall velocity in clouds | 102 |
| 6 | Application of the decomposition algorithm: comparison with model | 107 |
| 6.1 | Introduction | 107 |
| 6.2 | Case study: 7 December 2006 | 109 |
| 6.3 | Acknowledgments | 117 |
| 7 | Summary and Outlook | 119 |
| | Bibliography | 121 |

List of Figures

| | | |
|-----|------------------------------------------------------------------------------------------------------|----|
| 2.1 | Microphysical processes in clouds | 9 |
| 2.2 | Nucleation of ice particles | 11 |
| 2.3 | Basic shapes of ice crystals | 12 |
| 2.4 | Snow crystals morphology diagram | 13 |
| 2.5 | The possible proportions between vapor pressures in mixed-phase clouds | 16 |
| 2.6 | Ice crystal fed by droplets | 17 |
| 2.7 | Holes in clouds | 18 |
| 2.8 | Fall velocity of liquid drops based on their size | 21 |
| 2.9 | Fall velocity of frozen hydrometeors based on their size | 22 |
| | | |
| 3.1 | Basic representation of a radar system | 28 |
| 3.2 | Beam pattern for MIRA-36 | 29 |
| 3.3 | Schematic representation of the interaction process between radar waves and cloud droplets | 31 |
| 3.4 | Normalised radar cross section for liquid and solid water spheres . . | 35 |
| 3.5 | Examples of radar equivalent reflectivity factor for a cirrus and a stratus | 41 |
| 3.6 | Depolarization of waves incident on oblate particles | 48 |
| 3.7 | THI — Example of Signal to Noise Ratio and respective Linear Depolarization Ratio | 50 |
| 3.8 | Gaussian model of the Doppler spectrum | 54 |
| 3.9 | Examples of Time–Height Indicators | 58 |
| | | |
| 4.1 | Flow chart of the decomposition algorithm | 63 |
| 4.2 | Examples of spectra | 64 |
| 4.3 | Uni–modal spectrum | 67 |
| 4.4 | Noise spectrum | 68 |
| 4.5 | Noise profile | 70 |
| 4.6 | Decomposed spectra | 71 |
| 4.7 | Non–plausible modes | 73 |
| 4.8 | Another non–plausible mode | 74 |
| 4.9 | Scatterplots v_{cx} vs. v_{co} | 76 |
| | | |
| 5.1 | Example of a decomposed spectra profile | 83 |
| 5.2 | Time series of decomposed spectra profiles - mixed-phase | 84 |
| 5.3 | Time series of decomposed spectra profiles - turbulence | 85 |

| | | |
|------|------------------------------------------------------------------------------------------------------------|-----|
| 5.4 | Fall velocity | 87 |
| 5.5 | Scatterplots V_D against Z_e | 88 |
| 5.6 | Fall velocity with air vertical motions reductions; case 1 | 89 |
| 5.7 | Fall velocity with air vertical motions reductions; case 2 | 90 |
| 5.8 | Fall velocity with air vertical motions reductions (profile) | 91 |
| 5.9 | Fall velocity with air vertical motions reductions by different time averaging | 92 |
| 5.10 | D_0 vs. V_t relationships for different assumptions of the Particle Size Distribution | 95 |
| 5.11 | Main and secondary mode-specific reflectivity, fall velocity and LDR, 6 th March 2007 | 97 |
| 5.12 | Particle diameters, 6 th March 2007 | 100 |
| 5.13 | IWC, 6 th March 2007 | 101 |
| 5.14 | Example of fitted spectra profile, case 1 | 102 |
| 5.15 | Example of fitted spectra profile, case 2 | 103 |
| 5.16 | Example of fitted spectra profile, case 3 | 104 |
| 5.17 | Example of fitted spectra profile, case 4 | 105 |
| 5.18 | Time series of rate of increasing of fall velocity, 6 th March 2007 | 105 |
| 6.1 | Satellite image over East Europa on the 7 th December 2006 | 109 |
| 6.2 | Mode-specific fall velocity, 7 December 2006 | 110 |
| 6.3 | Mode-specific median volume diameter, 7 December 2006 | 111 |
| 6.4 | Mode-specific IWC, 7 December 2006 | 112 |
| 6.5 | Prediction for the different hydrometeors, 7 December 2006 | 113 |
| 6.6 | Model prediction for fall velocity, 7 December 2006 | 115 |
| 6.7 | Time series of rate of increasing of fall velocity, 7 th December 2006 | 116 |

List of Tables

| | | |
|-----|--------------------------------------------------------------------------|----|
| 2.1 | Characteristic coefficients for the terminal fall velocity of snow . . . | 23 |
| 3.1 | Typical values of equivalent reflectivity factor | 40 |
| 3.2 | Attenuation coefficients at 35 GHz | 42 |
| 3.3 | Typical values of Linear Depolarization Ratio | 49 |
| 3.4 | Specifications for the cloud radar MIRA-36 | 60 |
| 4.1 | What can go wrong during the automatized fitting procedure | 75 |

Abstract

Clouds play a vital role in regulating the climate of Earth. However, there is a lack of understanding on their microphysical properties, as well as on the physical processes responsible for formation, growth, and evolution of cloud particles.

Microphysical properties of clouds can be remotely investigated by using cloud Doppler radars. In order to characterize clouds by Doppler radar measurements, the first three moments of Doppler spectra, nominally reflectivity, Doppler mean velocity, and spectral width, and additionally the Linear Depolarization Ratio (LDR), are widely used. These observables allow radar meteorologists to derive information on particle size, shape, phase, orientation, concentration, and motion.

Traditionally the moments of the Doppler spectra are evaluated considering the spectra due to only one class of particles, i.e. either cloud droplets or ice crystals. But cloud radars have an excellent sensitivity to detect cloud particles and, therefore, they produce complex Doppler spectra which bring information on cloud droplets of different size, ice crystals with different habit and size, or on cloud droplets mixed with ice crystals. Against this potential to investigate clouds, robust techniques for resolving radar Doppler spectra are still not fully developed.

In this work we develop a new operational algorithm with the aim of routinely decompose radar Doppler spectra in their constitutive modes, each mode representing a different class of cloud particles. The rationale of the algorithm is that an ensemble of cloud particles of the same class produces a Gaussian spectrum with characteristic parameters, which are related to the traditional moments of the Doppler spectrum. Ensembles containing different classes of cloud particles produce linearly superposed Gaussian Doppler spectra, whose characteristic parameters are used to evaluate mode-specific moments. The three mode-specific moments and mode-specific LDR are then used to evaluate microphysical parameters of each class.

The algorithm has been developed on measurements taken by the Doppler cloud radar MIRA-36, operating at the frequency of 35.5 GHz and with Doppler velocity resolution of 0.08 m/s. Using these measurements we are able to separate the spectra in up to two dominant classes.

This analysis turned to be particularly useful in the recognition and study of mixed-phase layers, where the detected modes are due to snowflakes and supercooled droplets or snowflakes and ice crystals. The process plausibly occurring is ice secondary nucleation process, that is snowflakes falling through a layer of supercooled droplets splinter into pristine ice crystals.

The potentiality of the method is illustrated by applying it on radar measurements of deep stratiform convective cloud structures, for which a layer of double modes shows up for a persistent lapse of vertical and temporal extension.

Further pieces of information on the properties of the cloud particles are extracted by linearly fitting the main mode-specific velocity as a function of the altitude. The gradient of this fit gives a picture on the growing rate of hydrometeors along the vertical extension of the cloud. Specifically, we have observed a continual constant

increasing of the Doppler velocity on the cloud particles fall path.

The microstructure of mixedphase cloud as retrieved by cloud radar data has been compared for one case study with the results obtained by a configuration of the COSMO-DE model, showing a suitable agreement. As this model configuration includes an explicit cloud microphysical parametrization, the use of radar decomposed spectra in numerical cloud models should be considered for testing the current knowledge of the processes involved and for validation and refinement of numerical cloud models itself.

Chapter 1

Motivation

It is widely recognized that the climate of the Earth is strongly influenced by clouds through their radiative behavior, as assessed in the Intergovernmental Panel on Climate Change 2007 Report (IPCC, 2007).

The magnitude of the influence of clouds on the atmosphere depends on their geometrical properties, such as thickness or vertical and horizontal extension, as well as on their microphysical properties, such as cloud particle size or water content (Stephens et al., 1990).

Whereas geometrical properties are routinely measured by satellites (Stephens et al., 2002) and used to quantitatively represent clouds in atmospheric models (Marchand et al., 2009), the knowledge of the microstructure of clouds, as well as the physical processes responsible for formation, growth, and evolution of cloud particles, is extensive, but still not exhaustive (Cantrell and Heymsfield, 2005; Shupe et al., 2008).

In order to investigate cloud microphysical properties vertically resolved, millimeter, Doppler, polarimetric radar systems - the so-called cloud radars - are preferred because they have an excellent sensitivity to cloud particles (droplets and ice crystals) and at the same time a reasonable low attenuation by rain; they work continuously and unattended; finally they have a compact size and thus can be deployed on different platforms such as ships, satellites, or aircrafts.

Specifically cloud radar systems measure profiles of intensity of the signal backscattered by cloud particles, of their Doppler shift, and eventually the polarimetry of the backscattered radiation. From these measurements it is possible to derive information on particle size, shape, phase, orientation, concentration, and motion.

The basic information given by a cloud radar is then a Doppler spectrum for every time step and for every height step from the radar.

The Doppler spectrum is determined by the scattering cross section of all the particles present in a sampling volume as function of their Doppler velocity.

Conventionally, in order to characterize clouds by Doppler radar measurements, radar meteorologists use the first three moments of Doppler spectra (reflectivity, Doppler mean velocity, spectral width) and the Linear Depolarization Ratio (LDR); the moments of the Doppler spectrum are evaluated considering the spectra due to

only one class of particles.

Unfortunately these “global” moments are not sufficient to describe the complex structure of the spectra. The complexity arises mainly from the variegated collection of particles forming clouds: cloud droplets of different size, ice crystals with different habit and size, or cloud droplets mixed with ice crystals (mixed-phase clouds); moreover, cloud top turbulence influences the radar echoes. Thus, in case of clouds producing such composite Doppler spectra, the extraction of cloud microphysical parameters by using the global moments leads to incomplete, when not erroneous, retrievals.

In this work we consider Doppler spectra received with a cloud radar, to retrieve information on microphysical structure of clouds and dynamics of cloud systems. The shape of the Doppler spectra containing important information on the phase of the observed hydrometeors has been already recognized; however, the separation among the different classes of particles observed in a Doppler spectrum need sophisticated spectral analysis, as described by Shupe et al. (2004), Verlinde et al. (2007), Luke and Kollias (2007), or Rambukkange et al. (2011).

We present a novel algorithm to analyze Doppler spectra, with improved resolution of the complexity of the spectra, discriminating up to two classes of particles in a cloud. The rationale of the algorithm is that an ensemble of cloud particles of the same species — the same thermodynamic phase, analogous shape and size — produces a Gaussian spectrum with characteristic parameters, which are related to the global moments of the Doppler spectrum. Ensembles containing different classes of cloud particles produce linearly superposed Gaussian Doppler spectra with parameters that are (not necessarily but probably) sufficiently different that they can be separated.

Knowing the three moments and the LDR for each class, we are able to evaluate microphysical parameters for both the classes of cloud particles, extending and making more exhaustive our knowledge on cloud microphysical processes.

This algorithm has been applied routinely on the measurements taken by a 36 GHz Doppler research vertically pointing cloud radar, MIRA-36, that operates in Hamburg, Germany. Among the measurements collected between September 2006 and July 2007, we had examined closely spectra from several days in which deep frontal clouds showed up (Melchionna et al., 2008). For these clouds the global spectral width showed large values. In these cases we often observe, after the decomposition, a hundred metres depth layer with bimodal spectra, which are typical of a mixed-phase layer (Zawadzki et al., 2001).

The decomposition algorithm here presented is furthermore easily modifiable, so that future studies could be conducted, i.e. by changing the shape of the curves composing the spectra and combining the results within measurement campaigns in which several instruments to investigate clouds are involved, including TOSCA¹, COPS² and, currently, the Barbados campaign³.

¹<http://gop.meteo.uni-koeln.de/tosca/doku.php>

²<http://www.uni-hohenheim.de/spp-iop/index.htm>

³<http://barbadossite.wordpress.com/>

We believe that the retrievals here shown, combined with measurements other instruments of investigation will bring us to a deeper understanding of the microphysical processes that are going on in a mixed-phase cloud.

Moreover, the microstructure of mixed-phase cloud as retrieved by cloud radar data has been compared with the results obtained by a configuration of the COSMO-DE model which includes an explicit cloud microphysical parametrization (Seifert and Beheng, 2006).

Thus the further advance of our understanding on cloud microphysics could be used to evaluate and develop more realistic cloud models, in order to advance our knowledge on elusive mixed-phase clouds.

Chapter 2

Description of cloud microphysics

Schneeflöckchen, Weißbröckchen,
wann kommst du geschneit,
du wohnst in den Wolken,
dein Weg ist so weit.
Volkslied

2.1 Introduction

Cloud microphysical processes are related to the formation and to the small-scale modifications of clouds. Many and various microphysical¹ phenomena, most of which are still not completely understood, are responsible for the growth and for the phase modification of cloud particles. A simplified schema of cloud processes is depicted in figure 2.1. We identify as the basic processes that make a cloud: nucleation, condensational growth (and evaporation) by diffusion, and interparticle collection.

Let us consider an air parcel. An air parcel is an idealized volume of air containing a large number of air molecules. In a parcel the air is considered to be either dry or moist, and to have uniform thermodynamical properties. The parcel moves adiabatically through the atmosphere, without exchange of matter with it. To reach the equilibrium with the surrounding ambient pressure, the parcel can expand, cooling, or shrink, warming.

Nucleation of cloud particles occurs by the general following steps: water vapor is produced on the Earth surface by evaporation; thereafter convection in the troposphere causes the upward motion of a parcel of moist air; the rising parcel expands and cools adiabatically; if air becomes supersaturated with respect to liquid and

¹The prefix *micro* refers to the small dimension of the cloud particles relative to the entire cloud. Cloud particles sizes range from micrometres to millimetres.

to solid water phases, and in presence of suitable aerosol particles, condensation or deposition of water vapor (made possible because of supersaturation) lead to the formation of respectively liquid or solid cloud particles.

After nucleation, cloud particles continue to grow by diffusion of water vapor molecules on their surface up to 100 μm in diameter. Growth by diffusion diminishes in proportion to the ratio between surface and volume, and becomes insignificant at 100 μm diameter.

Interparticle collection process becomes dominant for further growth of the particles. Collection may occur among particles with the same or with different thermodynamic phase. Coalescence and aggregation are the processes of collection among respectively only liquid water particles (drop–drop interaction) and only solid water particles (ice–ice interaction). Contact freezing and riming are the processes with which respectively a larger liquid water particle collects a smaller solid water particle (drop–ice interaction) or a larger solid water particle collects a smaller liquid water particle (ice–drop interaction).

The microphysical properties of cloud particles are specified by phase, size, shape, and number concentration.

Cloud particles can be either in liquid or in solid phase. Indeed, the most general classification of clouds that one can give distinguishes warm clouds, made of only liquid droplets, from cold clouds, made of ice and eventually droplets. A portion of the cloud in which both the phases are present is called mixed-phase zone.

As book references about cloud microphysics we suggest Wallace and Hobbs (1996), Pruppacher and Klett (1997), Young (1993).

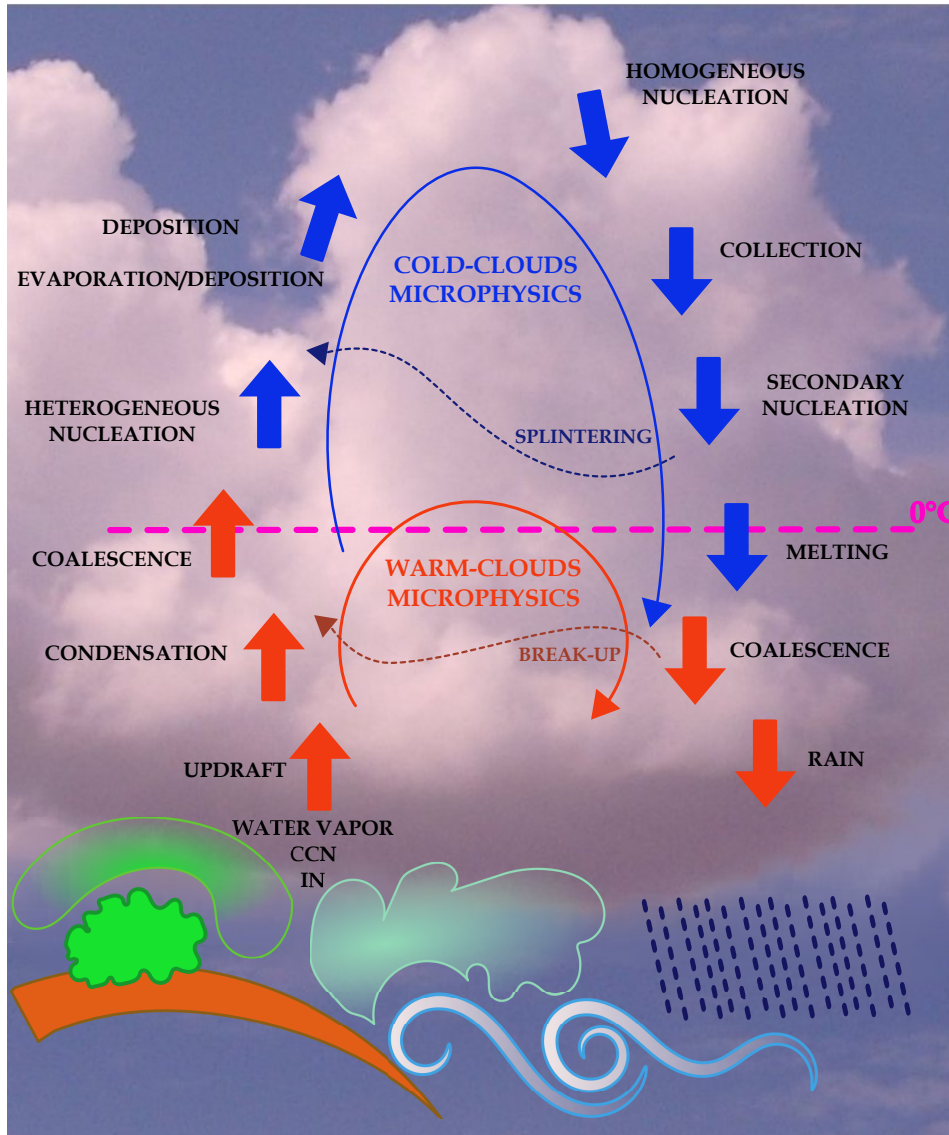


Figure 2.1: Summary of the microphysical processes operative in clouds. Red arrows indicate the processes related to liquid droplets; blue arrows indicate the processes related to ice particles, eventually mixed with liquid droplets.

2.2 Warm–clouds microphysics

2.2.1 Droplets formation

Liquid particles, i.e. cloud droplets, form by condensation of water vapor on atmospheric aerosols. In the atmosphere, aerosols acting as Cloud Condensation Nuclei (CCN) are sulfates, nitrates, or soluble material with dimensions of tenths of micrometres. The process of condensation of droplets is described by the Köhler theory (Köhler, 1936); it computes the supersaturation at which the cloud drop is in equilibrium with the environment over a range of droplet diameters. The Köhler equilibrium equation combines the change in saturation vapor pressure due to a curved surface with the saturation vapor pressure due to the solute, and therefore depends on the amount and composition of the solute (i.e. the atmospheric aerosol). When the conditions of ambient supersaturation given by the Köhler theory are reached, water vapor condenses first on a CCN, forming a liquid water film around it (activation of the CCN), and then continues to condensate on the surface of the new born droplet. This process reduces the amount of water vapor in the surrounding ambient, but, at the same time, adiabatic cooling caused by upward air motions reduces the equilibrium pressure. The activation of CCNs continues as long as the rate of reduction of partial pressure by expansion and by depletion of water vapor stays lower than the rate of reduction of equilibrium pressure by adiabatic cooling. Depending on CCNs characteristics and on updraft velocity, the number of droplets formed ranges from million to billion per cubic metre.

2.2.2 Droplets growth by condensation

Once that the CCNs have been activated, the droplets in warm clouds grow by condensation as long as the supersaturation exceeds the equilibrium value. By reasons of balance among molecular diffusion in the proximity of the particles and outflowing of latent heat released by the process of condensation, the growth rate decreases as the droplets grow.

2.2.3 Droplets growth by coalescence

In a warm cloud, a big droplet with a relatively higher fall velocity may collide against the little ones on its path, and eventually coalesce, forming a larger drop. The process of coalescence depends strongly on the size of collector and collected droplets. That is because a big droplet throughout its falling bends the air flow around itself, and hence pushes the little droplets away. Thus just a little fraction of droplets on the geometrical path of the collector does actually collide with it. Moreover, not all the collisions result in a coalescence, because air may still be trapped at the point of impingement. Laboratory studies have shown that the maximum collision efficiency is achieved by droplets with diameters from 60 to 100 μm sweeping droplets with diameters as small as 10 μm . Once that the droplets have reached the dimension of 0.1 mm, they grow by coalescence exponentially up to raindrop size.

It's disgusting.
I see more belly than brother.
S. K.

2.3 Cold-clouds microphysics

2.3.1 Ice crystals formation - primary nucleation

There are several nucleation processes that lead to the formation of ice crystals, schematically represented in figure 2.2.

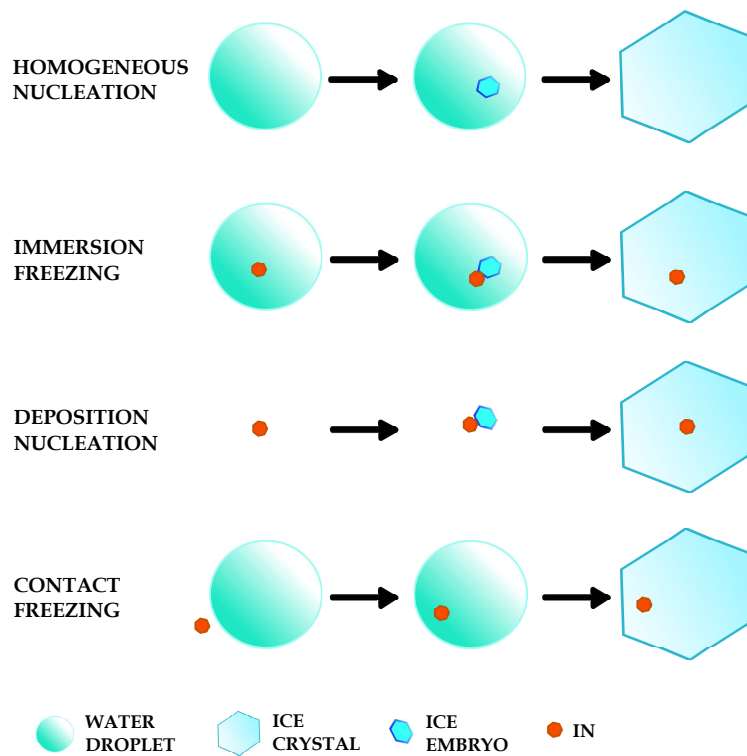


Figure 2.2: Schematic representation of the nucleation mechanisms of ice particles.

Let us start from liquid water. The presence of liquid water in the troposphere² is very common, because liquid water can exist below 0 °C down to -40 °C in the form of supercooled droplets. Below -40 °C water can not exist in liquid phase anymore, then supercooled droplets certainly freeze at those temperatures. For ice particles, as for liquid droplets, water molecules need to come together to form an ice embryo; if the embryo overcomes a critical size, the droplet freezes at a temperature that could be higher than -40 °C. If the droplet is made of pure water, we call the frozen process homogeneous nucleation. Homogeneous nucleation of liquid droplets

²The lowest temperature at the top of the troposphere is about -50 °C.

to ice occurs at temperatures around $-35\text{ }^{\circ}\text{C}$. Anyway, similarly to liquid droplets, the freezing process is favored by the presence of foreign particles, the Ice Nuclei (IN). When the creation of an ice cloud particle involves the presence of an IN, the nucleation is termed heterogeneous. Appropriate INs are insoluble particles with a crystalline structure affine to that of the ice crystals, i.e. hexagonal. If the supercooled droplet enclose an IN, water molecules will use it as molecular template for the ice crystal lattice, heightening the temperature of freezing (immersion freezing). Kaolinite (a clay) can nucleate at temperature so high as $-15\text{ }^{\circ}\text{C}$, whereas silver iodide can nucleate even at $-4\text{ }^{\circ}\text{C}$, reason why it is used in cloud seeding; biogenic matter, such as decayed plant leaves, nucleates also at $-4\text{ }^{\circ}\text{C}$.

Heterogeneous nucleation can besides occur by deposition or by contact.

Deposition nucleation is a process in which, granted that the air is supersaturated in respect to the solid phase of water, an ice particle forms by deposition of water vapor molecules on an IN.

Contact nucleation occurs when a cloud droplet freezes after it impacts with one external IN.

Nucleation by contact occurs at higher temperatures than the temperatures needed for the nucleation of the same IN but embedded in the droplet.

2.3.2 Ice crystals growth by deposition

Crystals of ice grow on the lattice of the INs into hexagonal prisms. Prisms are composed by two hexagonal basal facets with width a , and by six rectangular prism facets with length c , as shown in figure 2.3, and are characterized by their axial ratio c/a .



Figure 2.3: Basic shapes of ice crystals. The axial ratio c/a defines the shape of the crystal: less than 1 for plates-like, greater than 1 for columnar.

The basic shapes of ice crystals, as depicted in figure 2.3, are plate-like (axial ratio less than the unity) or columnar (axial ratio bigger than the unity). Their aspect ratio depends on how water molecules put themselves together on the growing lattice. Laboratory experiments have shown that the shape of an ice crystal depends strongly and in a complicated way on the temperature and on the amount of water vapor of the ambient air in which the crystal is growing, as it is illustrated in the morphology diagram (figure 2.4). Even if the physics behind this behavior is still not understood, we know that there is an alternation of the basic habits with the temperature, and that the shapes become complicated with higher supersaturation.

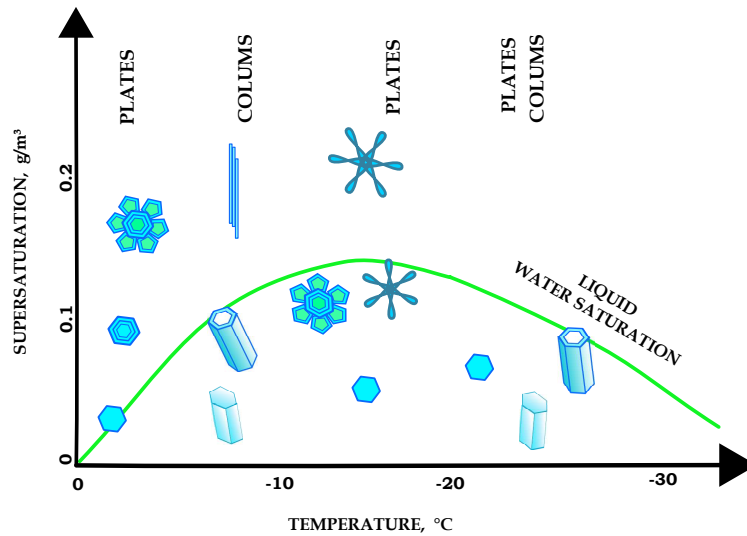


Figure 2.4: The snow crystals morphology diagram. It shows how snow crystals grow with temperature and water vapor supersaturation relative to ice. As the temperature decreases, there is an alternation between basic shapes, and the complexity of the shape increase with the supersaturation. The water saturation curve is depicted in green.

2.3.3 Ice crystals growth by collection

The collection processes that involve ice particles are aggregation and riming. Note that contact freezing, mentioned above about the formation of ice particles, has to be regarded also as a collection process.

Aggregation occurs when two ice particles collide and stick together. This process occurs more likely at temperatures above about $-5\text{ }^{\circ}\text{C}$ by sintering³. Dendrites are very likely to adhere because their arms can easily interlace during a collision, whereas plates tend to rebound.

Riming occurs when ice crystals pass through a region filled with supercooled droplets. The contact between ice and droplets results in the freezing of the droplets onto the ice surface. The collision efficiency for the riming process becomes appreciable for ice crystals with basal facet of about $150\text{ }\mu\text{m}$ for plates and $25\text{ }\mu\text{m}$ for columns (remember that a supercooled droplet has a diameter of about $10\text{ }\mu\text{m}$). At the early stage of the riming process, the original morphology of the rimed crystal is still recognizable. As the riming process continues, the number of droplets accumulated obscures the identity of the crystal, and the resulting crystal is referred to as graupel. When the dimension of graupel crystal exceeds 5 mm we referred to it as hail.

³Formation of a coherent mass of particles by heating without melting them until they adhere to each other.

2.4 Mixed-phase cloud microphysics

2.4.1 Ice crystals formation - secondary nucleation

The last decades of measurement campaigns have shown that ice crystals concentration disagrees with the one predicted by theory, when only ice crystals produced by nucleation are considered. In the attempt to explain this disagreement a few mechanisms of secondary ice production were postulated. Mechanical fracture of the arms of dendrites may increase the ice concentration. However, this process appears insufficient to explain the enhancement of concentration observed.

Laboratory works of Hallett and Mossop carried out between the seventies and eighties (Hallett and Mossop, 1974; Mossop and Hallett, 1974; Mossop, 1976, 1978, 1985) have pointed out that pristine ice crystals can be produced by splintering from rimed ice crystals. They have found out that there are strict conditions under which ice crystals growing by collection of supercooled cloud water may release tiny splinters of ice, that subsequently grow into columnar ice crystals. The variables involved in the process are: temperature of the cloud of supercooled droplets, that has to be between $-8\text{ }^{\circ}\text{C}$ and $-3\text{ }^{\circ}\text{C}$ with a maximum at about $-5\text{ }^{\circ}\text{C}$; velocity range at which the graupel falls through this cloud, going from 0.7 m/s to 2.7 m/s ; and size distribution of the supercooled water droplets, since splintering appears in presence of droplets larger than $25\text{ }\mu\text{m}$, and at the same time it is enhanced by the presence of droplets smaller than $12\text{ }\mu\text{m}$. The medium rate of secondary ice production is of one splinter for every 250 droplets larger than $25\text{ }\mu\text{m}$ collected by an ice particle with fall velocity of about 2 m/s at a temperature of $-5\text{ }^{\circ}\text{C}$. Even though ample laboratory evidences have characterized the splintering process, its physical mechanism is still uncertain (Cantrell and Heymsfield, 2005).

2.4.2 Ice crystals growth - ice crystal theory

There exists a special growing process for ice crystals immerse in a cloud of supercooled droplets, that takes the name of ice crystal theory⁴. This process involves the growing of ice crystals at the expenses of supercooled droplets. One should however keep in mind that the evolution of a mixed-phase cloud depends on the local thermodynamical characteristics of the cloud. In fact the rates of growth by condensation/deposition and of loss of mass by evaporation/sublimation are driven by the difference between the in-cloud water pressure e and the equilibrium vapor pressure over liquid/ice. Therefore the supersaturation conditions of the air can be such that both the liquid and ice particles continue to grow or both continue to evaporate or such that ice particles grow and liquid particles evaporate, the latter process being the ice crystal theory, as just stated.

Let us then consider the equilibrium vapor pressure over liquid $e_{s,w}$ for subfreezing temperatures and the equilibrium vapor pressure over ice $e_{s,i}$. The difference ($e_{s,w} - e_{s,i}$) may be evaluated by using Magnus equations. The Magnus equations (Herbert, 1987) are special solutions of the Clausius-Clapeyron differential equations for the saturation vapor pressures. Magnus equations are widely used in meteorology because they are simple to apply and at the same time they are still sufficient accurate for cloud microphysical uses. Their expressions are given by:

$$e_{s,w} = e_{s,w}(T_{(0)}) \exp \left[\frac{A_w(T - T_{(0)})}{T - B_w} \right] \quad (2.1)$$

$$e_{s,i} = e_{s,i}(T_{(0)}) \exp \left[\frac{A_i(T - T_{(0)})}{T - B_i} \right] \quad (2.2)$$

with the index w and i referring respectively to liquid water and ice, the equilibrium vapor pressures $e_{s,w/i}$ given in hecto Pascal, the absolute temperature T in kelvin, and with the values: $e_{s,w}(T_0) = 6.1070$ hPa, $A_w = 17.15$, $B_w = 38.25$ K, $e_{s,i}(T_0) = 6.1064$ hPa, $A_i = 21.88$, $B_i = 7.65$ K, where $T_{(0)}$ is the freezing point of water.

The difference ($e_{s,w} - e_{s,i}$) is always positive for all subfreezing temperatures, with a maximum at about -12 °C. Thus, when air is saturated with respect to liquid water, it is also always saturated with respect to ice.

Korolev and Mazin (2003) and Korolev (2007) have connected the ascension velocity of air parcels, and therefore, with the velocity at which water vapor is provided, with three different possible behaviors of the cloud particles: growing of both liquid and ice particles, growing of ice particles and evaporation of liquid particles, sublimation of ice particles and evaporation of liquid particles.

The possible scenarios, schematically illustrated in figure 2.5, are:

1. $e > e_{s,w} > e_{s,i}$ - growing of liquid and ice particles:
if enough water vapor is provided by the updraft motions of the air, both

⁴In literature this process is referred to with several different names, i.e. ice crystal theory, ice crystal process of precipitation, WBF theory or process, by the names of the scientists who have been the first to describe it: Wegener (1911), Bergeron (1935), and Findeisen (1938).

droplets and ice crystals, despite they compete for the same water vapor, continue to grow by diffusion. Anyway, ice particles grow for deposition faster than droplets for condensation, as a consequence of the different growth rates. This condition maintains the unstable state of mixed-phase until water vapor is provided by the updraft.

2. $e_{s,w} > e > e_{s,i}$ - growing of ice particles and evaporation of liquid particles (ice crystal theory):

this is the case in which ice crystal theory occurs. Ice crystal theory is considered to be the major process that contributes to the growth of the ice crystals in clouds with low updraft and consequently, low supersaturation, such as stratus clouds.

The depletion of water vapor in the vicinity of an ice crystal lowers the vapor pressure below the liquid water saturation value, causing the adjacent droplets to evaporate. This process is pictorially illustrate in figure 2.6 .

If this condition persists, it brings to the glaciation of the portion of the cloud

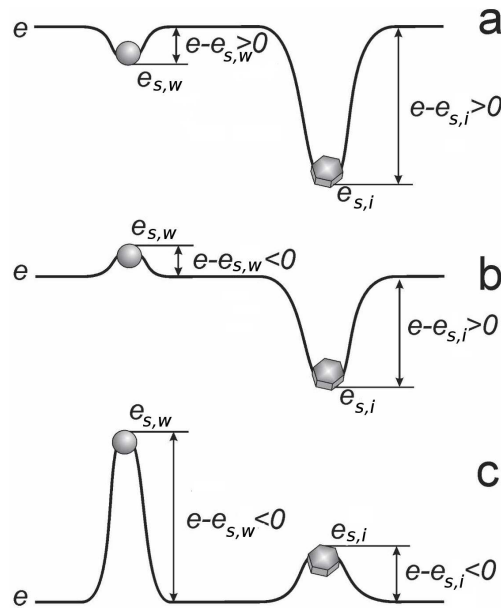


Figure 2.5: Schematic diagram of possible proportions among in-cloud water pressure e and equilibrium vapor pressure over liquid and ice $e_{s,w}/i$. Depending on the value of e in respect to the values of $e_{s,w}$ and $e_{s,i}$ in a localized portion of the mixed-phase cloud, three different scenarios are possible: (a) both liquid droplets and ice particle grow; (b) liquid droplets evaporate and ice particles grow; and (c) liquid droplets evaporate and ice particles sublimate. From Korolev (2007), with the permission of the author.

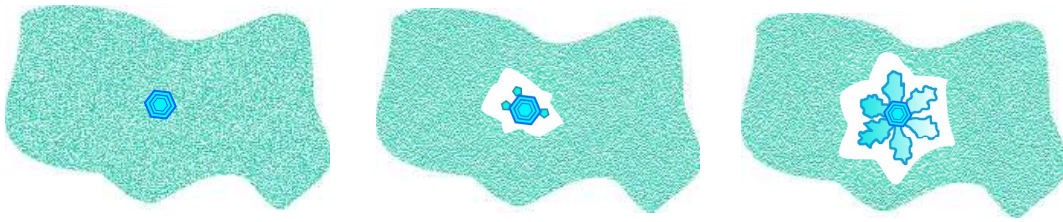


Figure 2.6: An ice crystal surrounded by droplets grows by deposition of water vapor which is provided by the evaporation of the droplets in its proximity.

interested.

The vapor flux which comes to establish from droplets to ice crystals achieves a maximum value for temperatures lower than $-12\text{ }^{\circ}\text{C}$; at higher temperature the latent heat released by the sublimation process reduces too much the vapor pressure around the ice crystals surface.

One macroscopic effect of the ice crystal theory is the formation of holes in warm clouds. In a warm cloud intercepted by a bounce of ice particles, for example the ones produced in the wakes of airplanes, it would be need less then half an hour to a large area of liquid water droplets to evaporate feeding the ice particles, as theorized by Rangno and Hobbs (1983) and in the recent study by Heymsfield et al. (2010). The glaciated part of the cloud would then descend to a lower level, leaving a clear sky area above. An example is shown in picture 2.7.

3. $e_{s,w} > e_{s,i} > e$ - simultaneous sublimation of ice particles and evaporation of liquid particles:

when the water vapor content is depleted by the mixing with dry air, as likely occurs along cloud boundaries, both droplet evaporate and ice particles sublimate up to the dissolve of the entire cloud; if ice particles sublimates all before the droplets (or the opposite), the cloud will pass through a stage of liquid (glaciated) stage.

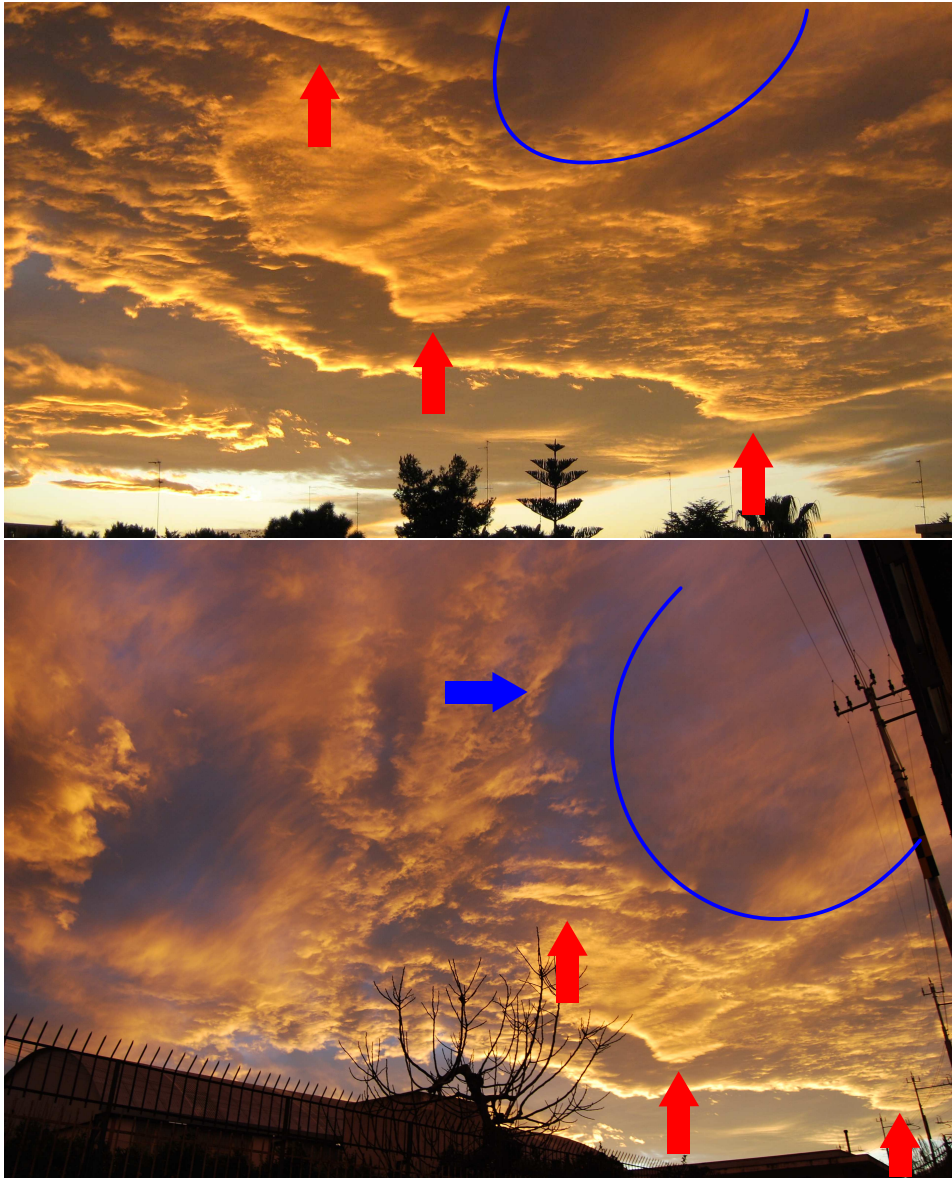


Figure 2.7: One effect of the ice crystal theory is the creation of holes in clouds. Here the hole appears as a clear area in the liquid cloud, partially covered by a glaciated descending portion of the cloud. The pictures were taken in the vicinity of an airport the 25th December 2009, in Bari, south of Italy, west looking. They are 6 minutes elapsed (17:34 upper panel; 17:40 lower panel); the picture in the lower panel was taken 500 m norther than picture in the upper panel. Red arrows indicate some reference points in the liquid portion of the cloud structure, the blue line indicates the boundaries of the glaciated cloud portion, and the blue arrow indicates the hole formed after its descending in picture (b). [Upper panel: photograph by S. Melchionna; lower panel: photograph courtesy of G. Genchi]

2.5 Precipitation

Precipitation, whether as rain or snow, appears once the particles in a cloud have reached a size large enough to fall against the local updrafts.

The coalescence process continues also in rainfall regimes. In steady air flow the equilibrium shape of a water drop at terminal velocity is determined by the balance of internal and external pressure at its surface; these forces involve aerodynamics, hydrostatic, and surface tension. As a result of the application of these forces, the shape of the drop deviate from a sphere, becoming oblate, with a dip into the bottom side. The dip increases in depth and width as the mass of the drop increases. Thus the drop looks more like a donut, with the upper side of the hole connected by a tiny film of water. During the fall, the film swells as a parachute. At some point it bursts, producing a spray of droplets, and the ring of water at its lower rim breaks up into small drops. The maximum size that raindrops can reach is about 7 mm.

2.6 Particle size spectra

To describe the microstructure of a cloud (without regard to the mechanisms that produced it) we need ultimately to specify how many particles of which size and shape are present at a given location and time. We express mathematically these characteristics by means of size spectra, which represent the cloud particle concentration in function of the diameter of the particles. The size spectra measured are approximated by empirical functions, which include several parameters, in order to take into account for the several shapes and sizes. These functions are widely used in the remote sensing of clouds as well as in modeling and parameterization of cloud properties.

As an example, cloud droplets are reasonably approximated by a generalized gamma distribution:

$$f(D) = c_N D^p e^{-\beta D^\lambda} \quad , \quad (2.3)$$

where c_N is a normalization constant, p , with p a positive number, describes the shape of the spectrum for small radii, and β and λ determine the exponential tail for large radii. Measurement campaigns settled the values of p for liquid clouds between 6 and 15.

The particular case of equation 2.3 with $\beta = 0$ and with negative values of p :

$$f(D) = c_N D^p \quad (2.4)$$

with p ranging from -12 to -2 , was founded to be a good approximation for ice crystal size spectra in cirrus and cloud particles with diameters between 600 and 1600 μm .

How odd.

The only way for us to touch the clouds is having a walk in the fog.

2.7 Size, shape and fall velocity of cloud particles

Knowing the size of the particles, together with their shape and phase, is fundamental to determine their terminal fall velocity.

Cloud droplets are spherical as result of surface tension effects and have diameters of tens of micrometres; their terminal fall velocity in still air is proportional to the square of the diameter D and does not exceed some centimetres per second.

Drizzle drops, that have to be regarded as the transition step between droplets and raindrops, have diameters of tenths of millimetres and fall velocity of some tens of centimetres per second.

Following Stokes theory, and assuming a small Reynolds number⁵ Re , the terminal velocity of a liquid water sphere falling through still air is given by:

$$v(D) = \frac{\rho_w - \rho_a}{36 \eta} g D^2 \quad , \quad (2.5)$$

with ρ_w liquid water density, ρ_a dry air density, η air dynamic viscosity, g gravitational constant. Using the standard values (sea level, 15 °C) of these constants we obtain:

$$v(D) = 31.3 D^2 \quad , \quad D \leq 0.1 \text{ mm} \quad , \quad (2.6)$$

and the inverse function:

$$D(v) = 0.179 \sqrt{v} \quad , \quad v \leq 0.313 \text{ m/s} \quad , \quad (2.7)$$

with D in millimetre and v in metre per second. The limit value for the diameter is due to the fact that as the drop grows the equilibrium among the forces affecting the drop shape changes, causing the Reynolds number to significantly increase.

Raindrops have in fact a flat shape, that can be approximated by an oblate spheroid with maximum diameter oriented perpendicularly to the flow and smaller diameter oriented vertically; this shape becomes parachute-like as the drops increase their size above some millimetres, because of the corresponding increasing of aerodynamic forces on their lower side; their fall velocity may reach up to ten metres per second. Figure 2.8 depicts the various velocities of liquid drops based on their sizes.

One general empirical equation for the terminal fall velocity of such drops is given by Atlas et al. (1973), which have fitted the data collected by Gunn and Kinzer (1949):

$$v(D) = 9.65 - 10.3 e^{-0.6 D} \quad , \quad 0.6 \text{ mm} \leq D \leq 5.8 \text{ mm} \quad , \quad (2.8)$$

⁵The Reynolds number is given by the ratio between inertial and viscous force acting of a particle moving within a fluid. Its value depends on the regime for the flow: small for laminar flows and large for turbulent flows.

with the inverse:

$$D(v) = 1.67 \left[2.33 - \ln(9.65 - v) \right] , \quad 2.46 \text{ m/s} \leq v \leq 9.33 \text{ m/s} . \quad (2.9)$$

Peters (2009a) has derived an equation that is valid for any diameter assumable by cloud droplets and raindrops joining equations 2.6 and 2.8 for their upper and lower limit, respectively. With D_c being a characteristic diameter with value 0.108 mm, the velocity of the particles in function of their diameter is given by:

$$v(D) = 9.65 - 10.3 e^{-0.6\sqrt{D^2 - D_c^2}} , \quad (2.10)$$

and then the inverse:

$$D(v) = \sqrt{\left(\frac{1}{0.6} \ln \frac{10.3}{9.65 - v} \right)^2 + D_c^2} , \quad (2.11)$$

with now D and v varying through the whole domain of diameters and fall velocities. Equations 2.6, 2.8, and 2.10 are represented in figure 2.8.

In contrast with liquid cloud particles, pristine ice particles never exceed some millimetres in size, and they occur in a broad diversity of shapes. Nucleation of ice particles produces simple monocrystalline structures, i.e. columns or plates, that grow into hexagonal forms whose geometry depends strongly on the temperature and

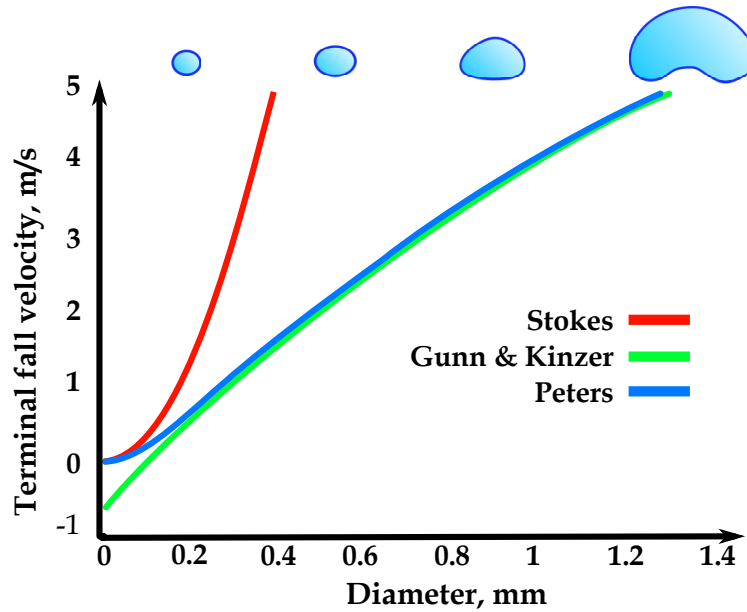


Figure 2.8: Falling velocity of liquid drops based on their size. The shapes of liquid drops with the size are also indicated. From Peters (2009a), with the permission of the author.

humidity conditions (Magono and Lee, 1966). These individual crystals may stick together forming larger aggregates (snowflakes), as well as droplets may freeze on them, forming rimed crystals. The fall velocity of a columnar crystal one millimetre in length is about half a metre per second, and increases with the length of the crystal. The terminal fall velocity of a plate-like crystal is also of the same order, but it is almost independent of its dimensions, because the drag force acting at a given speed on the base of the crystal balances the gravitational force which is proportional to the area. The situation changes if the crystals, of any sort, are rimed; then the terminal fall velocity depends strongly on the dimensions and on the degree of riming of the crystals, and it reaches even some metres per second for crystals as large as some millimetres.

Several measurement campaigns have shown that the terminal fall velocity for ice crystals is a power function of the maximum dimension D_M of the particle in the form:

$$v_t(D_M) = \mathcal{A} D_M^{\mathcal{B}} \quad , \quad (2.12)$$

where \mathcal{A} and \mathcal{B} are empirical coefficients varying with the family of crystals. Equation 2.12 for different kind of crystals is depicted in figure 2.9.

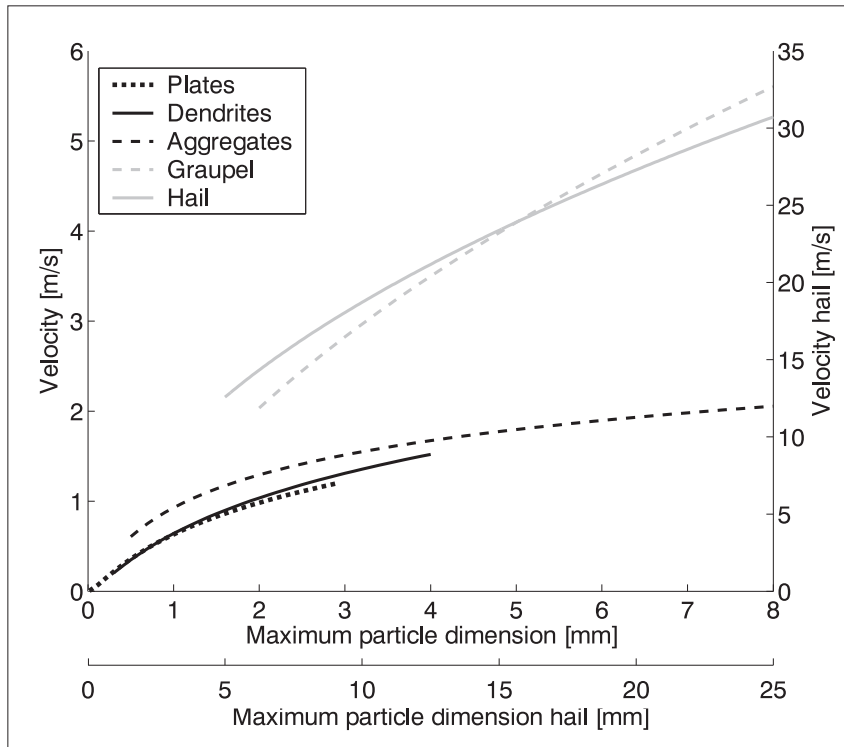


Figure 2.9: Falling velocity of frozen hydrometeors based on their size. By Spek et al. (2008); with the permission of the authors.

The coefficients \mathcal{A} and \mathcal{B} can be evaluated by following Mitchell (1996). The terminal fall velocity depends, beyond the maximum dimension D_M , on mass and area projected on the flow direction, which both can be also parameterized as power laws of D_M :

$$m(D_M) = \alpha D_M^\beta \quad (2.13)$$

$$A(D_M) = \gamma D_M^\sigma, \quad (2.14)$$

with m mass in grams, A area in square centimetre, D_M maximum extension in centimetre, and with α , β , γ , and σ empirical coefficients, determined from best fits to the experimental data in various size regions, tabled in table 2.1 for a selection of families of ice crystals.

It is obvious that if ice crystals would be homogeneous spheres, β and σ would assume the values of 3 and 2 respectively, values that are anyway the upper limit for the exponents in 2.13 and 2.14. According to Mitchell (1996) formulation the coefficients in equation 2.12 are expressed as:

$$\mathcal{A} = a_{Re} \nu \left(\frac{2 \alpha g}{\gamma \rho_a \nu^2} \right)^{b_{Re}} \quad (2.15)$$

and

$$\mathcal{B} = b_{Re}(\beta + 2 - \sigma) - 1, \quad (2.16)$$

where the coefficients a_{Re} and b_{Re} for large Reynolds numbers and particles with $D_M > 500 \mu\text{m}$ were calculated by Khvorostyanov and Curry (2002):

$$\begin{aligned} a_{Re} &= 1.85 \\ b_{Re} &= \frac{1}{2}. \end{aligned}$$

The general behavior of both the coefficients is to decrease with increasing size. Moreover, the terminal velocity increasing becomes slower with the increasing of the

Table 2.1: Characteristic coefficients for the terminal fall velocity of snow (equation 2.15 and equation 2.16)

| Type of crystal | Size (cm) | α | β | γ | σ | \mathcal{A} | \mathcal{B} |
|------------------|--------------------|----------|---------|----------|----------|---------------|---------------|
| Hexagonal plates | $0.0015 \leq 0.01$ | 0.00739 | 2.45 | 0.24 | 1.85 | 1.296 | 0.3 |
| | $0.01 \leq 0.3$ | | | 0.65 | 2 | 0.788 | 0.225 |
| Dendrites | $0.03 \leq 0.4$ | 0.003 | 2.3 | 0.21 | 1.76 | 0.883 | 0.27 |
| Aggregates | $0.05 \leq 0.8$ | 0.003 | 2.1 | 0.2285 | 1.88 | 0.847 | 0.11 |
| Graupel | $0.2 \leq 0.8$ | 0.049 | 3.06 | 0.5 | 2 | 2.313 | 0.53 |
| Hail | $0.5 \leq 2.5$ | 0.466 | 3 | 0.625 | 2 | 6.380 | 0.5 |

particle size, because for ice crystal larger the size smaller the bulk density. One should note that equations from 2.12 to 2.16 are valid near the ground level. To make the expression of the falling velocity valid for other altitudes, all other conditions being equal, it is necessary to multiply it for the correction factor c_{pT} , depending on pressure and temperature:

$$v_D(p, T) = c_{pT} v_D(p_0, T_0) = \left(\frac{p_0}{p} \frac{T}{T_0} \right)^{b_{Re}} v_D(\rho_a) = \left(\frac{\rho_a}{\rho_{a0}} \right)^{b_{Re}} v_D(\rho_{a0}), \quad (2.17)$$

with p_0 , T_0 , and ρ_{a0} are pressure, temperature, and density at standard conditions (sea level), p , T , and ρ_a are pressure, temperature, and density at the desired altitude. Since ρ_a in equation 2.15 depends on pressure and temperature, it need to be appropriately substituted.

2.8 Liquid and Ice Water Content

In order to describe the microphysical state of a cloud we commonly refer in case of liquid clouds to its Drop Size Distribution (DSD) and to its Liquid Water Content (LWC), or in case of ice clouds to its Particle Size distribution (PSD) and to its Ice Water Content (IWC).

As seen in section 2.6, the Size Distribution represents the cloud particle concentration in function of the diameter of the particles. We calculate the LWC and the IWC by integration of the DSD or of the PSD, respectively, which are in this case expressed by the number density of the particles n as a function of the particle radius r , or as a function of r_s , radius of the ice sphere having the same mass of the corresponding irregular ice particle:

$$\text{LWC} = \frac{4\pi}{3} \rho_w \int r^3 n(r) dr \quad (2.18)$$

$$\text{IWC} = \frac{4\pi}{3} \rho_i \int r_s^3 n(r_s) dr_s \quad , \quad (2.19)$$

with ρ_w the liquid water density, and ρ_i the ice water density.

Chapter 3

Cloud radars

3.1 Introduction

In meteorology radar systems are active devices designed to remotely study the atmospheric environment from a ground platform¹.

A radar produces electromagnetic radiation with a well defined frequency in the microwave band, and emits it through an antenna. Microwaves travel through the atmosphere and interact with targets such as raindrops or cloud forming particles – our interest as meteorologists – or such as insects, birds, etc. Because of this interaction, the targets emit radiation themselves. The part of radiation directed back to the radar is received by the radar system. Studying these echoes we are able to extract information on the observed objects. The design of the radar allows us to detect and locate targets, reason for which in meteorology radars are used operationally for monitoring the weather; radars also provide measurements that, after proper signal processing, allow us to individuate properties of the targets, such as size, shape, and velocity, and therefore to derive an empirical description of the physical processes that were likely operative at the time of measurements.

The advantages of cloud radar systems, compared with other remote sensing instruments, are the potential of detecting clouds over the whole troposphere, and the capability of long unattended operation.

Many text books describe the principle of radar systems; in this work we refer to Skolnik (1990), Doviak and Zrnić (1993), Bringi and Chandrasekar (2001).

¹Nowadays we can find meteorological radars also on air- or space- borne platforms

3.2 The radar equation

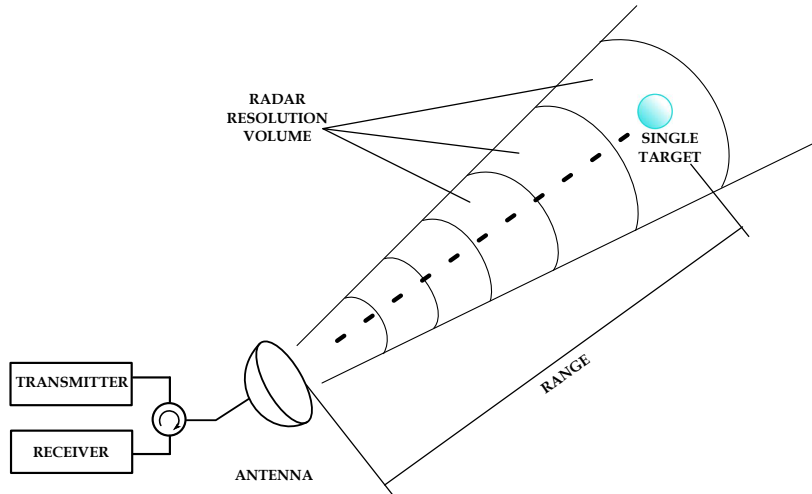


Figure 3.1: Basic representation of a radar system.

Figure 3.1 shows a schematic representation of a weather radar. A radar system incorporates the source of microwaves, that is a resonator, such as a klystron or a magnetron. The wavelength range useful for meteorological applications goes from millimetres to metres, in response of practical requirements (attenuation, range ambiguities, velocity ambiguities, ground clutter, spatial resolution).

In the last decades improvement of equipment sensitivity with high power and short wavelength radars were accomplished. The operating frequency of the radar system used in this work - MIRA-36 - is 35.5 GHz, that corresponds to a wavelength of 8.45 mm. At this wavelength the sensitivity (inversely proportional to λ^4 , in Rayleigh scattering regime) for the small hydrometeor constituting clouds is finer than at longer wavelength. Moreover, the contribution to the scattering due to the turbulent fluctuations of the refractive index of clear-air is negligible. Radar systems operating at this short wavelength are then suitable for cloud studies, even though, in circumstances that need to be considered, rainfalls attenuate the signal.

The microwaves travel through proper guides to the antenna. For meteorological applications, the antenna is designed to emit radiation within a narrow beam, and to receive radiation traveling along the opposite direction.

The radiation is emitted in pulses of constant length τ . The depth of the radar resolution volume is directly proportional to the length of the pulse. The pulses are repeated at regular intervals of length T ($T = 1/\text{PRF}$, with PRF the pulse repetition frequency). During this time interval between two consecutive pulses the radar system waits for an echo. This procedure allow us to range-resolve radar data: by measuring the time delay t_D between any transmitted pulse and its echo, we

evaluate the distance r of a target as:

$$r = \frac{c t_D}{2} \quad , \quad (3.1)$$

with c speed of light.

The radar antenna transmits an electromagnetic pulse with power P_t in the space around it. If the antenna irradiated isotropically², the power per unit area on the surface of a sphere of radius r and with center at the antenna would be:

$$P_i = \frac{P_t}{4\pi r^2} \quad . \quad (3.2)$$

Thus the incident power density on a point target distant r from the antenna would be P_i . Anyway antennas are never isotropic, but they are designed to be highly directional: the geometry of their reflectors is such that most of the energy is transmitted within a beam along a specific direction. The directionality of the antenna is expressed by the gain $G(\Theta, \Phi)$, function of the spacial coordinates azimuth and elevation. The spacial gain $G(\Theta, \Phi)$ shows a maximum G_0 within the beam. For circular paraboloidal reflectors, such as the one of MIRA-36, G_0 is expressed by:

$$G_0 = \frac{4\pi A_e}{\lambda^2} \quad , \quad (3.3)$$

with λ wavelength of the emitted electromagnetic radiation and A_e effective aperture of the antenna.

Figure 3.2 shows $G(\Theta, \Phi)/G_0$ for the radar system MIRA-36, where H- and V-plane refer to the plane of oscillations of the electromagnetic waves (see section 3.7). By assuming a sharp-edged conical beam with uniform gain G_0 , an extended target

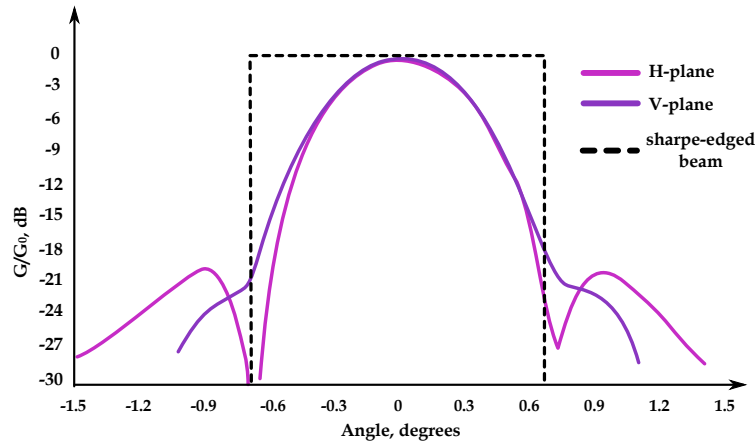


Figure 3.2: Beam pattern for radar MIRA-36, METEK documentation (2006)

with cross-sectional area A_{tg} that lies in the beam intercepts the amount of power:

$$P_{tg} = P_i G_0 A_{tg} \quad . \quad (3.4)$$

²power uniformly distributed on a sphere

If the target would not absorb any power but would re-irradiate all the intercepted power isotropically, the power density at distance r from the target would be (similarly to equation 3.2) :

$$P_r = \frac{P_{tg}}{4\pi r^2} \quad . \quad (3.5)$$

In a monostatic system, the same radar acts both as transmitter and receiver. Hence the radar antenna intercepts a power back from the target:

$$P_r = \frac{P_{tg}}{4\pi r^2} A_e \quad . \quad (3.6)$$

In antenna theory it is shown that the gain increases with decreasing wavelength:

$$A_e = \frac{G_0 \lambda^2}{4\pi} \quad . \quad (3.7)$$

Grouping the previous equations we obtain the radar equation for a single extended target:

$$P_r = \frac{P_t}{4\pi r^2} \frac{G_0 A_{tg}}{4\pi r^2} A_e = \frac{P_t G_0^2 \lambda^2}{(4\pi)^3} \frac{A_{tg}}{r^4} \quad . \quad (3.8)$$

Note that, because of the two-way trip of the signal, the power received by the antenna from a single target varies inversely to the fourth power of the distance.

Real targets do neither re-irradiate isotropically nor they are free of absorption. In order to maintain the validity of equation 3.8, we need to replace A_{tg} with the back scatter cross section σ , which specifies how much of the intercepted power is scattered back to the antenna. The backscattering cross-section σ has the dimensions of an area and depends on shape, size, and orientation of the target, but it is generally different from the physical cross section, because it depends also on conductivity and complex dielectric constant of the target, as well as on wavelength and polarization of the incident radiation.

By substituting the cross-sectional area A_{tg} of the target with its backscattering cross-section σ , equation 3.8 for a real target becomes:

$$P_\sigma = \frac{P_t G_0^2 \lambda^2}{(4\pi)^3} \frac{\sigma}{r^4} \quad . \quad (3.9)$$

This equation is valid for a single target in the volume V scanned by the radar. If the volume V contains more than one target (see figure 3.3), the total backscattered signal is the sum of the signals backscattered from each target i in V :

$$P_\sigma = \frac{P_t G_0^2 \lambda^2}{(4\pi)^3} \frac{1}{r^4} \sum_V \sigma_i \quad , \quad (3.10)$$

where the summation is over the volume centered at distance r , and σ_i is the backscattering cross-section of the i -th target in this volume.

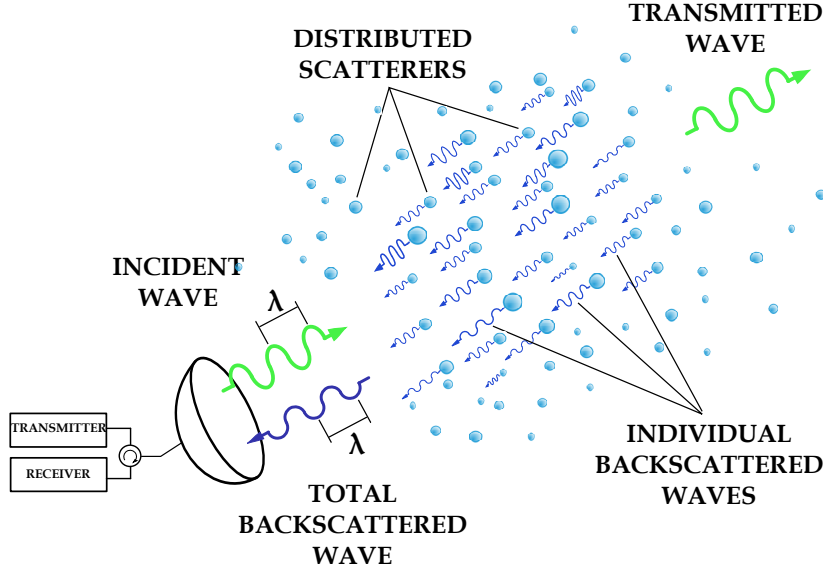


Figure 3.3: Schematic representation of the interaction among radar waves and a distributed target - namely cloud droplets.

The length τ of the emitted electromagnetic pulse and the beam width at distance r from the antenna determine the volume sampled by the radar:

$$V = \pi \frac{c\tau}{2} \left(\frac{r\theta}{2} \right) \left(\frac{r\phi}{2} \right) \quad , \quad (3.11)$$

with $c\tau/2$ being the volume depth, θ and ϕ the azimuth and elevation beam-widths, and the factor $\frac{1}{2}$ taking in account the two-way path.

Antennas with circular paraboloidal reflectors produce a symmetric beam, meaning $\theta = \phi$. Additionally, the Probert-Jones correction needs to be introduced to take in account that the beam shape is not uniform: assuming a Gaussian shape for the antenna beam (see figure 3.2), the radar sampling volume is smaller by a factor of $2 \ln 2$:

$$V = \frac{\pi\theta^2 r^2 c\tau}{2^4 \ln 2} \quad . \quad (3.12)$$

Let us assume that the targets are uniformly distributed over the volume, so that we may introduce the radar reflectivity η , such that it represents the backscattering cross-sectional area per unit volume:

$$\eta = \frac{\sum_V \sigma_i}{V} \quad . \quad (3.13)$$

Then equation 3.10 becomes:

$$P_\sigma = \frac{P_t G_0^2 \lambda^2 \theta^2 c\tau}{1024 (\ln 2) \pi^2 r^2} \eta \quad . \quad (3.14)$$

This signal needs still to be reduced because of the occurrence of losses. We group all the power losses introduced by the components between the antenna and the received input, such as waveguides or joints, in the factor L . The power loss L is measured at a fixed point in the radar system. MIRA-36 has a loss of power $\mathcal{L} = 10 \cdot \log L$ estimated to be about 7 dB. Considering the losses the equation 3.14 becomes:

$$P_\sigma = \frac{P_t G_0^2 \lambda^2 \theta^2 c \tau}{1024 (\ln 2) \pi^2 L r^2} \eta \quad , \quad (3.15)$$

or, simply:

$$P_\sigma = \frac{\text{constant}}{r^2} \eta \quad , \quad (3.16)$$

that represents the radar equation for uniformly distributed targets. It illustrates that the received power:

is a function of constants which depend on the characteristics of radar set;

is directly proportional to the radar reflectivity η , which represents the scattering properties of the ensemble of targets;

is inversely proportional to the square of the distance.

Backscattered power received at the antenna, decomposed in step:

$$P_\sigma = \left\{ \underbrace{\left[\underbrace{\left(\frac{P_t G_0}{4\pi r^2} \right)}_{\text{power density on a target}} \sigma \right]}_{\text{backscattered power}} \frac{1}{4\pi r^2} \right\} \frac{G_0 \lambda^2}{4\pi}$$

backscattered power collected by the antenna

Note that the amount of received power decreases with the second power of the distance, instead that with the fourth power as in the radar equation for a single target (equation 3.8), because the greater the distance, the larger the volume, the more numerous the scatterers.

As last aspect let us consider that all the radar systems, as electrical devices, suffer from thermal noise³. This noise produces an additive signal at the receiver input.

³Thermal noise is due to the thermal agitation of electrons that happens in any electrical conductor.

The receiver thermal noise power is given by:

$$P_N = k_B T_0 B F \quad , \quad (3.17)$$

where k_B is the Boltzmann's constant, T_0 is the standard temperature, B is the receiver bandwidth, and F is the receiver noise factor (or noise figure \mathcal{F}_N , if expressed in dB as $\mathcal{F}_N = 10 \cdot \log F$).

Since in all the equations seen up to this point the power P_σ is due to only scattering properties, and therefore is noise free, the power actually measured P_m by the radar system is given by the power backscattered from atmospheric targets plus the noise power:

$$P_m = P_\sigma + P_N \quad . \quad (3.18)$$

We define the Signal to Noise Ratio SNR as:

$$\text{SNR} = \frac{P_\sigma}{P_N} = \frac{P_m - P_N}{P_N} \quad . \quad (3.19)$$

Thus, we can evaluate the backscattered power P_σ from the SNR, which is a direct function of the noise and the measured power.

The nominal value of the thermal noise power for MIRA-36 assessed by equation 3.17 is about⁴ -100 dBm.

| | |
|---------------------------------------------------|---------------------------------------------------------|
| Receiver thermal noise power for MIRA-36: | |
| $\mathcal{P}_N = 10 \cdot \log P_N$ | |
| $= 10 \cdot \log (k_B T_0 B F)$ | |
| $= -103.6$ dBm | until 23 rd April 2007 |
| $= -98.6$ dBm | after 23 rd April 2007 |
| $k_B = 1.38 \cdot 10^{-23}$ J/K | Boltzmann's constant |
| $T_0 = 290$ K | standard temperature |
| $B = 1/\tau = 5$ MHz | receiver bandwidth |
| $F = 2.19 \Leftrightarrow \mathcal{F}_N = 3.4$ dB | receiver noise figure until 23 rd April 2007 |
| $F = 6.92 \Leftrightarrow \mathcal{F}_N = 8.4$ dB | receiver noise figure after 23 rd April 2007 |

There are other ways to evaluate the noise; one is to measure it directly at the receiver; the other involves the average of the power backscattered by a range gate, referred to as the noise gate, free from meteorological targets or plankton⁵. Usually the noise gate is chosen over 14 km. Considering that within a pulse cycle P_N stays nearly constant, in the practical use of MIRA-36 its value is measured at the noise gate at every pulse.

⁴With P (mW) expressed in milliwatt it follows $10 \log P(\text{mW}) = \mathcal{P}(\text{dBm})$ expressed in decibel relative to one milliwatt.

⁵With the term plankton in radar meteorology one means all the non-hydrometeorologic targets revealed from a radar system, that are normally insects, pollen, or birds.

3.3 Radar cross section for meteorological targets

The radar equation 3.16 is a function of properties of the radar set and properties of the scattering particles.

The properties of the radar set are known, and they are grouped in the radar constant, that includes the losses of the system.

The properties of the scattering particles depend on shape and size, number concentration, and thermodynamic phase, which all affect the amount of energy scattered back to the radar. Thus, the fundamental observable of a cloud radar is the reflectivity η , which through σ , as defined in equation 3.13, depends on the properties of all the scattering particles in a unit volume.

Meteorological scatterers have a variety of forms – from simply spherical droplets to awesome snow crystals –, a litre of air may contain some or millions of them, their dimension ranges from microns to millimetres, and they can be in liquid or solid thermodynamical state (see chapter 2 on cloud microphysics).

Let us imagine all the meteorological scatterers being spherical particles, and allow them only to vary with diameter D for the time being.

Mie (1908) had developed a theory that allow us to evaluate the backscattered energy of a sphere made of a uniform material. The theory predicts that the behavior of a spherical particle depends on the relation between the diameter D of the particle and the wavelength λ of the incident radiation. The limit cases are droplets large relative to the incident wavelength, which scatter in the optical region, and droplets small relative to the incident wavelength, which scatter in the Rayleigh region. The bounds of these regions are determined by the ratio between the circumference of the spherical particle and the incident wavelength:

$$\frac{\pi D}{\lambda} \begin{cases} \lesssim 1 & ; \text{Rayleigh region} \\ \gtrsim 1 & ; \text{optical region} \end{cases}$$

When the diameter D of a particle is much smaller than the incident electromagnetic wave the induced field can be approximated by a dipole field with the axis on the direction of the incident wave (Rayleigh scattering approximation); the induced field maintains the same frequency as the incident field and it is proportional to the number of molecules of the particle, that means that it is proportional to the volume of the particle $\left(\frac{4}{3}\pi\left(\frac{D}{2}\right)^3\right)$. In the Rayleigh approximation the power of the backscattered radiation is well approximated by:

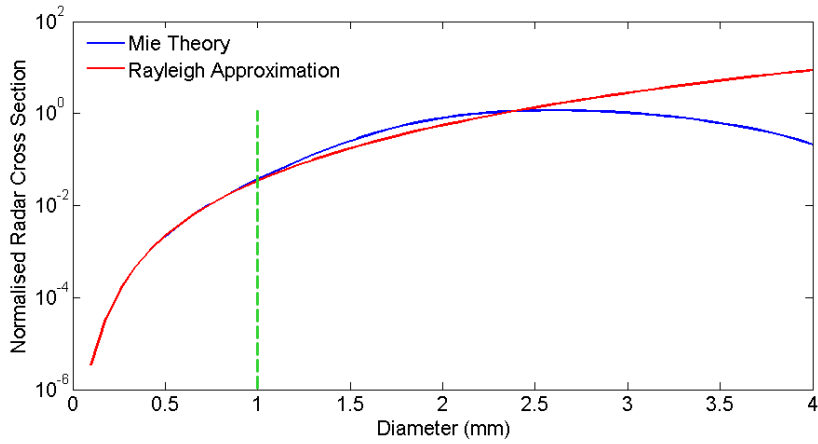
$$\sigma_i = \frac{\pi^5}{\lambda^4} |K_w|^2 D_i^6 \quad , \quad (3.20)$$

where K_w is the dielectric factor:

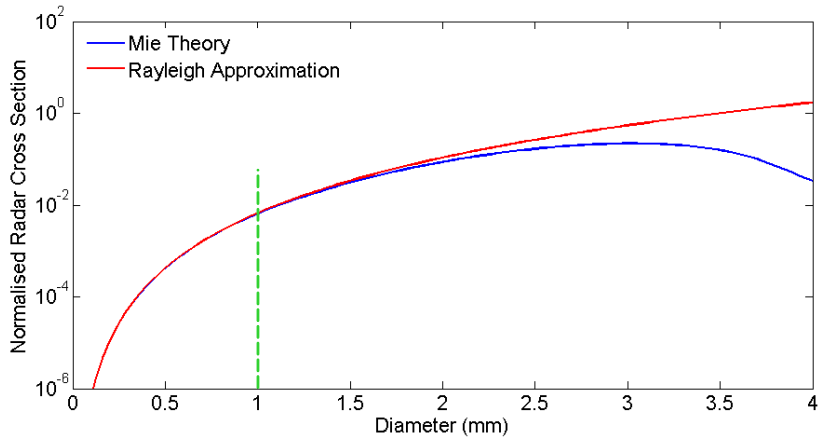
$$K_w = \frac{m^2 - 1}{m^2 + 2} \quad , \quad (3.21)$$

with m the complex index of refraction of liquid water.

Equation 3.20 is known as Rayleigh approximation: the backscattering cross-section



(a) Liquid water sphere



(b) Solid water sphere

Figure 3.4: Normalised radar cross section at a frequency of 35.5 MHz **(a)** for a liquid water sphere at a temperature of 10 °C (Liebe et al., 1991) and **(b)** for a solid water sphere at a temperature of -10 °C (Hufford, 1991).

increases linearly with the sixth power of the diameter of the scatterer.

In the case of MIRA-36, working with a wavelength of 8.45 mm, the limit for diameter of spherical liquid or solid water particles to behave in the Rayleigh approximation is shorter than 1 mm, as shown in figure 3.4. The refractive index model used for the scattering computations of a liquid water sphere has been developed by Liebe et al. (1991), and the one used for the scattering computations of a solid water sphere has been developed by Hufford (1991). Remembering that the greatest dimension of cloud particles - liquid droplets or ice crystals - is about 0.1 mm, whereas raindrops have maximum diameters ranging from 1 to 7 mm, we derive that at the wavelength of MIRA-36 cloud particles scatter in the Rayleigh

region, and raindrops scatter in the Mie region. We should note that in this section, for the sake of simplicity, we are treating spherical, liquid-made water particles. The most important point in 3.20 is that the backscattering cross-section is strongly dependent on the particle size, therefore the reflectivity η shows the same dependence:

$$\begin{aligned}\eta &= \frac{1}{V} \sum_V \sigma_i \\ &= \frac{1}{V} \frac{\pi^5}{\lambda^4} |K|^2 \sum_V D_i^6 \quad .\end{aligned}\quad (3.22)$$

In general, a litre of air in a warm cloud contains more than one billion droplets;

Resolution volume centered at 5 km in litres for MIRA-36:

$$\begin{aligned}V &= \frac{\pi\theta^2 c\tau}{2^4 \ln 2} \cdot r^2 = \\ &= 35 \cdot 10^3 \text{ m}^3 = 35 \cdot 10^6 \text{ l}\end{aligned}$$

$$\theta = 0.52^\circ = 0.00908 \text{ rad}$$

$$\tau = 200 \text{ ns}$$

a radar resolution volume – i.e. for the radar MIRA-36 a resolution volume at 5 km is constituted by $35 \cdot 10^6$ litres – contains a number of particles high enough to allow us to substitute the discrete sum over all the particles diameters with an integral of the continuous function Particle Size Distribution $N(D)$, with the particles uniformly distributed over the radar resolution volume. Thus it is clear that the radar reflectivity is the product of the concentration and of the radar cross section of the particles:

$$\eta = \frac{\pi^5}{\lambda^4} |K|^2 \int_0^\infty N(D) D^6 dD \quad ,\quad (3.23)$$

where $N(D) dD$ represents the number of particles per unit volume having diameter between D and $D + dD$.

The radar reflectivity represents the product of the concentration and of the radar cross section of the particles. The integral on the right end of the 3.23 takes the name of reflectivity factor Z :

$$Z = \int_0^\infty N(D) D^6 dD \quad (3.24)$$

that does not depend on the radar set and refers to spherical targets of unknown properties but the size; we also say that the reflectivity factor Z is given by the sixth moment of the Particle Size Distribution. Radar sets measure the reflectivity η , which is used to evaluate the reflectivity factor Z .

The strong dependence on the diameter entails that in a volume containing a distribution of particles, few relatively big particles dominate the backscattered power and obscure the power backscattered by a higher number of smaller particles. This point is referred to as the large droplet issue (Russchenberg and Boers, 2003). It has as a consequence that the Liquid Water Content LWC - proportional to the third power of the droplet diameters - is not evaluable directly only from reflectivity measurements, but other remote sensing systems should be additionally considered (as a synergy with Lidar, see Hogan and O'Connor, 2004). Moreover the cloud base height is not detectable in the presence of few rain drops or either few drizzle-like particles.

The units of η are area per unit volume, both expressed in metres (m^2/m^3), whereas by convention Z is expressed as the sixth power of millimetres per unit volume in metres (mm^6/m^3), to remind that it represents the sixth power of a diameter per unit volume.

The values of the reflectivity factor span many orders of magnitude, therefore radar meteorologists make use of a logarithmic scale:

$$\mathcal{Z}(\text{dBZ}) = 10 \log_{10} Z(\text{mm}^6/\text{m}^3) \quad , \quad (3.25)$$

where \mathcal{Z} on the left hand side is in the so-called dBZ units (decibel relative to the reflectivity factor) and Z on the right end side is in mm^6/m^3 units. Values of \mathcal{Z} range from -20 to 20 dBZ for clouds, and from 0 to as much as 60 dBZ for rainfalls. Let us write the equation 3.23 in function of the reflectivity factor Z , and let us substitute it in equation 3.15, so that the power backscattered is expressed as function of Z ; including the known constants of the backscattering cross section in the radar constant we obtain:

$$\begin{aligned} P_\sigma &= \frac{P_t G_0^2 \lambda^2 \theta^2 c \tau}{1024 (\ln 2) \pi^2 L} \frac{1}{r^2} \left[\frac{\pi^5}{\lambda^4} |K|^2 Z \right] \\ &= \frac{P_t G_0^2 \theta^2 c \tau \pi^3 |K|^2}{\lambda^2 1024 (\ln 2) L} \frac{1}{r^2} Z \\ &= \frac{\text{constant}}{r^2} Z \quad . \end{aligned} \quad (3.26)$$

The reflectivity factor evaluated inverting equation 3.26 turns to be a function of backscattered power and range:

$$Z = \frac{r^2}{\text{constant}} P_\sigma \quad . \quad (3.27)$$

Recalling equation 3.18, where P_m and P_N are measured quantities:

$$Z = \frac{r^2}{\text{constant}} (P_m - P_N) \quad . \quad (3.28)$$

We may also write, highlighting the contribution to the reflectivity factor due to the noise, Z_N :

$$Z = Z_m - Z_N \quad . \quad (3.29)$$

Using equation 3.19:

$$\begin{aligned}
 Z &= \frac{r^2}{\text{constant}} P_N \frac{(P_m - P_N)}{P_N} \\
 &= \frac{P_N}{\text{constant}} r^2 \text{SNR} \\
 &= C r^2 \text{SNR} .
 \end{aligned} \tag{3.30}$$

Specifying the units:

$$\begin{aligned}
 Z(\text{mm}^6/\text{m}^3) &= C(\text{m}) r^2(\text{m}) \text{SNR} \\
 \mathcal{Z}(\text{dBZ}) &= \mathcal{C} + 20 \cdot \log r(\text{m}) + \text{SNR}_{\text{dB}} ,
 \end{aligned} \tag{3.31}$$

with $\mathcal{C} = 10 \cdot \log C$ and $\text{SNR}_{\text{dB}} = 10 \cdot \log \text{SNR}$. The constant \mathcal{C} takes the name of weather radar constant. The value of \mathcal{C} for MIRA-36 is -92.47 dB, with the range provided in metre.

Weather radar constant of MIRA-36:

$$\mathcal{C} = 10 \cdot \log C = 10 \cdot \log \frac{\lambda^2 1024 (\ln 2) L P_N}{P_t G_0^2 \theta^2 c \tau \pi^3 |K_w|^2} = -92.47 \text{ dB}$$

$\lambda = 8.45$ mm

$\mathcal{L} = 3.6$ dB

$P_N = -98.6$ dBm

$P_t = 25$ kW

$G_0 = 89125$ (= 49.5 dB)

$\theta = 0.52$ °C = 0.00908 rad

$\tau = 200$ ns

$|K_w|^2 = 0.93$ [liquid water]

If MKS units are used to evaluate C , then the result must be multiplied by 10^{18} to return Z in mm^6/m^3 units, and the distance r of the target from the radar in equation 3.31 must be expressed in meters.

3.3.1 Equivalent reflectivity factor

So far equation 3.30, through equation 3.24, does not relate the power recorded by the radar system with the properties of the hydrometeors, because we need to know the phase of the particles and we need to assume a Particle Size Distribution PSD. Recalling the assumptions done up to now, the following ideal conditions need to be fulfilled for the weather radar equation to be valid: resolution volume completely and uniformly filled by the particles; particles spherical, liquid water made, and small enough to satisfy Rayleigh approximation.

When the above conditions are not met, the equivalent⁶ reflectivity factor Z_e is used in place of the reflectivity factor Z . This means that we rewrite equation 3.23 as:

$$Z_e (= Z) = \frac{\lambda^4}{\pi^5 |K_w|^2} \eta \quad . \quad (3.32)$$

where the equality in brackets is valid in the ideal case, and with K_w a function of the complex index of refraction of liquid water (see equation 3.21); in weather radar applications is still used an old value tabulated by Gunn and East in 1954: $|K_w|^2 = 0.93$. The convention of considering cloud and precipitation particles being made of liquid water is adopted because weather radars were first used to evaluate amount of rain, and it is still used because generally it is not known which kind of particles the resolution volume currently contains.

It being understood that the resolution volume is still supposed uniformly filled, if we conjecture that the radar resolution volume under study contains ice or snow, we should change the value of the index of refraction for water with the one for ice, that is $|K_i|^2 = 0.176$ for a density of 0.917 g/cm^3 , and we should use an expression of the backscattering cross section that is appropriate for irregular shaped particles. Rayleigh approximation is still valid for ice at the common weather radar wavelengths, because ice is a weak dielectric. This implies that the exact shape of the particle is inessential: the backscattering cross-section of an irregular particle composed by ice is similar to that of a uniform ice-made sphere with the same mass of the actual particle. It should be noted that Rayleigh approximation is anyway no more valid either in case of huge hailstone, nor in case of large wet particles.

The issue here is that radar systems are customized to measure Z_e , which means that an assumed dielectric factor is incorporated in the weather radar constant; nevertheless it is possible to evaluate the actual reflectivity from the equivalent one if the properties of the scatterers are known.

Smith (1984) has sketched how to properly connect Z with Z_e . We saw that for liquid spherical drops in Rayleigh approximation, the equivalent reflectivity factor Z_e is equal to Z (equation 3.32). Let us rewrite the reflectivity expression (equation 3.23) for irregular ice particles, by substituting the dielectric factor $|K_w|$ for liquid particles with the dielectric factor $|K_i|$ for ice particles, and by substituting the diameter D of a generic spherical particle with the diameter D_s of an equivalent ice

⁶In literature you may also find the term “effective” in place of “equivalent”.

sphere (i.e. the ice sphere having the same mass of the corresponding irregular ice particle):

$$\eta = \frac{\pi^5}{\lambda^4} |K_i|^2 \int_0^\infty N(D_s) D_s^6 dD = \frac{\pi^5}{\lambda^4} |K_i|^2 Z \quad ; \quad (3.33)$$

we obtain, using equation 3.33 in equation 3.32 :

$$\begin{aligned} Z_e &= \frac{|K_i|^2}{|K_w|^2} Z = 0.189 Z \\ Z &= \frac{1}{0.189} Z_e \quad , \end{aligned} \quad (3.34)$$

or, as logarithmic expression:

$$\mathcal{Z} = 7.2 \text{ dB} + \mathcal{Z}_e \quad .$$

This means that the measured reflectivity factor, Z_e , is smaller by a factor 0.189 than the actual one, Z . We may still maintain the value of Z_e , if we consider in place of D_s , the diameter of a liquid particle obtained by the complete melting of the ice one, D_m . The relation between D_m and D_s is given by:

$$D_m = D_s \sqrt[3]{\frac{\rho_i}{\rho_w}} = 0.97 D_s \quad , \quad (3.35)$$

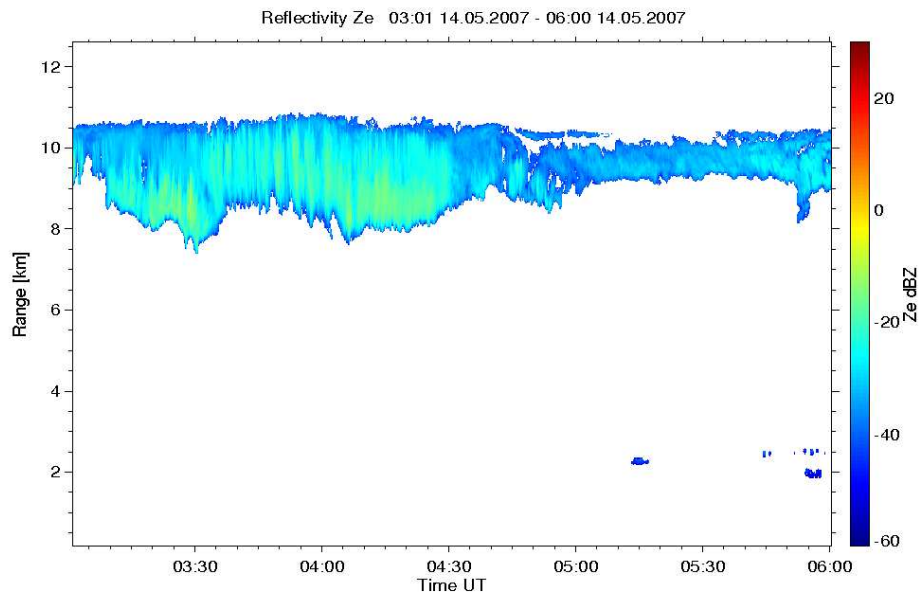
with the densities of ice and water being respectively $\rho_i = 0.9168 \text{ g/cm}^3$ and $\rho_w = 0.9998 \text{ g/cm}^3$. The use of alternative diameters for ice particles is necessary because they trap air in different amount, and the density of an ice particle may be as low as 0.05 g/cm^3 .

Typical values of equivalent reflectivity factor \mathcal{Z}_e , expressed on a logarithmic scale, are tabled for different cloud types in table 3.1, and examples of radar measurements by MIRA-36 for cirrus and stratus are shown in figure 3.5⁷.

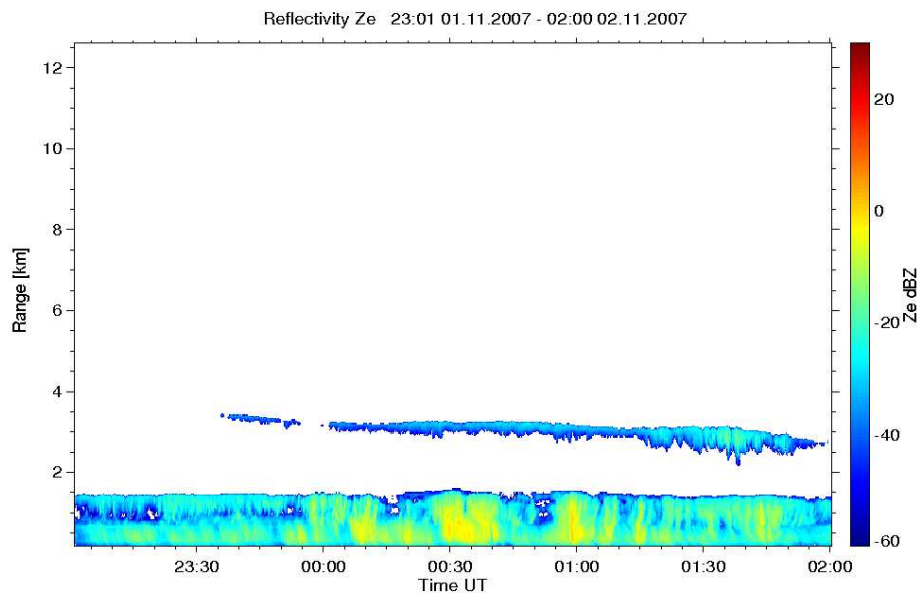
Table 3.1: Typical values of equivalent reflectivity factor for the radar system MIRA-36 placed in Lindenberg (DWD Meteorological Observatory). By Görzdorf (2009).

| Cloud type | Equivalent reflectivity \mathcal{Z}_e |
|-----------------------------|-----------------------------------------|
| Cirrus | −50 ... 0 dBZ |
| Fair weather cumulus | −50 ... −30 dBZ |
| Non-drizzling stratocumulus | −50 ... −30 dBZ |
| Stratocumulus with drizzle | −30 ... 10 dBZ |
| Light rain (drizzle) | −10 ... 10 dBZ |
| Moderate rain | 10 ... 30 dBZ |

⁷See section 3.10 for an explanation of Time–Height Indicators.



(a) Cirrus



(b) Stratus

Figure 3.5: Examples of radar equivalent reflectivity factor measured by the radar system MIRA-36 (Hamburg, 2007).

3.4 Attenuation

Electromagnetic waves propagating through the atmosphere are attenuated by gases and particles. The attenuation depends on the composition and concentration of the penetrated matter as well as on the wavelength. Attenuation due to liquid water is appreciable, and increases with decreasing wavelength. Corrections for attenuation by atmospheric gases and liquid water clouds are necessary for radar systems working at 94 GHz; but radar systems working at frequencies as low as 36 GHz do not suffer of strong attenuation from atmospheric gases or hydrometeors, as one sees in table 3.2 by Görsdorf (2009). Attenuation corrections below the melting layer could anyway be included using the algorithm developed by Hitschfeld and Bordan (1954).

Table 3.2: Attenuation coefficients in dB/km for 35 GHz radar separated for absorption by gases (h being the absolute humidity and with pressure $p = 1013$ hPa and temperature $T = 0$ °C) and extinction by rain (R being the rain rate). By Görsdorf (2009), after the formulation of Lhermitte (1990).

| | | |
|---------------------|-----------------------------|------------|
| Absorption by gases | $h = 0.25$ g/m ³ | 0.04 dB/km |
| | $h = 25$ g/m ³ | 0.35 dB/km |
| Extinction by rain | $R = 0.3$ mm/h | 0.06 dB/km |
| | $R = 10$ mm/h | 2 dB/km |

“Daddy?”

“Yes?”

“I want to be a scientist.”

XKCD.com/585

3.5 Doppler radar

All the particles in the radar resolution volume are moving in respect to the radar, each with its own velocity and each giving rise to a different echo signal. The single signals from every particle superpose linearly to give rise to the total echo. This echo is a radiation with the same wavelength of the initial incident radiation, but has intensity and phase fluctuating, as result of the random movements of the particles (figure 3.3). Note that the wavelength is of course also affected by the Doppler shift. Indeed the Doppler effect for microwave radars and for usual meteorological velocities is so small that it cannot be resolved in the short time of observation of backscattered signal from a single transmit pulse. It is rather reconstructed from the incremental phase shift of the backscattered signal for subsequent transmit pulses. The intensity of the echo is related to the distribution and to the size of the particles, as we saw in the foregoing sections (see in particular equations 3.24 and 3.26), whereas the shift in phase is due to the Doppler effect and hence it is related to the velocities of the particles in respect to the radar.

The radial velocity v_r of the target in respect to the radar system is related to the Doppler shift f_D by:

$$f_D = \frac{2}{\lambda} \cdot v_r \quad . \quad (3.36)$$

In case of vertically pointing radar, v_r represents the vertical component of the radial velocity of the particle, which we indicate as Doppler velocity v_D in the following. Thus a radar system that measures the shift in phase allows us to calculate the Doppler velocity of the particles through equation 3.36. A radar system with this capability is called Doppler radar, and it returns the Doppler spectral power density $\mathcal{S}_{f_D}(f_D)$, or Doppler spectrum, which is defined such that $\mathcal{S}_{f_D}(f_D) df_D$ represents the density of power backscattered by the particles having Doppler shifts in the range f_D to $f_D + df_D$.

Since signals are recorded in a discrete way, we need to reconstruct the continuous signal by computing the Fast Fourier Transform from a discrete number of samples (2^n points, $n = 6, 7, 8, \dots$). The radar emits a pulse of length τ ; then it waits for the echo for a time long T ; during T the signal received by the radar system (signal plus noise) is sampled every Δt_D , every sample corresponding to a subsequent range gate of Δr metres along the beam track (see equation 3.1). In order to reconstruct the signal we need to collect from the same range gate a number of samples high enough so that the samples are a complete representation of the signal, but small enough to can consider the particles remain in a stationary state, that means they not change their own velocity.

According to Nyquist theorem a maximum signal frequency f_M is associated to a frequency of sampling PRF (Pulse Repetition Frequency):

$$f_M = \frac{\text{PRF}}{2} \quad , \quad (3.37)$$

from which we calculate the maximum Doppler velocity range measurable as:

$$v_{DMax} - v_{Dmin} = f_M \frac{\lambda}{2} \quad . \quad (3.38)$$

The sign of the shift is related with a motion of the particles toward or away from the radar. The Doppler velocity resolution is given by:

$$\Delta v_D = \frac{v_{DMax} - v_{Dmin}}{N_{\text{FFT}}} \quad , \quad (3.39)$$

with N_{FFT} the number of points for the Fast Fourier Transform.

Then it is clear that by increasing N_{FFT} we increase the frequency (or velocity) resolution, but not the Nyquist range, that is instead driven by Pulse Repetition Frequency (and wavelength) of the specific radar system.

As said, instant by instant the power backscattered fluctuates, since the particles move randomly. Then to obtain a more realistic estimate of the behavior of the particles we could either perform a running average of one spectrum over a certain frequency interval, or a time averaging of successive spectra over a period of several multiples of the time needed to have one complete reconstructed spectrum of the received signal — the latter technique being the one used in the radar system MIRA-36.

The time averaged spectrum of a sampled series of spectrum $S_{f_D}(f_D)$ is $\overline{S_{f_D}}(f_D)$. Hence the expression for the time averaged power is:

$$\overline{P_m} = \int_{-\infty}^{+\infty} S_{f_D}(f_D) df_D \quad . \quad (3.40)$$

By virtue of equation 3.36, that expresses the Doppler frequency shift in terms of the radar wavelength λ and of the Doppler velocity v_D of the particles, we write, likewise equation 3.40:

$$\overline{P_m} = \int_{-\infty}^{+\infty} S_{v_D}(v_D) dv_D \quad , \quad (3.41)$$

where $S_{v_D}(v_D) dv_D$ is the time averaged spectrum of a sampled series of spectrum $S_{v_D}(v_D)$, representing the density of power backscattered by the particles having Doppler velocity in the range v_D to $v_D + dv_D$.

We know that the scattering particles are size distributed, that their number is large in the radar resolution volume and that they move independently with respect to one other. The single scattered electromagnetic waves superpose with constructive and destructive interference, giving rise to a signal that arrives to the radar with random phase and fluctuating intensity. The statistical error of the mean measured

intensity, and thus of the reflectivity factor Z , is given by $1/\sqrt{n}$, $n \gg 1$, with n the number of averaged spectra.

For MIRA-36 system, at the configuration used for this work, that is PRF = 5 kHz and $N_{\text{FFT}} = 256$, the time needed to have one complete reconstructed spectrum for every range gate is 51.2 ms (500 range gates of 30 metres), the Nyquist range goes from -10.625 m/s to $+10.625$ m/s, and the Doppler velocity resolution is 0.08 m/s.

The averaging time is 10.0352 seconds, that corresponds to average over 196 *raw* spectra.

The statistical error value for MIRA-36 for the averaging time of 10.0352 seconds is about 7%, that corresponds to 0.3 dB.

3.6 Gaussian spectra

The measured Doppler spectrum $S_{v_D}(v_D)$ is the convolution of functions describing several factors.

The convolution of two signals $h(t)$ and $x(t)$ is defined as:

$$y(t) = h(t) \otimes x(t) = \int_{-\infty}^{+\infty} h(\xi)x(t - \xi)d\xi \quad (3.42)$$

It can be proved that the spectrum of $y(t)$ is given by the product of the spectra of $h(t)$ and $x(t)$, that is:

$$Y(f) = \mathcal{F}_T[y(t)] = \mathcal{F}_T[h(t) \otimes x(t)] = \mathcal{F}_T[h(t)] \mathcal{F}_T[x(t)] = H(f)X(f) \quad (3.43)$$

as a property of the Fourier transform \mathcal{F}_T .

The first contribution to the measured Doppler spectrum is due to the particle fall velocity distribution.

A broadening of the spectra is caused by the dwell time, that is the time of residence of the particles in the radar resolution volume. This factor is anyway negligible for the radar system used in this work.

The spectra could be affected by wind shear or droplet size distribution broadening, specifically, the dominating effect to the shape of a Doppler spectrum is the broadening due to turbulent motion of the air.

Thus the measured Doppler spectrum is the convolution of the still air Doppler velocity spectrum with the turbulent velocity probability density function, which is usually assumed to be Gaussian (Gossard et al., 1997). In the ideal case we suppose that the particles in the resolution volume are of the same type and have the same dimensions, so in steady air they move with the same velocity. Therefore the fall velocity is a Dirac's delta function.

Since the convolution of a Dirac's delta function with a Gaussian function is still a Gaussian function, we can reasonably assume Doppler spectra of cloud signals being Gaussian-shaped.

3.7 Polarimetric radar

The identification of the hydrometeors just using reflectivity factor and Doppler velocity is a challenge because, for example, little droplets can produce an echo similar to the one of larger ice crystals.

Polarimetric radar systems provide information on the shape of the sensed hydrometeors, on their fall orientation related to the radar beam direction, and on their refractive index and bulk density. More and more radar systems are nowadays equipped with polarimetry control for the emitted and received waves. Linearly polarized electromagnetic waves oscillate on one well defined plane, called the polarization plane. Common configurations for cloud radars use linear, circular, or elliptical polarized waves. Radar system MIRA-36 emits waves on one linear polarized plane H , and measures waves on the same plane H and on the orthogonal plane V . This radar is vertically pointing, and indeed for vertically pointing radar systems the direction of polarization is inessential; we maintain the labels of H (horizontal) and V (vertical) polarization following the conventional notation for slanted-looking radars.

The study of the polarization of the received waves, compared with the polarization of the emitted one, allows us to infer the asymmetry of the particles, so that we can distinguish spherical droplets from asymmetric snow crystals.

The measure of the asymmetry of the particles is called Linear Depolarization Ratio LDR, and is given by the ratio between the signal received on the vertical polarization plane and the signal received on the horizontal polarization plane; in decibel:

$$\text{LDR}_{\text{dB}} = 10 \cdot \log_{10} \left(\frac{Z_{VH}}{Z_{HH}} \right) . \quad (3.44)$$

In the suffixes in equation 3.44 the first letter indicates the received polarization plane, and the second letter the emitted polarization plane; then, since we are interested in systems with only one plane of polarization for the emitted wave, Z_{VH} is the reflectivity received on the vertical polarized plane, or cross-polar plane (cx-channel), and Z_{HH} is the reflectivity received on the horizontal polarized plane, or co-polar plane (co-channel).

With the term depolarization we mean that part of a linearly polarized wave incident on a target that starts to oscillate on a different polarization plane, so that there is a distribution of the incident energy among all the possible oscillation planes. Let us imagine a liquid particle with cross-section oblate with respect to the radar line of sight. Let us also consider that the incident wave has a plane of polarization in respect to the line of sight aligned as illustrated in figure 3.6. Let us decompose the incident field E_i in two arbitrary components E_{iX} and E_{iY} (figure 3.6a); as the choice of these components does not change the final result, we consider two orthogonal axis XY oriented at 45° degrees in respect to the incident wave (T. Otto, personal communication). The two components E_{iX} and E_{iY} of the incident wave induce in the particle the fields $E_{\sigma X}$ and $E_{\sigma Y}$ (figure 3.6b) oriented parallel to their directions, such that the power (P_x and P_y) of the backscattered waves are proportional to the

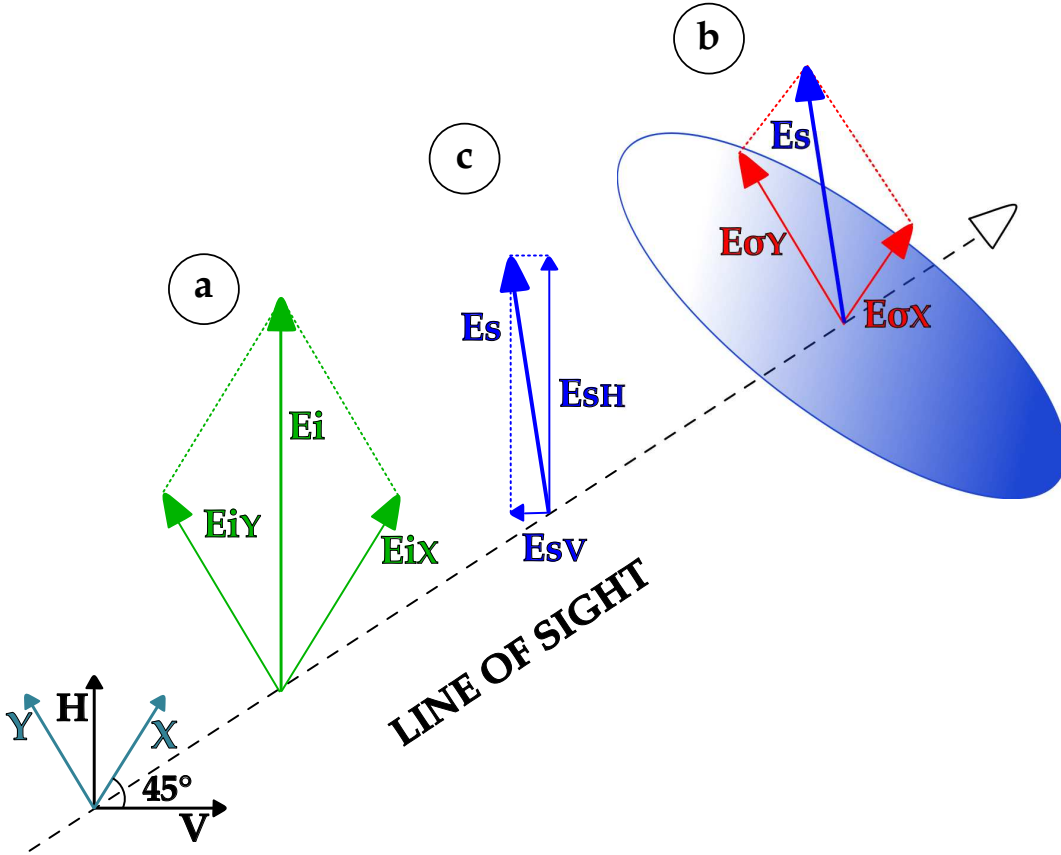


Figure 3.6: Depolarization of waves incident on oblate particles. **a**: incident wave decomposed on two arbitrary orthogonal components (XY); **b**: components of the field induced on an oblate particle and backscattered wave due to their composition (XY); **c**: backscattered wave decomposed on the polarization planes (HV).

backscattering cross sections σ_x and σ_y , that in the Rayleigh approximation depend on the 6th power of the length of the section of the liquid particle along the considered component. The composition of E_{σ_X} and E_{σ_Y} results in a backscattered wave with field E_s that is not necessarily oriented along the incident polarization plane. Let us decompose again E_s on the plane individuated by the axis H and V , H oriented along the incident polarization plane and V oriented orthogonally to it (figure 3.6c). If the component E_{sV} of E_s along the V axis is not zero, than the transmitted wave E_i has been depolarized. If the liquid particle has a spherical cross-section with respect to the line of sight of the radar, there is no depolarized component, the depolarization ratio E_{sV}/E_{sH} is zero, and the value of the LDR_{dB} (see equation 3.44) tends to $-\infty$. Practically there is a limit in measuring the depolarized component, depending on the goodness of the separation of the waveguides in the radar system, as any imperfection of the antenna will produce a cross-polarized component. For MIRA-36 radar system the lowest limit for the LDR_{dB} is about -35 dB.

If the liquid particle has a cross-section oblate with respect to the line of sight of the radar, the maximum possible depolarization results when E_s is oriented such that its projections on the H and V axis, E_{sH} and E_{sV} , have the same intensity. In this case the the depolarization ratio E_{sV}/E_{sH} is one and the value of LDR_{dB} is then zero.

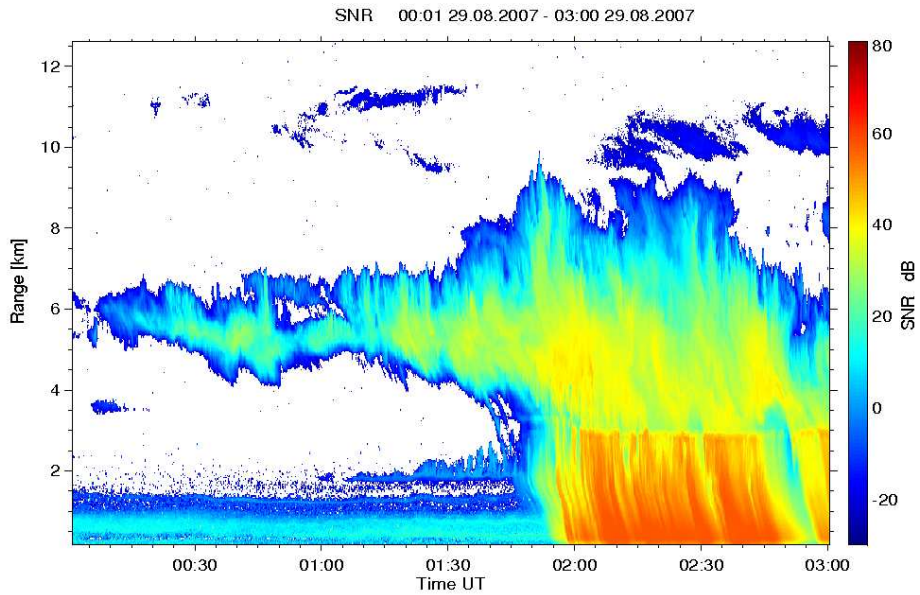
The things became more complicated by the elaborate shapes of the ice crystals. Hence from the LDR_{dB} values we just infer how much aspherical is the section of the particles. Moreover, ice has a small index of refraction, therefore the value of LDR_{dB} might not be always measurable for the smaller ice crystals.

The LDR_{dB} is also used as an indicator of the melting layer, since it was observed that its value consistently increase in this part of the clouds. The reason for this behavior of the LDR_{dB} is still not clear, even though several explanations were suggested (Kowalewski and Peters, 2010). The most invoke process is that the ice particles begin to melt at 0°C from their external part; the liquid film of water distributes around the still solid particle until the complete melting; during this melting process the wet particles produce a greater value of the depolarized wave, as a consequence of the increasing of the index of refraction.

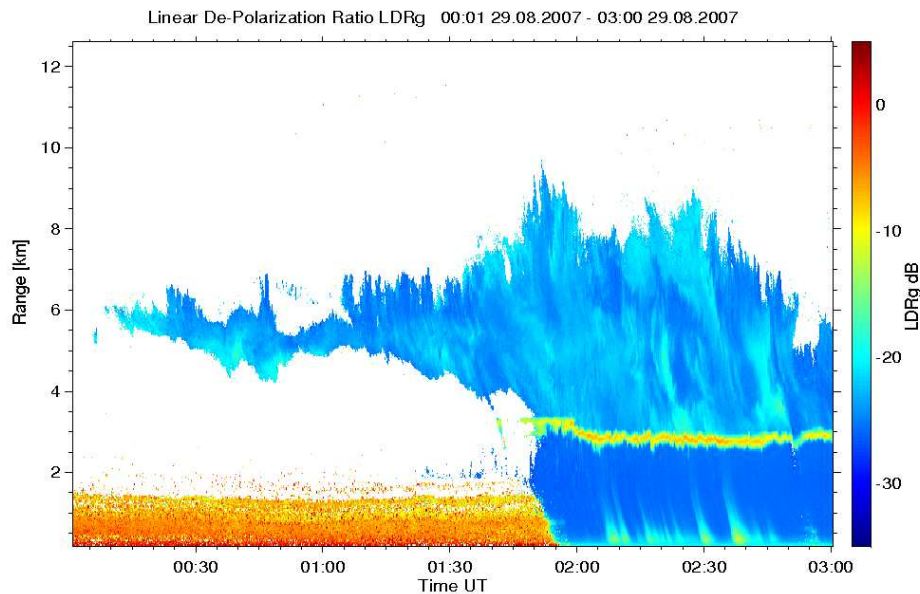
Ground clutter and plankton, although they show the same reflectivity of cloud particles, can be distinguished from hydrometeors by studying the values of the LDR_{dB} . Indeed, being largely not spherical, this kind of targets gives rise to a larger cross-polarized component, and therefore has a larger LDR_{dB} than the hydrometeors (figure 3.7). Typical signature of LDR_{dB} for different targets as measured are given in table 3.3.

Table 3.3: Typical values of LDR_{dB} measured by the radar system MIRA-36 placed in Lindenberg (DWD Meteorological Observatory). By G6rsdorf (2009).

| LDR_{dB} | class of targets |
|--------------------------|--------------------|
| $-30 \dots -10$ dB | mixed phase clouds |
| $-25 \dots -10$ dB | ice clouds |
| $-20 \dots 0$ dB | melting layer |
| $-10 \dots 0$ dB | insects |



(a) Signal to Noise Ratio



(b) Linear Depolarization Ratio

Figure 3.7: Example of Signal to Noise Ratio and respective Linear Depolarization Ratio measured by the radar system MIRA-36 (Achern, Germany, 2007, within the COPS campaign (Wulfmeyer et al., 2008)). In the lower panel, the reddish layer up to 2 km is atmospheric plankton (insects, pollen, etc.); note that the SNR of the plankton is similar to the cloud particles one, so that they are distinguishable only by their LDR signatures. The red tiny layer at 3 km is the melting layer. Little ice particles (between 9 and 12 km) visible in the SNR, have a not measurable LDR. See section 3.10 for an explanation of Time–Height Indicators.

3.8 Phase noise

The radar system MIRA-36 utilizes a magnetron as resonator (the source of electromagnetic waves). The magnetron developed for MIRA-36 is particularly stable in terms of intensity and wavelength of the emitted radiation, but it is not a coherent resonator, that means that the phase of subsequent pulse is arbitrary. That implies that the phase⁸ Φ_n of the emitted wave need to be measured at every pulse n . Due to uncertainties in this measurement, a further source of noise need to be considered in addition to the thermal noise P_N : the phase noise. The main consequence of the presence of the phase noise is that the noise floor in the spectra will not be constant, but will increase its value with the intensity of the corresponding received wave.

Let us analyze the details of this process, rising from the “coherent on receiver” technology, as described by Peters (2009b). The signal emitted at the pulse n is $S_n(t)$ (see section 3.5). For the sake of simplicity let us normalize the signal to:

$$e_n(t) = e^{[i(\omega t + \Phi_n)]} \quad , \quad (3.45)$$

with t the time elapsed after the leading edge of the transmit pulse. The copy of the signal stored for the next coherent processing is:

$$e_n'(t) = e^{[i(\omega t + \Phi_n + \varphi_n)]} \quad , \quad (3.46)$$

whit φ_n a random uncertain phase. The received signal from a distance r_n (see equation 3.1) is:

$$E_n(t) = E e^{[i(\omega(t - \frac{2r_n}{c}) + \Phi_n)]} \quad , \quad (3.47)$$

with E the amplitude of the signal. Considering each particle moving with the same velocity v , mean of the velocities of all the particles involved in the scattering, we can express the mean range r_n of these particles as:

$$r_n = r_0 + v n T \quad , \quad (3.48)$$

with r_0 the mean range at $n = 0$, and T pulse repetition time. Then equation 3.47 turns in:

$$E_n(t) = E e^{[i(\omega(t - \frac{2r_0}{c} - \frac{2vnT}{c}) + \Phi_n)]} \quad . \quad (3.49)$$

The next step of signal processing is “mixing” the received signal into the base band (transmitted signal), by means of a multiplication of the received signal with the complex conjugate of the transmitted signal according equation 3.46:

$$m'(n) = E e^{[-i(2r_0k + 2vnTk - \varphi_n)]} \quad , \quad (3.50)$$

⁸We need to know the phase of the electromagnetic waves emitted and received to evaluate the Doppler shift (see section 3.5).

with $k = \omega/c$ the wave number; note that the dependency on the time t canceled. The first phase term is fixed and is determined by the position of the targets during the first pulse. The second phase term describes the Doppler shift. The third phase term is the random phase measurement uncertainty. If, for simplicity of notation, we assume that the first and second terms are zero, then:

$$m(n) = E e^{-i\varphi_n} \quad . \quad (3.51)$$

For small variation of φ_n , that means $\varphi_n \ll 1$, we can approximate equation 3.51 with:

$$m(n) = E \left(1 - i \varphi_n \right) \quad . \quad (3.52)$$

As described in section 3.6, the power spectrum (Doppler spectrum) is given by the Fourier transform of the auto covariance function of the signal. The auto covariance function of equation 3.52 is:

$$\begin{aligned} \text{acf} \{m(n')\} &= E^2 \cdot \left(\underbrace{\frac{1}{N} \sum_{n=0}^{N-1} 1}_1 - \underbrace{\frac{i}{N} \sum_{n=0}^{N-1} \varphi_n}_0 - \underbrace{\frac{i}{N} \sum_{n=0}^{N-1} \varphi_{n'}}_0 + \underbrace{\frac{1}{N} \sum_{n=0}^{N-1} \varphi_{n'} \varphi_n}_{\text{var}\{\varphi\} \delta(n,n')} \right) \\ &= E^2 (1 + \text{var}\{\varphi\} \delta(n, n')) \quad , \end{aligned} \quad (3.53)$$

with $\text{var}\{\varphi\}$ the variance of φ , and $\delta(n, n')$ the Kronecker delta, defined by:

$$\delta(n, n') = \begin{cases} 1 & \text{if } n = n' \\ 0 & \text{if } n \neq n' \end{cases} \quad . \quad (3.54)$$

The discrete Fourier transform $\mathcal{F}_{\mathcal{T}}$ of the auto covariance function 3.53 is:

$$\mathcal{S}(j) = \mathcal{F}_{\mathcal{T}} [\text{acf} \{m(n')\}] = E^2 \delta \left(\frac{2\pi j}{T}, 0 \right) + E^2 \text{var}\{\varphi\} \quad , \quad j = 0, 1, 2, \dots \quad . \quad (3.55)$$

The first term of 3.55 is the signal peak with zero Doppler shift, whereas the second term is the frequency-independent noise power in each frequency bin due to the measurement uncertainty of φ .

A usual representation of the phase noise power is obtained by normalization with respect to the signal power E^2 (referred to as ‘‘carrier power’’) and with respect to the frequency bin width $1/T$:

$$P_{N\Phi} = \text{var}\{\varphi\} T \quad . \quad (3.56)$$

Often a logarithmic presentation in decibel is preferred, which is:

$$\mathcal{L} = 10 \cdot \log P_{N\Phi} \quad , \quad (3.57)$$

with units dBc, where c indicates the ‘‘carrier’’.

Typical values for MIRA-36 are about $\mathcal{L} = -35$ dBc/Hz.

3.9 Moments of the Doppler spectrum

We saw in a last section (3.6 at page 46) that a Fourier transform converts a time series of backscattered power in a series of reflectivities each one associated with a different velocity of the particles, the Doppler spectrum. Considering the Doppler spectra be a continuous probability density distributions, the moments of the Doppler spectrum are defined⁹ as the normalized statistical moments of the Doppler spectrum:

0^{th} **moment** i.e. the received power:

$$\langle v^0 \rangle = \int_{-\infty}^{+\infty} S_{v_D}(v_D) dv_D = \overline{P_m} \quad . \quad (3.58)$$

1^{st} **moment** i.e. the mean Doppler velocity (reflectivity weighted):

$$\langle v^1 \rangle = \frac{\int_{-\infty}^{+\infty} v_D S_{v_D}(v_D) dv_D}{\int_{-\infty}^{+\infty} S_{v_D}(v_D) dv_D} = \overline{v_D} \quad . \quad (3.59)$$

2^{nd} **central moment** i.e. the square of the Doppler spectrum width (or Doppler velocity width):

$$\langle v_c^2 \rangle = \frac{\int_{-\infty}^{+\infty} (v_D - \overline{v_D})^2 S_{v_D}(v_D) dv_D}{\int_{-\infty}^{+\infty} S_{v_D}(v_D) dv_D} = \sigma_v^2 \quad . \quad (3.60)$$

Trough equation 3.30 we see that the 0^{th} moment represents, with the appropriate conversions and units, the reflectivity of the particles in a resolution volume, and then that the reflectivity can be evaluated by calculating the area under the Doppler spectrum $S(v_D)$. Recalling equations 3.41 and 3.28, we see that, for any fixed range, the reflectivity factor Z is directly proportional to the total power received by the radar system, and, therefore, it is equal, up to an arbitrary constant, to the integral of the measured Doppler spectrum $S_{v_D}(v_D)$:

$$\left. \begin{array}{l} 3.41 \Rightarrow \overline{P_m} = \int_{-\infty}^{+\infty} S_{v_D}(v_D) dv_D \\ 3.28 \Rightarrow Z = \frac{r^2}{\text{constant}} (P_m - P_N) \end{array} \right\} \Rightarrow Z \propto \int_{-\infty}^{+\infty} S_{v_D}(v_D) dv_D \quad . \quad (3.61)$$

The mean Doppler velocity is expressed by the reflectivity weighted distribution of the Doppler velocities of the particles within the scattering volume. We should remember this point when comparing the mean Doppler velocity measured by a radar system, that represents the mean velocity of the particle in the scattering volume, with the terminal fall velocity (see equation 2.10 or equation 2.12), that

⁹Similarly to the statistical moments of a continuous random variable, the n-th moment of a distribution is the expected value of the n-th power of the variable, and the n-th central moment of a distribution is the expected value of the n-th power of the deviations from the 1^{st} moment.

predicts the fall velocity of a single cloud particle.

It is clear, therefore, that the moments of the Doppler spectrum, that are received power, mean Doppler velocity, and spectrum width, fully characterize the Doppler spectrum, if it is assumed Gaussian (see figure 3.8); nevertheless, if the Doppler spectrum deviates from a symmetric, Gaussian model, we should expect a bias in the mean Doppler velocity and spectrum width estimators.

In the following the first three moments will be referred to as global moments of the spectrum, since they denote microphysical property of the whole ensemble of particles in the scattering volume.

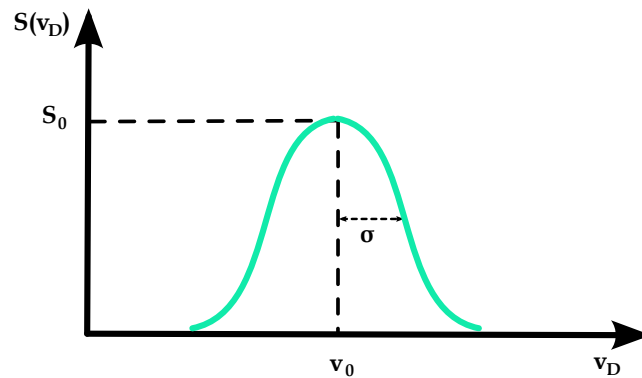


Figure 3.8: Gaussian model of the Doppler spectrum. The moments of the Doppler spectrum, nominally the received power $\overline{P_m}$, the mean Doppler velocity $\overline{v_D}$, and the spectrum width σ , are estimated from the parameters of the Gaussian curve, respectively maximum value S_0 , center v_0 , and standard deviation σ_v .

By using the moments of the Doppler spectra we evaluate meaningful meteorological parameters, such as, for example, the extension of the clouds and its liquid or ice water content, and microphysical properties. The intensity of the backscattered power gives us information on the cloud particle phase, as liquid water scatters back higher amount of power than solid one; from the Doppler velocity we can derive diameter of the particles as ice particles and little cloud droplets fall with terminal velocity of about 2 m/s, whereas snow has relatively higher fall velocity, and rain reach velocities even faster than 5 m/s. The LDR_{dB} tells us how asymmetric the particles are, allowing us to distinguish the irregularly shaped hydrometeors, as snowflakes, from spherical droplets. Combining the moments of the Doppler spectrum with ceilometers and microwave radiometer measurements, Illingworth et al. (2007) have been able to classify hydrometeors on a continuous basis.

3.9.1 The spectral reflectivity factor

The data acquisition software of MIRA-36 system provides values of the output signals in so called Engineering Units (EU); that means that these values are proportional to the physical quantity of interest, but they need to be calibrated before we can connect the output numbers with the physical phenomena we are measuring. The primary measured values of the radar are spectral powers $p_{raw,i}$ in EU. To derive the calibration constant between primary values and spectral radar reflectivity z_i in mm^6m^{-3} we follow the indications given by Peters (2010).

Let us define the total power at the receiver input in engineering units P_{raw} as:

$$P_{raw} = \sum_{i=0}^{255} p_{raw,i} \quad , \quad (3.62)$$

with the index of the sum covering the 256 bins of the spectrum.

Similarly to the total power we define the total receiver noise measured at the noise gate (14 km) in EU as:

$$N_{T,raw} = \sum_{i=0}^{255} n_{T,raw,i} \quad , \quad (3.63)$$

with $n_{T,raw,i}$ the spectral total noise at the noise gate.

The noise derived after the application of Hildebrand and Sekhon method (see section 4.4 for more details) is:

$$N_{HS,raw} = 256 \cdot n_{HS,raw} \quad , \quad (3.64)$$

again with the total noise $N_{HS,raw}$ and the spectral noise $n_{HS,raw}$ in EU. Note that Hildebrand and Sekhon noise level is constant along the spectrum.

The radar software returns as a global moment the Signal to Noise Ratio SNR, dimensionless, given by (compare with equation 3.19):

$$\text{SNR} = \frac{P_{raw} - N_{HS,raw}}{N_{T,raw}} \quad . \quad (3.65)$$

From equation 3.30 the radar reflectivity factor Z , in EU, can be expressed as:

$$Z = C r^2 \text{SNR} \quad , \quad (3.66)$$

with C constant of proportionality (whose logarithm represents the weather radar constant), and r the range gate height in metre. In the same manner of equation 3.65 we can define the spectral signal to noise ratio as:

$$\text{snr}_i = \frac{p_{raw,i} - n_{HS,raw}}{N_{T,raw}} \quad , \quad (3.67)$$

so that the total SNR can be also write as:

$$\text{SNR} = \sum_{i=0}^{255} \text{snr}_i \quad . \quad (3.68)$$

and equation 3.66 can be write as:

$$Z = \sum_{i=0}^{255} C r^2 \text{snr}_i \quad . \quad (3.69)$$

Let us express the spectral reflectivity z_i in $\text{mm}^6 \text{m}^{-3}$ such as:

$$Z = \sum_{i=0}^{255} z_i \quad , \quad (3.70)$$

that then brings to:

$$z_i = C r^2 \text{snr}_i \quad . \quad (3.71)$$

If we wish to express z_i by the measured quantities (EU), we substitute equation 3.67 to snr_i :

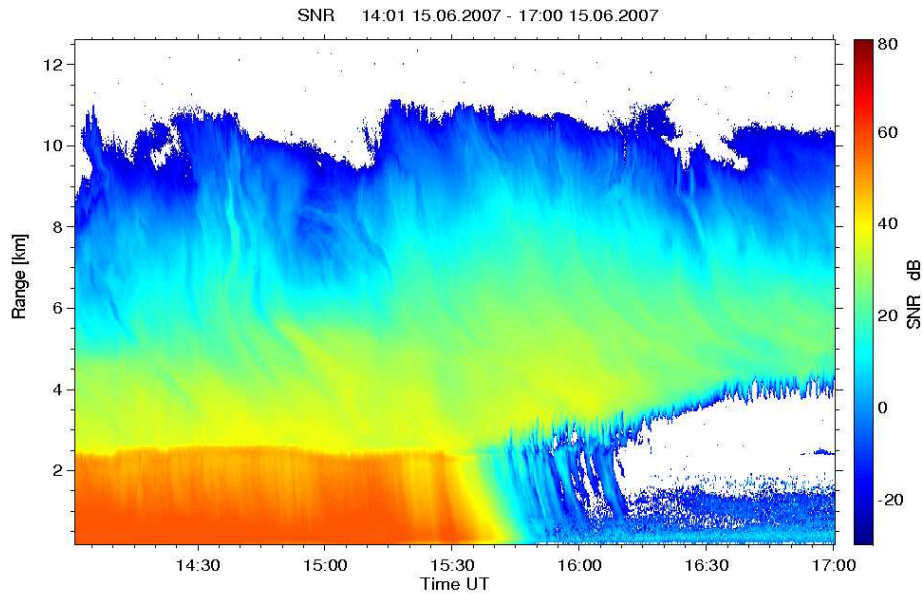
$$z_i = C r^2 \frac{P_{\text{raw},i} - n_{\text{HS,raw}}}{N_{T,\text{raw}}} \quad , \quad (3.72)$$

from which finally Z can be evaluated.

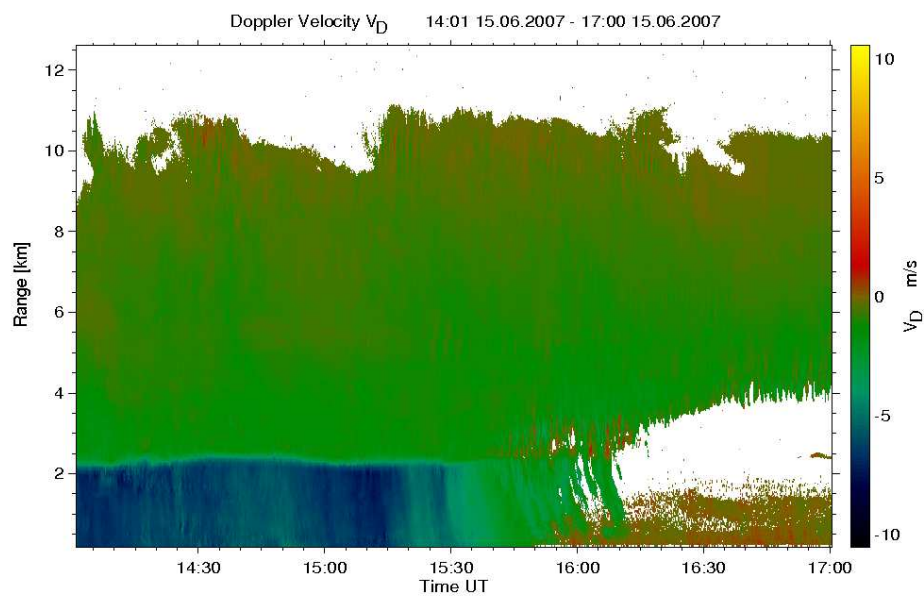
3.10 Graphical representation of measurements by vertically pointing radar systems

In case of vertically pointing radars the usual way to visually represent the global moments, the LDR, and additional meteorological variables, is to use a Time–Height Indicator (THI). A THI has the time on the X–axis and the height range from the radar on the Y–axis. To every point on this XY–space it is assigned a color, representing the magnitude of the represented variable; the reference values are indicated on a scale on a side panel. One can ultimately consider a THI as the vertical section of a cloud as the cloud passes over the radar system.

The panels in figure 3.9 illustrate an example of global moments and LDR measured by MIRA-36 in Hamburg on 15th June 2007 . The period here shown (from 14:00 until 17:00) is dominated by a stratiform cloud from about 2 to 11 km. The melting layer is recognizable at 2.5 km until 16:00 by the sharp increase of reflectivity and the high LDR values. Below it, heavy rain is characterized by high values of reflectivity and spectral width as well as by significant values of the vertical velocity. After 16:00, the signal below 2 km is dominated by atmospheric plankton with high values of LDR.

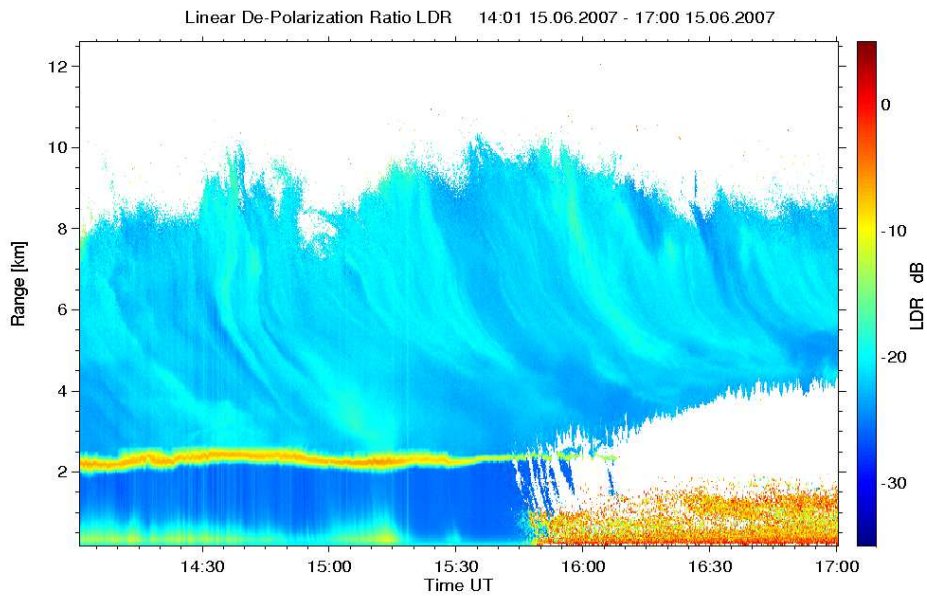


(a) Signal to Noise Ratio

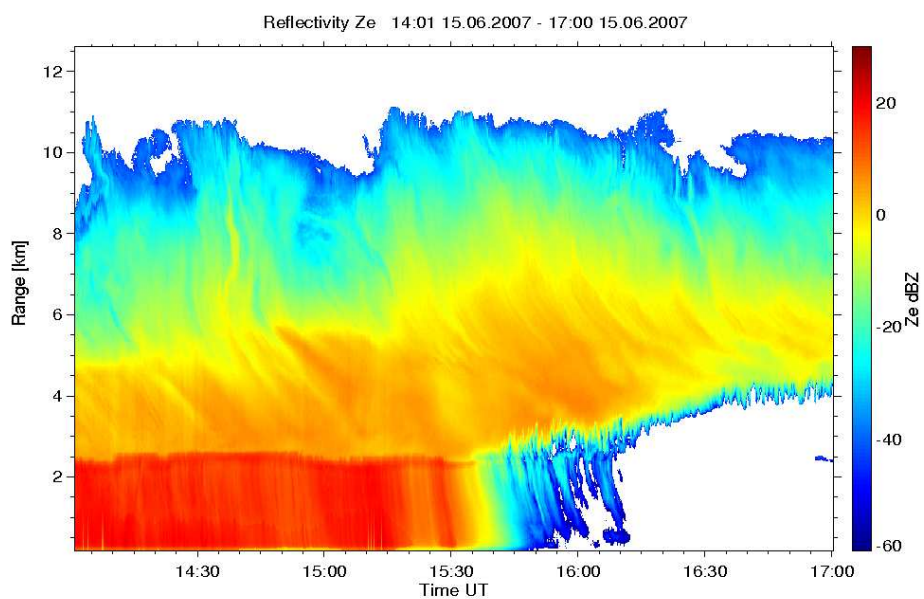


(b) Doppler fall velocity

Figure 3.9: Examples of Time–Height Indicators. THI for the SNR, Doppler velocity, LDR, and equivalent reflectivity factor measured with cloud radar MIRA-36 in Hamburg (2007).



(c) Linear Depolarization Ratio



(d) Equivalent reflectivity factor

Figure 3.9: Cont. In the equivalent reflectivity factor the atmospheric plankton is filtered by using an algorithm developed at METEK (Bauer-Pfundstein and G6rsdorf, 2007)

3.11 Radar specifications of MIRA-36

During this chapter we saw how radar systems work, and we evaluate some values for the radar system MIRA-36. In this section (table 3.4) we recall the basics value for MIRA-36, and the special settings used for this work, which represents a compromise of good resolution and acceptable storage requirements.

All the measurements considered in this work were taken in Hamburg by the 35-GHz vertically pointing Doppler radar MIRA-36 in the period going from August 2006 to May 2007.

Table 3.4: Specifications for the cloud radar MIRA-36. The operational parameters indicated are valid for the measurements considered in this work. For more details about the radar see the radar user manual (METEK documentation, 2006).

| Parameter | Value |
|-----------------------------|----------|
| Frequency | 35.5 GHz |
| Wavelength | 8.45 mm |
| Peak power | 30 kW |
| Pulse Repetition Frequency | 5 kHz |
| Pulse length | 200 ns |
| Range resolution | 30 m |
| Antenna diameter | 1.2 m |
| Beamwidth | 0.52° |
| FFT length | 256 |
| Doppler velocity resolution | 0.08 m/s |
| Integration time | 10 ns |
| Minimum range | 150 m |
| Maximum range | 15 km |
| Minimum detectable LDR | -35 dB |

Chapter 4

Development of the decomposition algorithm

4.1 Introduction

In order to characterize clouds by Doppler radar measurements, radar meteorologists use the global moments of the Doppler spectrum. As explained in the previous chapter, a Doppler spectrum is determined by the power backscattered by the hydrometeors in function of their radial Doppler velocity. Sustained by the considerations outlined in section 3.6, in this work we assume that cloud particles produce spectra with a Gaussian shape. More specifically, an ensemble of cloud particles of the same species — the same thermodynamic phase, analogous shape and size — produces a Gaussian spectrum, henceforth defined as a mode, with characteristic parameters, which are related to the global moments of the Doppler spectrum (see section 3.9, for the definition of the moments of the Doppler spectrum).

Traditionally the moments of the Doppler spectrum are evaluated considering the spectra due to only one mode of particles. Thus, in case of clouds producing Doppler spectra composed of more modes, the extraction of cloud microphysical parameters by using the global moments leads to incomplete, when not erroneous, retrievals, as for example a shifted mean Doppler velocity, or a too wide spectral width.

To overcome this lack, we have developed an algorithm capable of decomposing the spectral modes of the Doppler spectra, from which it is possible to evaluate mode-specific moments (in opposition with respect to the global moments). Therefore deeper information on the structure of a cloud can be extracted.

In this chapter we will illustrate the decomposition technique developed to decompose the Doppler spectra with some results obtained by using this algorithm. All the routines constituting the algorithm are written in IDL¹.

¹<http://www.itvis.com/ProductServices/IDL/tabid/63/language/en-US/Default.aspx>

It isn't I cannot see the solution;
it is I cannot see the problem.

4.2 Overview of the decomposition algorithm

The basic flow chart illustrating the steps of the decomposition algorithm is depicted in figure 4.1.

We start our analysis from preprocessed data: we consider spectral powers $p_{raw,i}$, already averaged in time, the averaging time being about 10 seconds, as described in the last part of section 3.5.

The main step is to fit every spectrum with the function describing the spectral model chosen for the decomposition. A detailed description of the spectral model is given in section 4.3.

In order to simplify the decomposition process, the first operation to do is to remove the noise floor. The algorithm we develop individuates the noise level for every spectrum by using a method suggested by Hildebrand and Sekhon (1974). This routine is described in section 4.4. For the analysis that follows we use the spectra devoid of the noise. The noise level is considered again when calculating the power of the meteorological signal (see also section 3.8).

The automatic fitting procedure could give results that have no physical meaning, thus we need to settle several checks, so that only plausible modes would be returned. We also formulate a separability criterion among more modes. See section 4.5 for details.

Once the characteristic parameters of the spectral model are individuated, we use the final products, that means the global moments, to properly calibrate the mode-specific spectral powers, as we will explain in section 4.6.

Microphysical retrievals obtained applying this algorithm are presented in chapter 5.

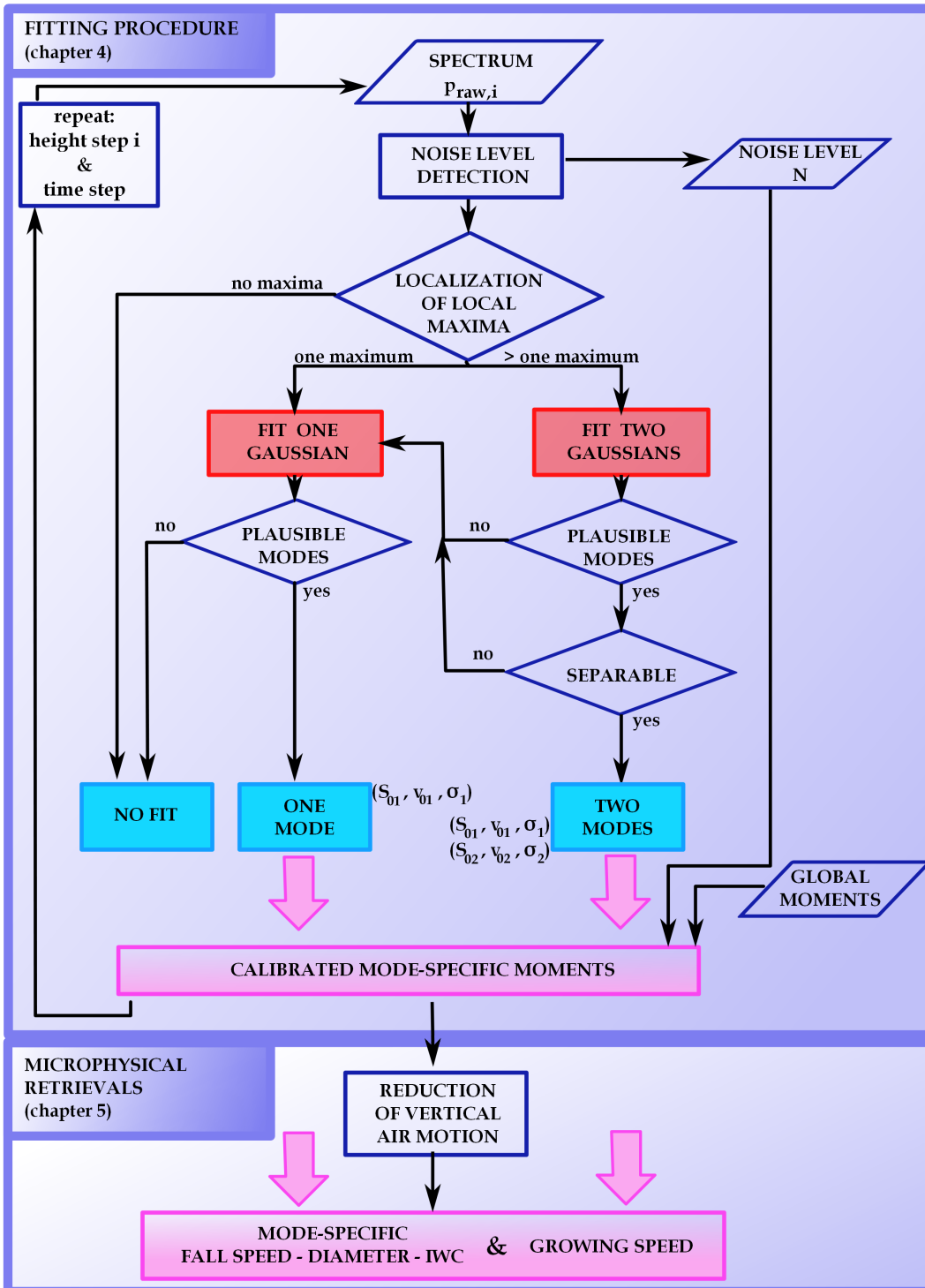


Figure 4.1: Flow chart of the decomposition algorithm.

4.3 The spectral model

The core of the algorithm is the model chosen to fit the data, and, therefore, to decompose the spectra.

A prevalent uni-modal Doppler spectrum measured with MIRA-36 in a cloud is shown in figure 4.2a. Moreover, often Doppler spectra are measured that show a bi-modality, which means double peaked power distributions, as shown in figures 4.2b, 4.2c, and 4.2d. The shaded area in every panel of figure 4.2 depicts the measured spectrum.

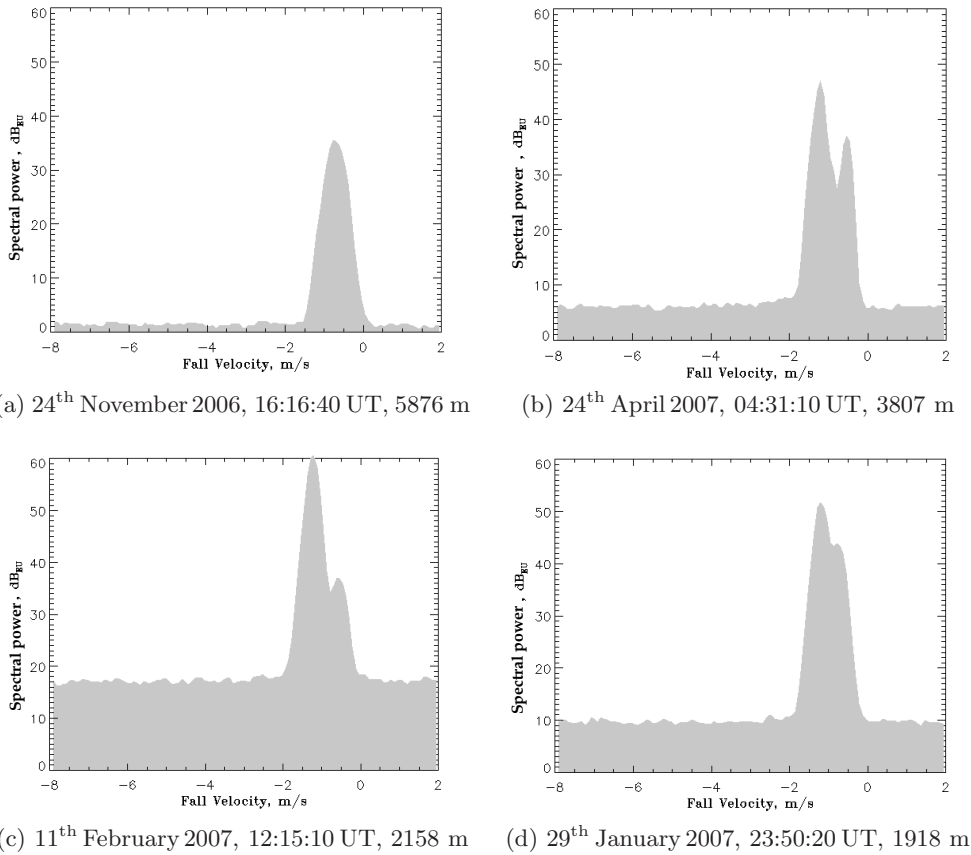


Figure 4.2: Examples of spectra measured by the radar system MIRA-36 (Hamburg, Germany). The measurements are represented with gray shaded areas. Negative velocities are downwards.

We consider bi-modal spectra indicative of the simultaneous presence in the radar resolution volume of at least two ensembles of cloud particles, each producing a Gaussian Doppler spectrum having slightly different parameters, which linearly superpose. A typical condition for the appearing of these particular bimodal spectra is the presence of a mixed-phase layer in a deep stratiform cloud. We should specify that also particles moving not uniformly in the radar resolution volume, as can hap-

pen to ice crystals because of turbulent motion on cooling cloud tops, could produce a double peaked spectrum.

We are aware that, because of the 10 seconds averaging time, secondary modes may appear due to the random scattering processes involved. Unfortunately, because of disk space limitations, it is not possible to save the raw data², thus it is not possible to verify if - and show that - secondary modes are present constantly in every spectrum averaged. The point is that, when revealed, secondary modes are present along a layer of some hundred metres and a time range of about half an hour. The observation of this persistence is not compatible with random processes, and let us believe that these secondary modes highlight a real physical structure.

We have already pointed out (see equation 3.20 and the following discussion at page 34) that one of the main characteristics of a radar system is the dependence of the received signal (i.e. the reflectivity) on the sixth power of the diameter of the observed particles. This means that radar systems are more sensible to bigger particles present in a resolution volume. Hence, when more ensembles of particles are present in a radar resolution volume, the signal produced by bigger particles, although with a low concentration, contributes normally the most to the backscattering cross section. In these circumstances only the strongest signal would be measurable. After eye inspection of samples of many spectra, taken from clouds showing different vertical and temporal extensions, it turned out that the decomposition of clouds Doppler spectra in no more than two modes is adequate in most cases.

Motivated by these observations, we developed a spectral model based on a mixture of two Gaussian functions, from which mode-specific moments of the Doppler spectrum are derived.

A Gaussian spectrum is represented by the equation:

$$S_G(v) = S_0 e^{-\frac{(v-v_0)^2}{2\sigma^2}} \quad , \quad (4.1)$$

where S_0 is the maximum power of the signal, v_0 is the mean velocity of the ensemble of particles, and σ is the spectrum width.

We already discussed (section 3.2 equation 3.17 and section 3.8) the presence in the signal registered by the radar system of a fluctuating additive noise N , which is due to the thermal noise P_N plus the phase noise $P_{N\Phi}$:

$$N = P_N + P_{N\Phi} \quad . \quad (4.2)$$

Then equation 4.1 becomes:

$$S_N(v) = N(v) + S_0 e^{-\frac{(v-v_0)^2}{2\sigma^2}} \quad , \quad (4.3)$$

where S_0 is referred to the noise-free floor level.

²At the DWD observation site in Lindenberg (Germany) spectra measured with a twin radar system MIRA-36 averaged for only 2 seconds are saved every week for 5 minutes (U. Goersdorf, personal communication)

If in a radar resolution volume there are more ensembles of particles, they produce a spectrum that is due to the linear superposition of the Gaussian signals which they would produce singularly. The additive noise is instead a result of the radar technology of measurement, thus it is added to the final noise-free signal. The equation representing this process is:

$$S(v) = N(v) + \sum_k S_{0k} e^{-\frac{(v-v_{0k})^2}{2\sigma_k^2}}, \quad (4.4)$$

with the index k representing the k -th component, or mode, of the total spectrum. As illustrated above, the spectral model used in this work is the linear superposition of only two Gaussian functions $S_1(v)$ and $S_2(v)$, plus the additive noise $N(v)$:

$$\begin{aligned} S(v) &= N(v) + S_1(v) + S_2(v) \\ &= N(v) + S_{01} e^{-\frac{(v-v_{01})^2}{2\sigma_1^2}} + S_{02} e^{-\frac{(v-v_{02})^2}{2\sigma_2^2}}, \end{aligned} \quad (4.5)$$

where $S_1(v)$ and $S_2(v)$ are the two Gaussian spectral components; S_{0k} , v_{0k} , and σ_k , with $k = 1$ and 2 , are the maximum signal power, the mean velocity, and the spectrum width of the k -th component, respectively.

Known the parameters of the k -th component of the spectrum, we are able to evaluate mode-specific moments of the spectrum and LDR_{dB} , by applying equations 3.58, 3.59, 3.60, and 3.44 to every component.

4.4 Noise level detection

Every measured spectrum is constituted by the meteorological signal and by a fluctuating additive noise, as shown in figure 4.3.

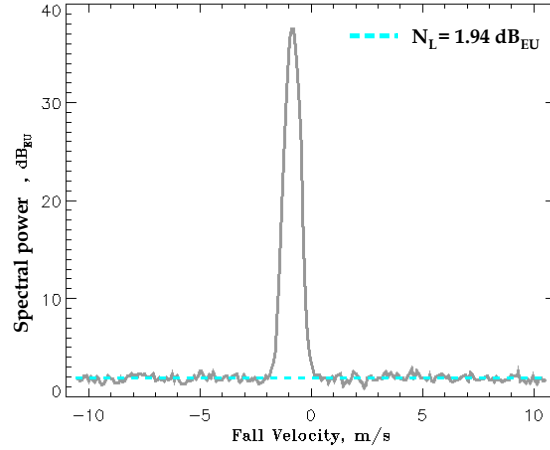


Figure 4.3: Example of an uni-modal spectrum measured by the radar system MIRA-36 (gray solid line). Negative velocities are downwards. The noise level N_L retrieved with the Hildebrand and Sekhon method (1974) is shown by the horizontal cyan dotted line. 07th December 2006, 15:02:40 UT, 6129 m, Hamburg, Germany

The noise is due to thermal noise and phase noise.

The thermal noise is always present, and depends on the electronic of the measuring system. Its mean value is fairly constant for every spectra, and is evaluated for all the spectra in one vertical profile by averaging the power values of the spectrum at the noise gate, that is a gate where no meteorological signal is present, as the spectrum shown in figure 4.4; usually the noise gate is one gate placed above 14 km (see also section 3.2 equation 3.17).

The phase noise is proportional to the power of the meteorological signal. Thereby its value varies from spectrum to spectrum (see also section 3.8).

In order to evaluate an unambiguous noise threshold for every spectrum, we adopt the method developed by Hildebrand and Sekhon (1974), which makes use of the power spectrum under investigation without any a priori knowledge about the electronic instrumentation. The only assumption made is that for radar systems the noise measured is a white Gaussian signal, that means that its power has a variance equal to the square of its mean value:

$$\sigma_{N(v)}^2 = \overline{N(v)}^2, \quad (4.6)$$

with $N(v)$ the measured noise spectral density (where all the sources of noise are considered). This equation is valid for non-averaged spectra.

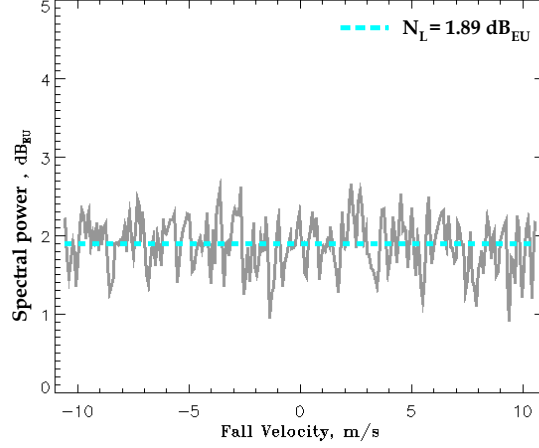


Figure 4.4: Example of a noise spectrum measured by the radar system MIRA-36 (gray solid line). Negative velocities are downwards. The noise level N_L retrieved with the Hildebrand and Sekhon method (1974) is shown by the horizontal cyan dotted line. 01st May 2007, 01:23:20 UT, 7725 m, Hamburg, Germany.

For averaged spectra this condition has to be modified as:

$$\sigma_{N(v)}^2 = \overline{N(v)}^2 / m \quad , \quad (4.7)$$

with $m \gg 1$ the number of averaged spectra

Let us consider one spectrum. The procedure consists in finding the noise threshold by subsequent approximations. First we calculate the mean value of the spectrum; the spectral points with a value greater than this mean value are cut away, and a new spectrum is formed. This process is iteratively performed reducing the threshold by recalculating for every step the new mean value of the spectrum, until it satisfies the property expressed in equation 4.7. The noise level value N_L is then equal to the last threshold applied. In the upper left panel on figure 4.5 it is shown a vertical profile for the noise level N_L retrieved for a sample of a deep convective cloud. By comparing it with the maximum signal power, shown on the upper right panel, you note that the noise level increases with the meteorological echo; as previously mentioned, this increasing is due to the phase noise, and it can be assumed that the thermal noise level is the one at very high range, where there is no meteorological signal.

Note that the values of the spectra here are given in Engineering Units EU (see section 3.9.1 for clarifications).

After applying the Hildebrand and Sekhon threshold method to retrieve the noise level, we remove it by subtracting N_L from the measured spectrum; we cut also some low peaks, which are due to the noise fluctuations, by smoothing to N_L the peaks with a maximum power lower than $N_L + \sigma_{N(v)}$.

After the removal of the noise the new function for the spectral model $S_m(v)$ (equation 4.5) is given by:

$$\begin{aligned} S_m(v) &= S_1(v) + S_2(v) \\ &= S_{01} e^{-\frac{(v-v_{01})^2}{2\sigma_1^2}} + S_{02} e^{-\frac{(v-v_{02})^2}{2\sigma_2^2}} . \end{aligned} \quad (4.8)$$

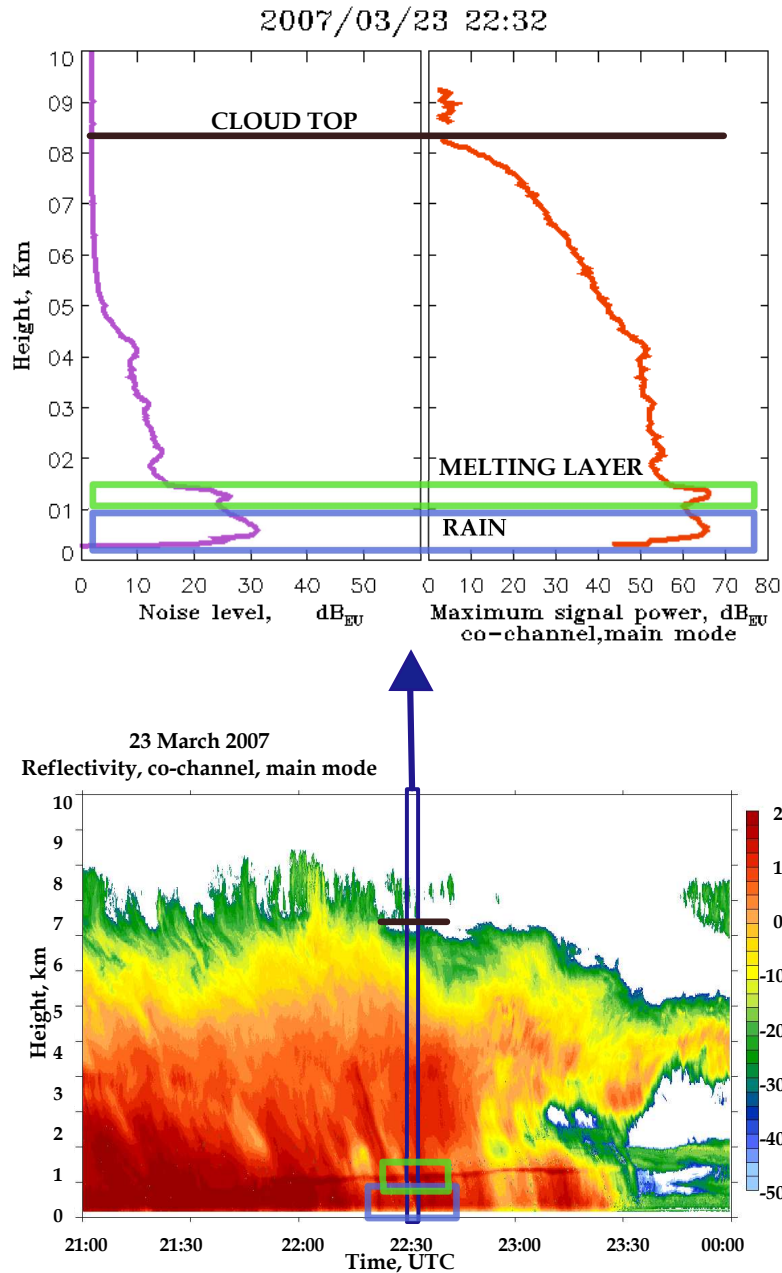


Figure 4.5: A noise profile sample taken at 22:32 UT from the measurements of a deep convective cloud (23th March 2007, Hamburg, Germany), whose reflectivity is shown on the lower panel. Upper left panel: profile of noise. Upper right panel: corresponding profile for the maximum signal power, co-channel, main mode after decomposition. Lower panel: reflectivity, co-channel, main mode after decomposition. Green rectangle: the melting layer, visible on the reflectivity measurements, shows a peak on both noise and maximum signal power at about 1.3 km. Black solid lines: cloud top. Blue rectangle: rainfall.

4.5 Fitting procedure

Before going into details, the decomposition algorithm is first illustrated in figure 4.6 for the cases presented in figure 4.2. In every panel the gray shaded area represents the measured spectrum; the cyan horizontal dashed line represents the noise level N_L retrieved by the Hildebrand and Sekhon method; the other dashed lines represent the components of the spectrum, specifically blue for the mode with the higher fall velocity and green for the mode with the slower fall velocity; the fuchsia solid line represents the reconstruction of the spectrum from its components. On the right side of every panel a legend indicates the values retrieved by the decomposition algorithm: with $i = 1, 2$ for the first or second mode respectively, $V_{Dmax,i}$ is the center of the

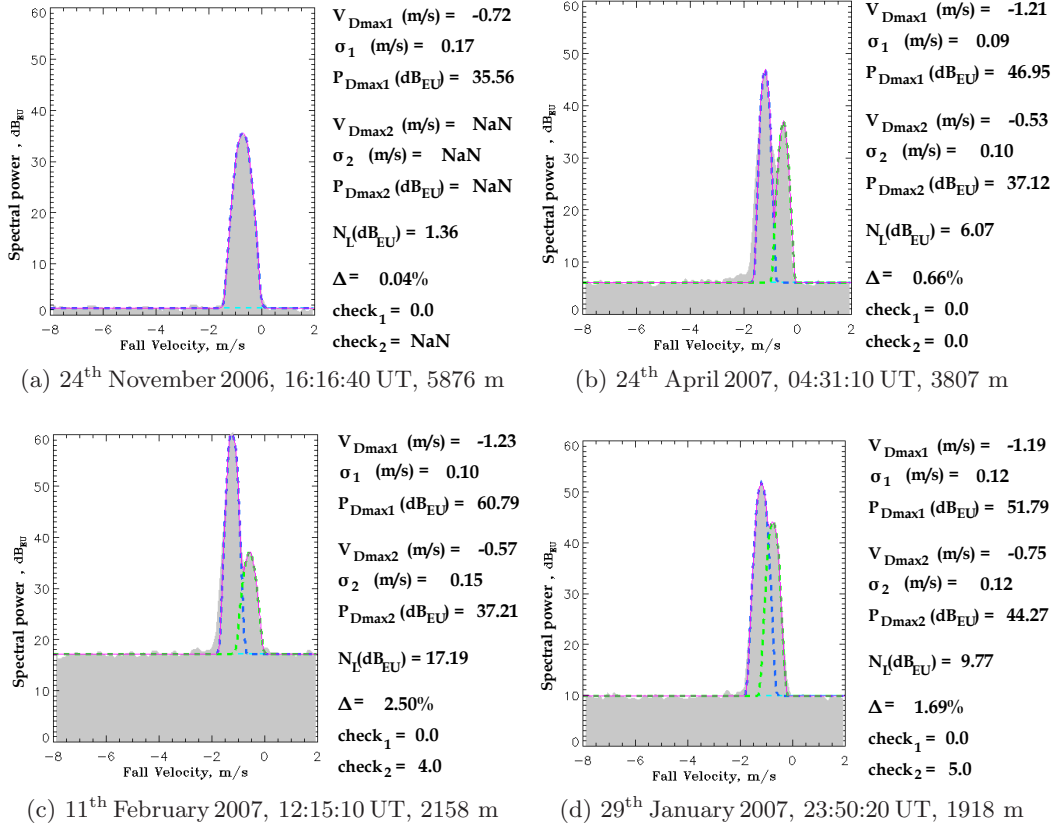


Figure 4.6: Examples of decomposed spectra. Gray shaded areas: measurements; cyan horizontal dashed line: noise level N_L retrieved by the Hildebrand and Sekhon method; blue and green dashed lines: components of the spectrum retrieved by the decomposition algorithm; fuchsia solid line: reconstruction of the spectrum from its components. Legend on the right side of every panel: values for the modes retrieved by the decomposition algorithm. Negative velocities are downwards. Measurements taken in Hamburg, Germany.

Gaussian curve ($v_{0,i}$ in equation 4.8), σ_i is the standard deviation, $P_{Dmax,i}$ is the maximum of the Gaussian curve ($S_{0,i}$ in equation 4.8), N_L is the noise level, Δ is the error of the fit evaluated as the average of the deviation between measures and fit expressed in percentage, and $check_1$ and $check_2$ are two indices whose meaning is described in table 4.1.

The decomposition algorithm works as following.

Once the spectral model is defined as illustrated in the previous section, the task of the algorithm is to fit the measured spectrum and to return the parameters of the model, namely the triplets (S_{01}, v_{01}, σ_1) and (S_{02}, v_{02}, σ_2) being composed by the maximum signal power, the mean velocity, and the spectrum width of the two Gaussian components (see also figure 3.8). The routine chosen for the fit is an IDL custom routine, which makes use of a gradient–expansion algorithm to compute a non–linear least squares fit. The performance of the fit is represented by the parameter χ^2 (chi square). Its value ranges from 0 to 1; a large value indicates that the model represents reasonably the measured data. Iterations are performed until the χ^2 changes by a specified amount, or until a maximum number of iterations have been performed. The automatic fitting procedure needs an initial guess for the parameters of the spectral model. These are relative maxima, the corresponding values for the Doppler velocities, and the width of the components of the spectrum. We search for the two higher relative maxima in every spectrum, and the corresponding values for the Doppler velocities, by using a dedicated routine, whereas for the width

The retrieved values for every decomposed spectra are saved all together in an IDL vector that is composed of the following elements:

- 0 – $V_{Dmax,1}$: center of the main mode–specific Gaussian curve;
- 1 – $FWHM_1$: Full Width at Half Maximum of the main mode–specific Gaussian curve;
- 2 – $P_{Dmax,1}$: maximum of the main mode–specific Gaussian curve;
- 3 – ε_{V_1} : computational error for $V_{Dmax,1}$;
- 4 – ε_{FWHM_1} : computational error for $FWHM_1$;
- 5 – ε_{P_1} : computational error for $P_{Dmax,1}$;
- 6 – $V_{Dmax,2}$: center of the secondary mode–specific Gaussian curve;
- 7 – $FWHM_2$: Full Width at Half Maximum of the secondary mode–specific Gaussian curve;
- 8 – $P_{Dmax,2}$: maximum of the secondary mode–specific Gaussian curve;
- 9 – ε_{V_2} : computational error for $V_{Dmax,2}$;
- 10 – ε_{FWHM_2} : computational error for $FWHM_2$;
- 11 – ε_{P_2} : computational error for $P_{Dmax,2}$;
- 12 – N_L : noise level;
- 13 – σ_N : noise variance;
- 14 – $check_1$ and 15 – $check_2$: indices whose meaning is described in table 4.1;
- 16 – Δ : error of the fit evaluated as the average of the deviation between measures and fit expressed in percentage.

of the components of the spectrum we choose a fixed starting value, namely 0.3 m/s.

Values for the model parameters with no physical meaning could occur as result of the automatized fitting procedure, as shown in figure 4.7. Such unsuitable results need to be excluded.

We come out with the following list of possible non-plausible modes:

- a mode with a negative value for the maximum signal power (figure 4.7a);
- a mode with mean velocity value out of the possible range (figure 4.7b), which is:
[-10.5 m/s, +10.5 m/s];

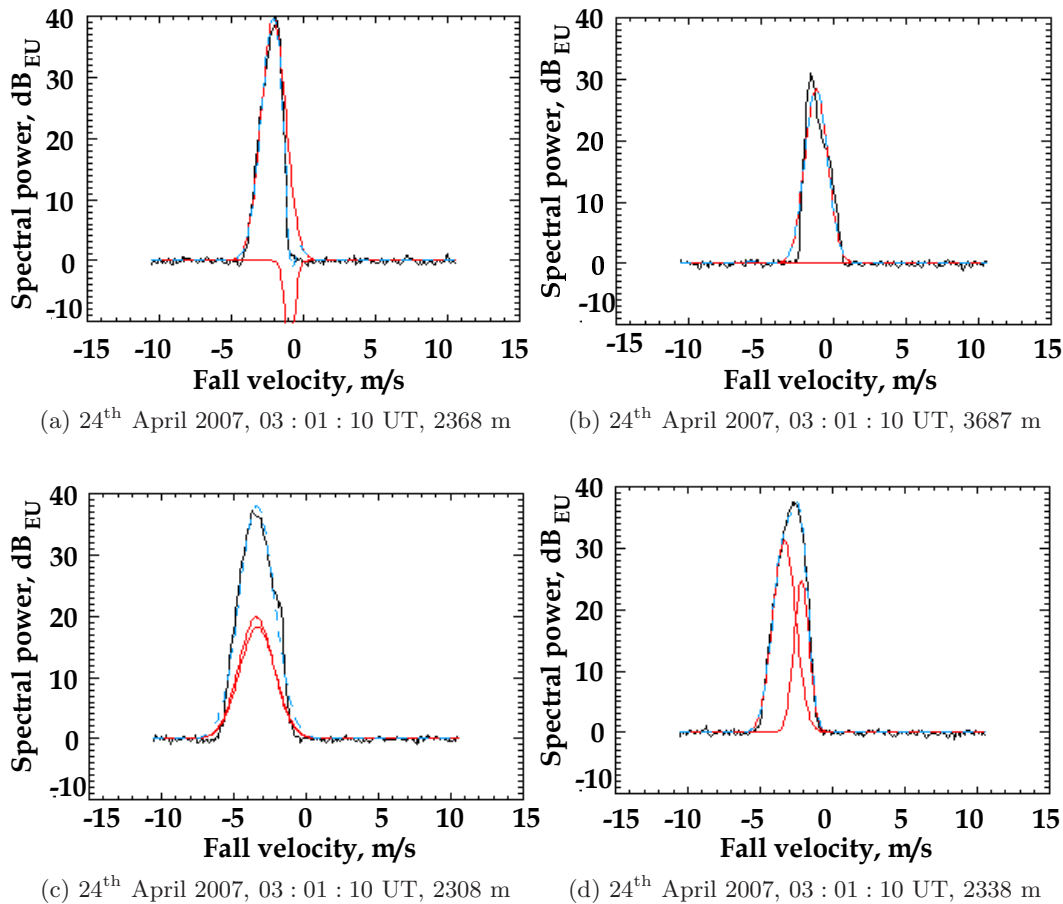


Figure 4.7: Example of non-plausible modes. Black solid line: measurements; red solid lines: the two Gaussian components of the spectrum before the non-plausible mode analysis; blue dashed line: linear superposition of the Gaussian components (see equation 4.8). (a): a negative value for the maximum signal power; (b): a mean velocity value out of the possible range; (c): a mode lying underneath the other; (d): modes too close to each other. Negative velocities are downwards.

- a mode where the spectral width is oversized; we choose as reasonable a value lower than a third of the total velocity range spread:
 $1/3 \cdot 21 \text{ m/s} \cong 7 \text{ m/s}$;
- a mode lying underneath one other mode in the same spectrum (figure 4.7c).

If one relative maximum is detected, and the mode found is rejected because non-plausible, then the relative spectrum is considered containing no meteorological signal.

If two relative maxima are detected, but one of the mode retrieved is non-plausible, the fitting is repeated by forcing a one-mode fitting.

We note that the detection of a non-plausible modes for two relative maxima could happen also if the two modes have both a physical meaning, but in consequence of a too large difference in energy values between the two relative maxima, the lower mode is automatically discarded, as for example it happens for the two peaks shown in figure 4.8. Thus, when the difference between the two maxima is greater than 32 dB, a one-mode fitting is forced on the lower peak, after the higher is momentarily removed from the spectrum.

Ultimately it is checked if the two modes are too close to each other (figure 4.7d). A separability criterion between Gaussian curves is then applied: when the absolute value of the difference between the mean velocity values is smaller than the averaged

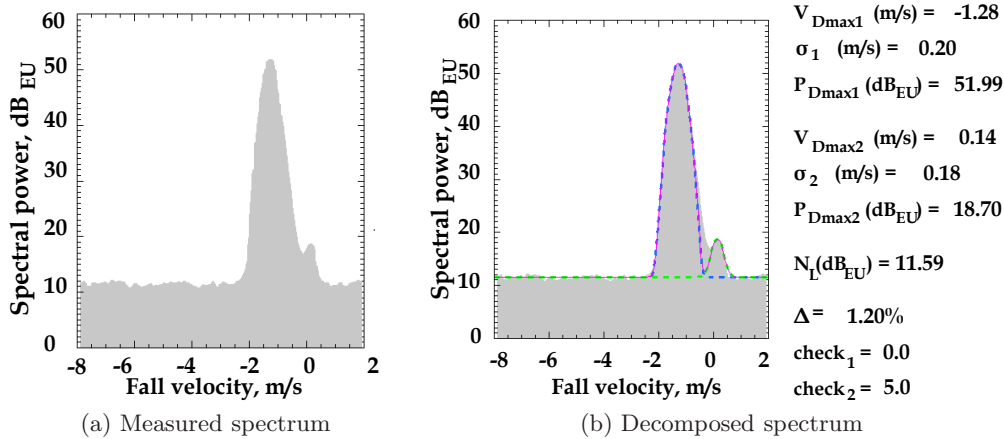


Figure 4.8: Example of a non-plausible mode resulting from the automatized fitting procedure. Here is shown a spectrum with a large difference in energy values between the two relative maxima. Gray shaded areas: measurements; cyan horizontal dashed line: noise level N_L retrieved by the Hildebrand and Sekhon method; blue and green dashed lines: components of the spectrum retrieved by the decomposition algorithm; fuchsia solid line: reconstruction of the spectrum from its components. Legend on the right side of every panel: values for the modes retrieved by the decomposition algorithm. Negative velocities are downwards. 22nd March 2007, 19:24:20 UT, 3027 m.

standard deviations of the two modes, then the modes are considered not separable, and one-mode fitting is again forced.

To control which path the algorithm followed to get the final components of every spectrum, like whether one or two modes were detected and whether one of these were rejected and why, we create a two values index, illustrated in table 4.1. The first

Table 4.1: What can go wrong during the automatized fitting procedure: meaning of the indices $check_1$ and $check_2$ and final result of the decomposition algorithm.

| Case | CHECK ₁ | CHECK ₂ | Meaning | Result of the decomposition |
|----------|--------------------|--------------------|------------------------------------------------------------------------------------------------------------------------------------------------------------------------------------------------------------------------------|-------------------------------------------------------------------------------------------------------|
| a | NaN ^a | NaN | no relative maxima found | no mode |
| b | 0 | NaN | 1 maximum | 1 mode |
| | 1 | NaN | 1 maximum but mode with negative maximum signal power | no mode |
| c | 2 | NaN | 1 maximum but mode with mean velocity value out of the possible range | |
| | 3 | NaN | 1 maximum but mode with too wide spectral width | |
| d | 0 | 0 | 2 maxima | 2 modes |
| | 1/0 | 0/1 | 2 maxima but 1 th /2 nd mode with negative maximum signal power | one-mode fitting forced |
| e | 2/0 | 0/2 | 2 maxima but 1 th /2 nd mode with mean velocity value out of the possible range | |
| | 3/0 | 0/3 | 2 maxima but 1 th /2 nd mode with too wide spectral width | |
| f | 0 | 4/5/6 | one-mode fitting was forced (case <i>e</i>); if too large difference in energy values between the two relative maxima \implies remove temporarily the retrieved mode and force one-mode fitting on the remaining spectrum | 1 mode (first mode retrieved and case <i>c</i>) or 2 modes (first mode retrieved and case <i>b</i>) |
| g | 0 | 7.1/7.2 | 2 modes but maximum value of the 1 th /2 nd mode lies below the 2 th /1 nd mode curve | one-mode fitting forced |
| h | 0 | 8 | 2 modes but not separable | one-mode fitting forced |

^aNot a Number: IDL custom value to represent missing values in computations

(second) value refers to the main (secondary) mode retrieval, and the combination of them tell us which non-plausible mode checks, if any, the algorithm went through, as it is annotated in the table. This list has helped us in developing and refining the algorithm.

As different modes correspond to different ensembles of particles, we also attempt to cluster the data, by using the measured values of fall velocity and LDR_{dB} , and the vertical structure of the modes as additional information. At the present state of the art the results of this clustering routine are not stable enough to run it automatically. Thus we decide, for the time being, to cluster the modes by sorting them with the fall velocity. Nevertheless, a suitable clustering routine, along with a classification algorithm, would be valuable for a proper evaluation of liquid and ice water content. By observing the results of the decomposition algorithm we note that usually the mode with lower power has fall velocity slower than the mode with higher power (note that negative velocities are downwards, therefore a particle with the lower value of fall velocity is actually falling faster to the ground). This means that, for every spectrum, if only one mode is detected, it is assigned to a main mode; if two modes are detected, to the main mode it is assigned the one falling faster (lower fall velocity).

The decomposition algorithm is applied to both the co- and the cross-channel. In order to verify whether the corresponding mode-specific fall velocities are the same in the co- and cross-polarised channels, v_{co} and v_{cx} respectively, we consider the scatterplot of v_{cx} vs. v_{co} , in which the cloud of points should be distributed along the diagonal. The examples shown in figure 4.9 sustain that the decomposition algorithm is able to properly recognize different ensemble of cloud particles.

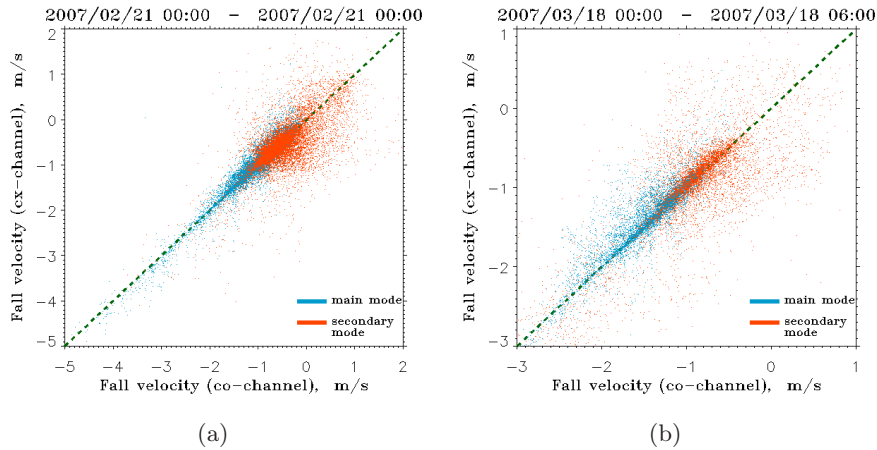


Figure 4.9: Scatterplots v_{cx} vs. v_{co} for two cases of (a) 24 and (b) 6 hours. The mode-specific fall velocities are distributed along the diagonal, thus the decomposition algorithm assigns the same fall velocity to the modes retrieved in the two channels. Negative velocities are downwards.

4.6 Calibration

We have seen in section 3.9.1 that, in order to properly calculate the spectral reflectivity z_i (see equation 3.72) from the spectral powers $p_{raw,i}$ returned by the radar data acquisition software, we need to know the Hildebrand and Sekhon spectral noise level $n_{HS,raw}$, the weather radar constant C , and the spectral total noise $n_{T,raw}$ at the noise range gate. The radar software performs this operation automatically, with instantaneous recorded values of the spectral total noise. Due to the limited space in the disk for data, only spectral powers and global moments evaluated from them are saved. Thus the problem of correctly calibrating the mode-specific moments insistently arises.

The Hildebrand and Sekhon noise level is found for every spectrum by using the routine explained in section 4.4.

An estimate for the spectral total noise $n_{T,raw}$ at the noise range gate can be obtained by averaging the values of the Hildebrand and Sekhon spectral noise level $n_{HS,raw}$ on the range gates along the last kilometer away from the radar.

Let us consider a spectrum decomposed in its two components, as function of the velocity range; from equations 3.38 and 3.39, we are allowed to substitute the summation over the spectral bins with summation over the Doppler velocity:

$$\begin{aligned} P_{1,raw} &= \sum_v p_{1,raw,v} \quad , \\ P_{2,raw} &= \sum_v p_{2,raw,v} \quad , \end{aligned} \quad (4.9)$$

so that the total power is directly proportional to their sum:

$$P_{raw} = c (P_{1,raw} + P_{2,raw}) \quad , \quad (4.10)$$

with c a constant of proportionality, needed because the mode-specific spectral power could overlap for some bins of the spectrum.

By expanding equation 3.67 we can write:

$$\text{snr}_v = c \frac{p_{1,raw,v} - n_{HS,raw}}{n_{T,raw}} + \frac{p_{2,raw,v} - n_{HS,raw}}{n_{T,raw}} = c (\text{snr}_{1,v} + \text{snr}_{2,v}) \quad . \quad (4.11)$$

As the spectral reflectivity factor is given by equation 3.71 :

$$z_v = C r^2 \text{snr}_v \quad , \quad (4.12)$$

we can write:

$$\frac{z_v}{C r^2} = c (\text{snr}_{1,v} + \text{snr}_{2,v}) \quad , \quad (4.13)$$

and then evaluate the calibration constant C_{cal} as:

$$C_{cal} = c \cdot C r^2 = \frac{z_v}{\text{snr}_{1,v} + \text{snr}_{2,v}} \quad , \quad (4.14)$$

so that, summing over the spectrum:

$$Z = C_{\text{cal}} (\text{SNR}_1 + \text{SNR}_2) \quad , \quad (4.15)$$

with the mode-specific calibrate reflectivities:

$$\begin{aligned} \text{SNR}_{1,\text{cal}} &= C_{\text{cal}} \text{SNR}_1 \\ \text{SNR}_{2,\text{cal}} &= C_{\text{cal}} \text{SNR}_2 \quad . \end{aligned} \quad (4.16)$$

The result of the decomposition algorithm returns the coefficient of the two Gaussian components of the spectrum; thus the summation over the spectrum of the individual $\text{snr}_{k,v}$ yields to:

$$\begin{aligned} \text{SNR}_k &= \sum_v \frac{p_{k,\text{raw},v} - n_{\text{HS},\text{raw}}}{n_{T,\text{raw}}} \\ &= \frac{A_{G,k}}{n_{T,\text{raw}} \cdot \Delta(v)} \quad , \end{aligned} \quad (4.17)$$

with $k = 1, 2$ the component of the spectrum, $A_{G,k}$ the area subtended by the k -th Gaussian curve, and $n_{T,\text{raw}}$ being constant along the spectrum. From integration theory it follows that:

$$A_{G,k} = S_{0,k} \sigma_k \sqrt{2\pi} \quad , \quad (4.18)$$

with $S_{0,k}$ and σ_k respectively the maximum signal power and the spectrum width of the k -th component of the spectrum.

Chapter 5

Microphysical retrievals

Dissertation:
every word a drop of blood.

5.1 Introduction

The decomposition of the spectral modes of the Doppler spectra and the evaluation of the mode-specific moments (previous chapter) allows us to retrieve several microphysical properties of the cloud system under study.

Among the available data collected in Hamburg (Germany) by the radar system MIRA-36 between July 2006 and May 2007, we choose to analyse the data collected between November 2006 and May 2007. This narrowed data set presents in fact a constant technical configuration, namely the one illustrated in section 3.11 (during 2006 the system was still tested), which meets requirements of needful accurate measurements and of disk space disposal.

Moreover, we restrict our interest to non convective events, as for convective events it is not possible to separate the contribution of the vertical air motion from the motion of the hydrometeors (see section 5.3).

In this data set, embracing nevertheless different cloud structures, we find that bimodal spectral structures prevail for most cloud types, although Linear Depolarisation Ratio (LDR) is evaluable for both the modes only in case of deep stratiform convective clouds.

We want to emphasize that the aim of this work is not to resort to statistics, rather to develop and test the new algorithm.

Statistical analysis can be realized within the several measuring campaigns the radar system MIRA-36 was involved in, including TOSCA¹ (Kneifel et al., 2010), COPS² (Wulfmeyer et al., 2008), and, currently, the Barbados campaign³.

¹<http://gop.meteo.uni-koeln.de/tosca/doku.php>

²<http://www.uni-hohenheim.de/spp-iop/index.htm>

³<http://barbadossite.wordpress.com/>

Therefore in the following we propose an analysis of stratiform mixed-phase cloud systems.

After having individuated a mixed-phase system by means of the presence of a layer of double modes stable in time (section 5.2), we proceed with reducing the influence of the vertical air motion by using an averaging approach. As we will see in section 5.3, the limit of this approach is that it is applicable only to non-convective stratiform clouds.

Known the fall velocity of cloud particles, we derive their size and subsequently the cloud water content. As explained in section 3.3 at page 37, it is not possible to evaluate the Liquid Water Content (LWC) with the single use of one radar system. Thus, we evaluate mode-specific microphysical characteristics of the ice cloud particles only, such as characteristic diameter and Ice Water Content (IWC). The methods used for these retrievals are described in section 5.4.

Further pieces of information on the properties of the cloud particles are extracted by linearly fitting the main mode-specific velocity as a function of altitude. The gradient of this fit gives a picture on the growing behavior of the particles along the vertical. Specifically, we have observed a continual constant increasing of the Doppler velocity on the cloud particles fall path, as we describe in section 5.5.

5.2 Mixed-phase recognition

An example of decomposed and clustered spectra profile is shown in figure 5.1, where retrieved mode-specific parameters for the model, (i.e. mean velocity, maximum signal power, and spectrum width), equivalent reflectivity, and LDR are depicted in blue for the main mode and in green for the secondary mode.

The main features of the algorithm are drawn in this figure.

The melting layer is recognizable at about 1.5 km by the abrupt jump observed in the fall velocity; below this level, in the rain band, the results of the algorithm are unrealistic, as echoes from raindrops do not have a Gaussian power density distribution, which is instead the rationale for the application of our decomposition method (equation 4.5).

Two modes are observed along 500 m above the melting layer in both the polarimetric channels. The values of the LDR for these two modes are significantly mode-dependent: about -25 dB for the main mode and between -15 and -10 dB for the secondary mode. Let us recall that for spherical cloud particles, as cloud- or drizzle- drops, LDR tends to the lowest limit of -35 dB. Any deviations of LDR from this value indicates presence of non-spherical cloud particles. Well separated values of LDR imply hydrometeors with different shapes, supporting the claim that a mixed-phase layer was observed near the cloud base in the considered event. Two modes are also visible in the co-channel at about 8.5 km; however, as in this case the bimodal spectra cannot be explained by a realistic particle distribution, we assume here that they reflect enhanced turbulent motion of cloud particles induced by radiative cloud top cooling.

Putting the double modes generated by turbulence aside, the typical condition for observing bimodal spectra remains the presence of a mixed-phase layer.

Looking at the fall velocity and LDR values only, it is not possible to say, apart from the secondary mode moving slower to the ground, if the modes are due to solid or liquid water particles. Because of the presence of the melting layer, it is reasonable to assume that the main mode is due to ice crystals, growing to snow and then melting to form rain.

Zawadzki et al. (2001) have suggested a qualitative method to assign a phase to the two modes, when melting layer is observed. Let us firstly underline that the presence of a secondary mode is an evidence for the concurrent presence of snow, supercooled liquid droplets and ice crystals, the latter produced by secondary nucleation, process illustrated in section 2.4.1 (Hallett and Mossop, 1974). The signature of droplets and pristine ice crystals to a cloud radar is very similar, so we cannot distinguish among them looking at cloud radar measurements only. Nevertheless, we can claim that the secondary mode retrieved is due to the class of particles with major concentration, that produces an echo that superposes over the other.

Let us now focus on the secondary mode vanishing in the melting layer. The disappearance of the secondary mode in the melting layer is a clear indication of particles melting, and thus we infer that the secondary mode is due to the higher concentration of ice crystals; if instead the secondary mode appears just to grow in fall

velocity through the melting layer, this is the indication of the increasing of mass of the particles due to coalescence and of their transformation in rain drops, thus we infer that the secondary mode is due to the higher concentration of droplets.

In the example here reported the first hypothesis seems to be more reliable.

As we notice in our discussion on the spectral model (section 4.3), secondary modes may appear due to the random scattering processes occurring during the 10 seconds averaging time. Figure 5.2 shows that the secondary modes of figure 5.1 are present for an appreciable time range. The observation of this persistence is not compatible with random processes, therefore it seems very plausible that these secondary modes highlight a real physical structure.

In contrast the signature produced by the turbulence, shown in figure 5.3, exhibits double modes which appear and disappear from one time step to the other.

Note that in figure 5.2 the profiles are one minute apart, whereas in 5.3 the profiles are consecutive, i.e. ten seconds apart.

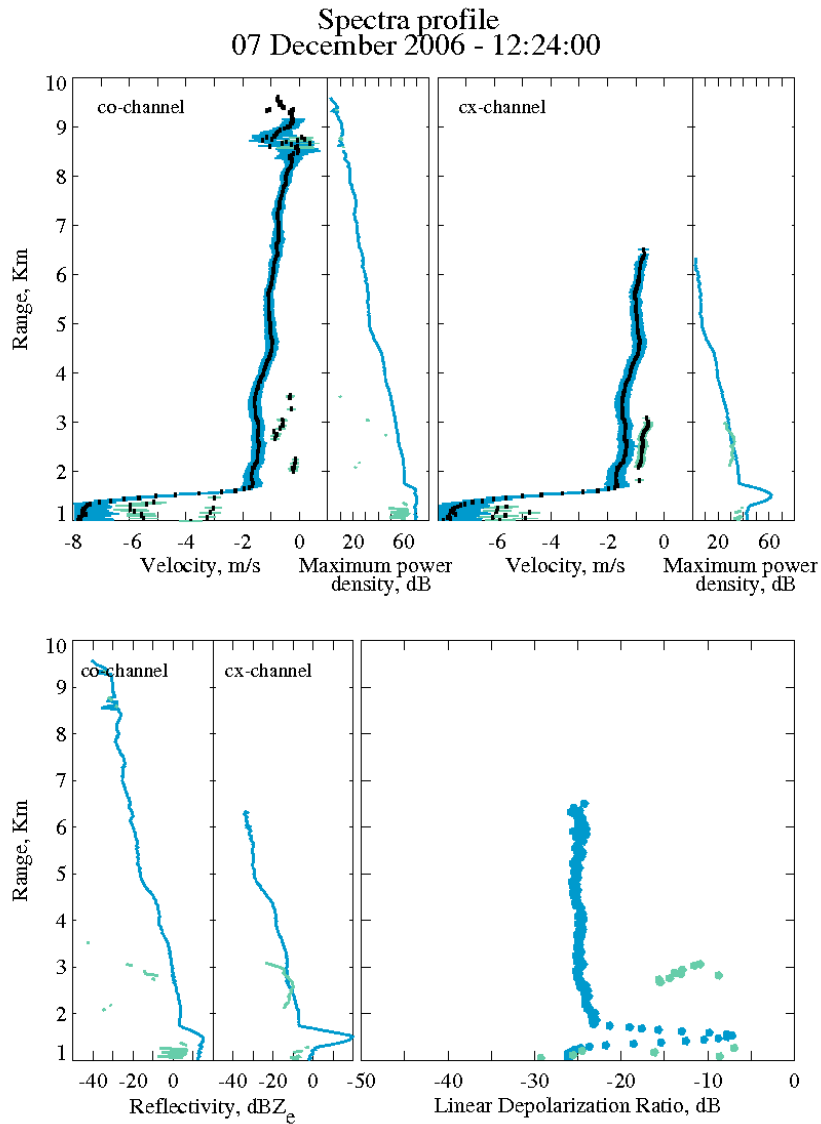


Figure 5.1: Example of mode-specific model parameters (mean velocity, maximum signal power, and spectrum width), equivalent reflectivity, and LDR profiles resulting from the decomposition. The colors indicate the mode order number: blue for the main mode, green for the secondary mode. Upper panels: mean fall velocity (black thick), spectrum width (colored horizontal bars), and maximum signal power in the co-channel (left panel) and in the cx-channel (right panel). Lower panels: equivalent reflectivity factor in the co- and in the cx-channel (left panels) and LDR (right panel). Negative velocities are downwards.

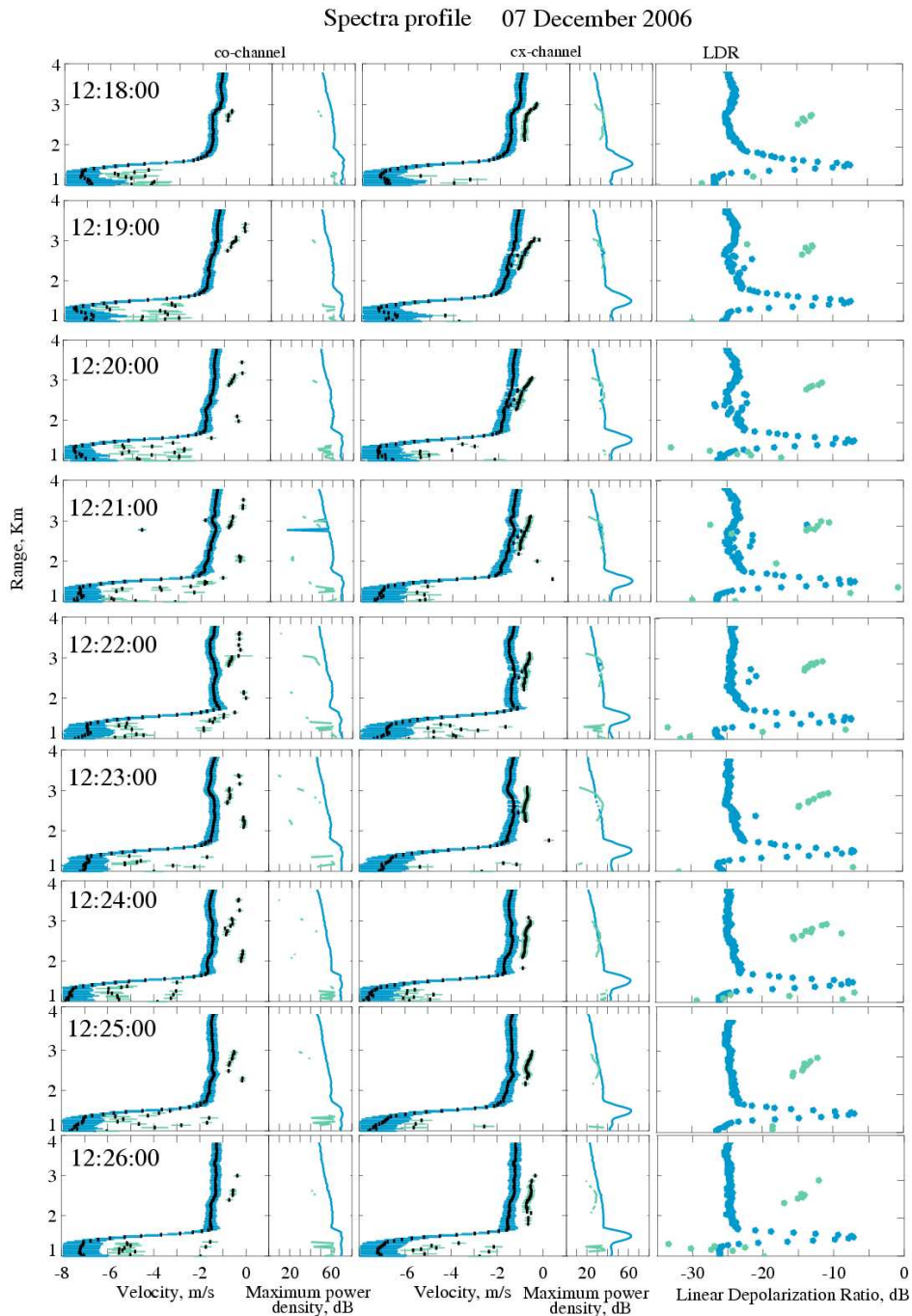


Figure 5.2: Time series of mode-specific (main mode in blue and secondary mode in green) model parameters and LDR profiles resulting from the decomposition. The presence of secondary modes on a height layer, during a continuous period of time, and with stationary values of velocity and LDR, is plausibly due to a mixed-phase layer. Mean fall velocity (black thick), spectrum width (colored horizontal bars), and maximum signal power in the co-channel (left panels) and in the cx-channel (central panels). Right panels: LDR. Time is indicated on every line of panels. Negative velocities are downwards.

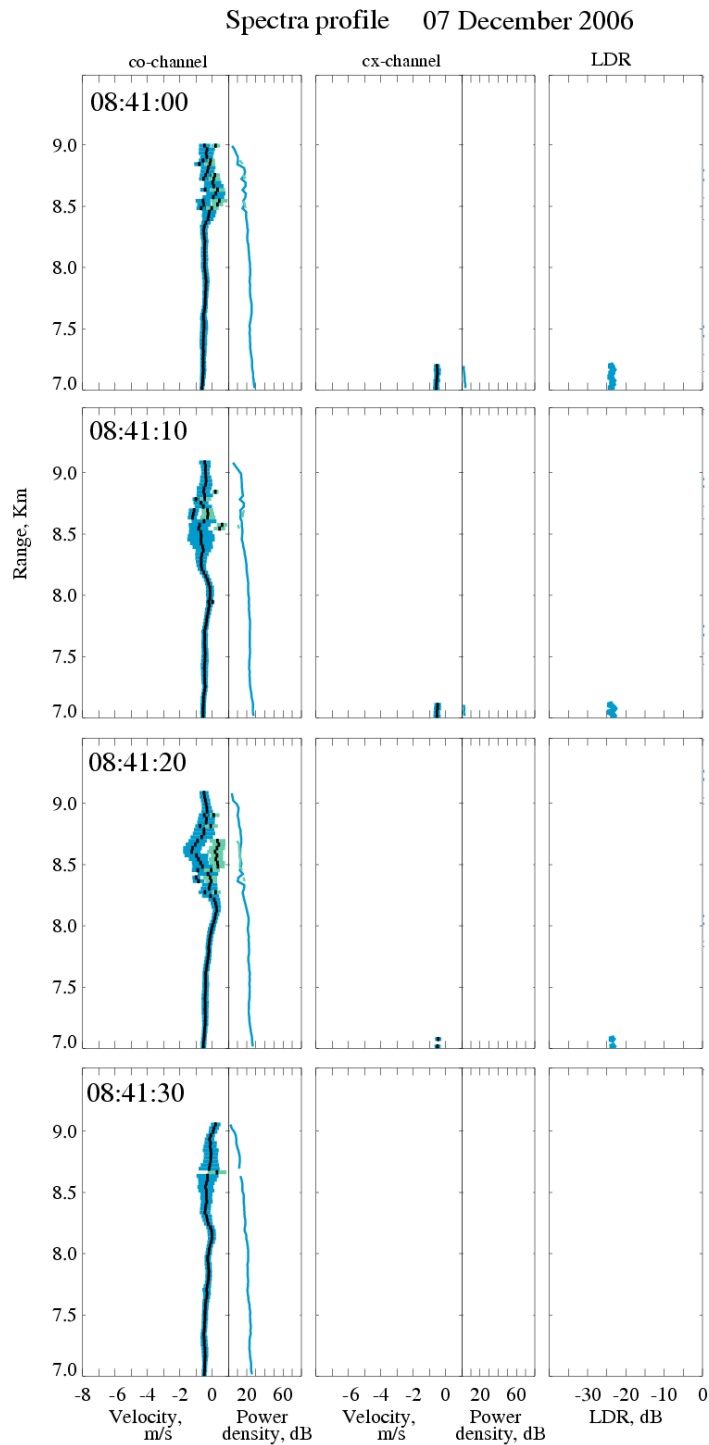


Figure 5.3: Time series of mode-specific (main mode in blue and secondary mode in green) model parameters and LDR profiles resulting from the decomposition. The presence of random secondary modes is plausibly due to turbulence. Mean fall velocity (black thick), spectrum width (colored horizontal bars), and maximum signal power in the co-channel (left panels) and in the cx-channel (central panels). Right panels: LDR. Time is indicated on every line of panels. Negative velocities are downwards.

5.3 Vertical velocity of cloud particles assessed by Doppler radar measurements

In order to calculate microphysical properties of clouds by measurements taken with a vertically pointing Doppler radar system, we need to determine the ice particle characteristic size from the measured Doppler velocities.

The vertical Doppler velocity measured by vertically pointing radar systems V_D is due to two terms: the terminal vertical velocity of the particles, and the vertical motion of the air that they also experience. In symbols:

$$V_D = V_t + V_a \quad , \quad (5.1)$$

with V_t the actual terminal velocity of the cloud particles and V_a the vertical air motion.

Considering the bias which is introduced by vertical air motion is then fundamental, as we want to connect unambiguously the fall velocity of cloud particles to their size. The contribution of air motion for small cloud particles could be indeed of the same magnitude or even larger as the particles terminal velocity, that is about 1 m/s. Before using the values of the Doppler velocity to retrieve the dimension of the particles, one should estimate the value of V_a , for example using a windprofiler (i.e. a VHF Doppler radar system) as has been described by Wakasugi et al. (1986), or reduce its influence, so that the measured Doppler velocity can be considered a good approximation for the terminal velocity of the ensemble of particles as $V_D \approx V_t$.

In the case of our measurements, we rely on a single cloud radar system, therefore in the following we will illustrate a technique apt to reduce the contribution of the air vertical motions on the total measured Doppler velocity, which does not require further instrumentation. This method has been suggested by Orr and Kropfli (1999) and has been successfully applied in a simplified variant by Matrosov et al. (2002), and by Delanoë et al. (2007). The rationale of Orr and Kropfli approach is that the vertical air motions are supposed to randomly fluctuate, therefore, after performing a time average of the Doppler velocity measurements, one expects them to have a 0 m/s average.

If there was no influence from air motions, and assuming that different populations of particles do not effect to a great extent the scattering, the measurements should lay on the solid curve:

$$V_D = \alpha Z_e^\beta \quad , \quad (5.2)$$

where α and β are retrieved by a least square fit on the cloud of points. The distance of every measured point from the regression line in the scatter plot of V_D against Z_e indicates the presence, and the intensity, of vertical air motions in the case under study.

In order to retrieve information on the cloud structure, Orr and Kropfli have suggested to group the data in small cloud height bins and cloud reflectivity bins, and then to perform the time average. As it is supposed that the structure of a stratiform cloud varies with the height, but stays fundamentally stable within a cloud

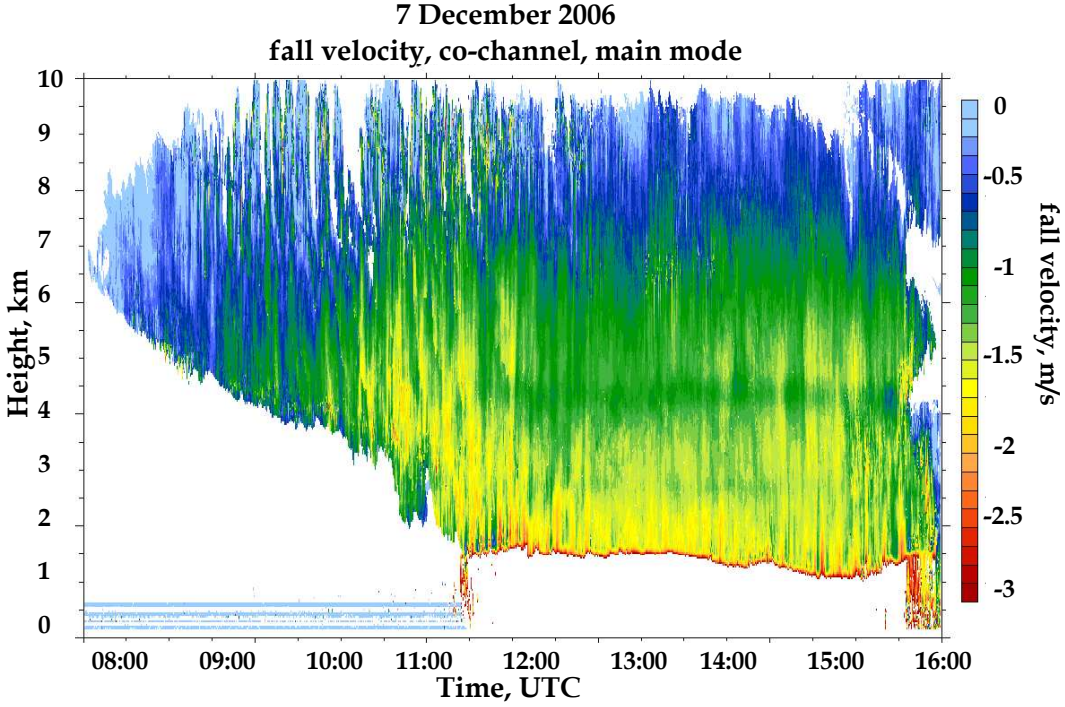


Figure 5.4: Fall velocity measured the 7th December 2006, from 07:30 to 16:00 UTC, Hamburg, Germany. Negative velocities are downwards. Velocity values of rain, below about 1.5 km are out of the shown range.

layer, the time averaging can be performed on thin cloud layers. Furthermore, time averaging intervals need to be long enough to reduce the air motion variability, but at the same time short enough to not avoid possible changes in the cloud structure. For the i -th height layer we can then write the 5.2 as:

$$\langle V_D \rangle_{i,j} = \alpha_i \langle Z_e \rangle_{i,j}^{\beta_i} \quad , \quad (5.3)$$

with $\langle V_D \rangle_{i,j}$ and $\langle Z_e \rangle_{i,j}$ the time averages of V_D and Z_e in the i -th height bin and in j -th reflectivity bin, and with α_i and β_i obtained by a least square fit on the partitioned data. Once that the coefficient of the power law relationship 5.3 are retrieved, the punctual fall velocity V_t' corrected for the air motions can be calculated by using the measured values of the reflectivity factor for every height layer:

$$V_t' = \alpha_i Z_e^{\beta_i} \quad . \quad (5.4)$$

One should note that the residuals of the vertical air motions may be large compared to V_t only if strong up- or down-drafts are present. As a consequence, this approach can be successfully applied to clouds with a stable stratiform structure, but not to convective events. Indeed, best-fit curves which have similar coefficients and

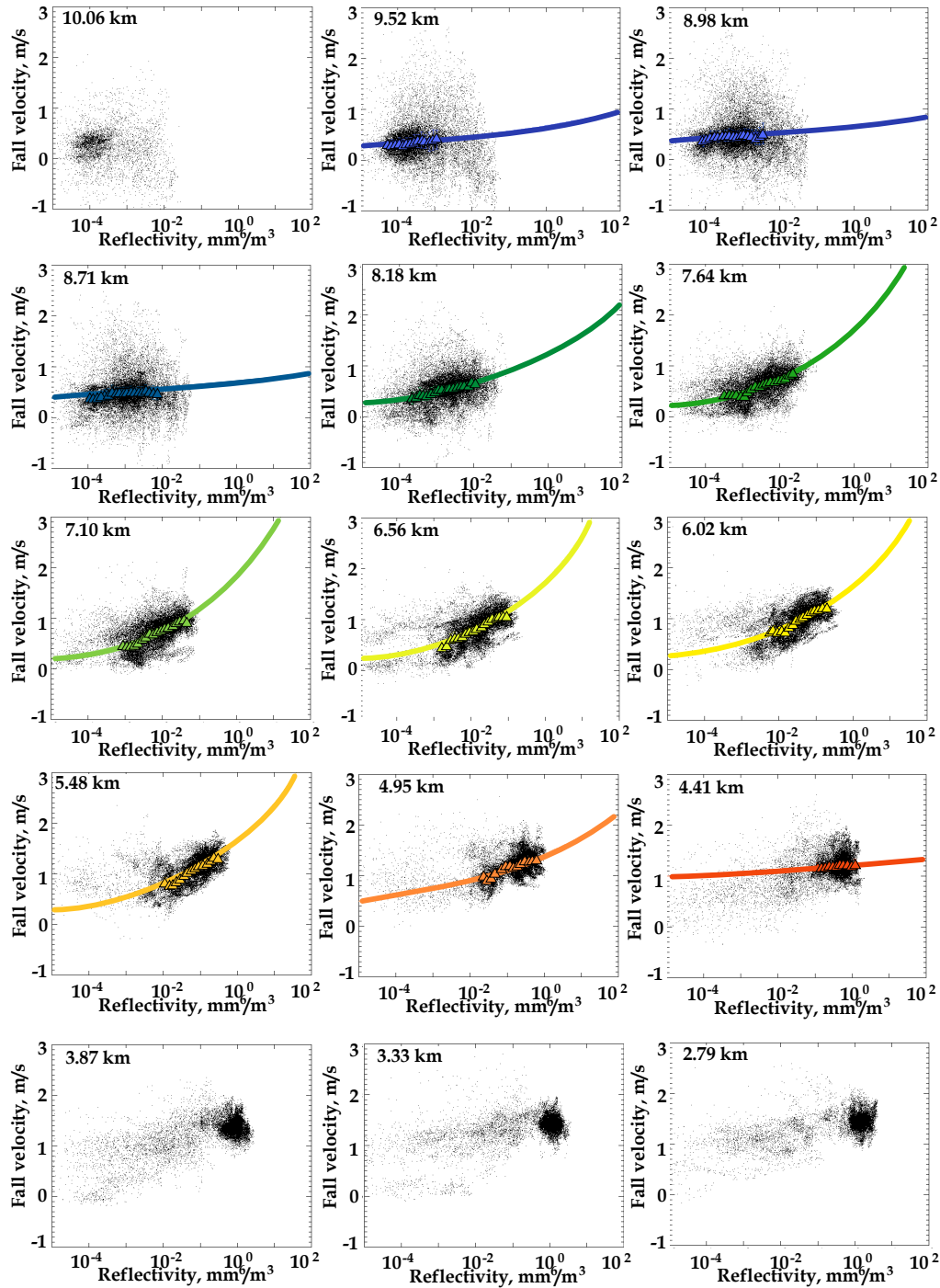


Figure 5.5: Scatterplots of V_D against Z_e , for the reflectivity measured the 7th December 2006, Hamburg, Germany. Every panel corresponds to a cloud layer of 270 m centered at the indicated quote. The measurements are represented by the cloud of points. The time averages for reflectivity bins of 1 dB are calculated only for groups of data with more than 500 points, and are represented by colored triangles. The best-fit curves with the equation 5.2 are also shown. The particle terminal velocities are plotted as positive values to be consistent with the power-law analysis.

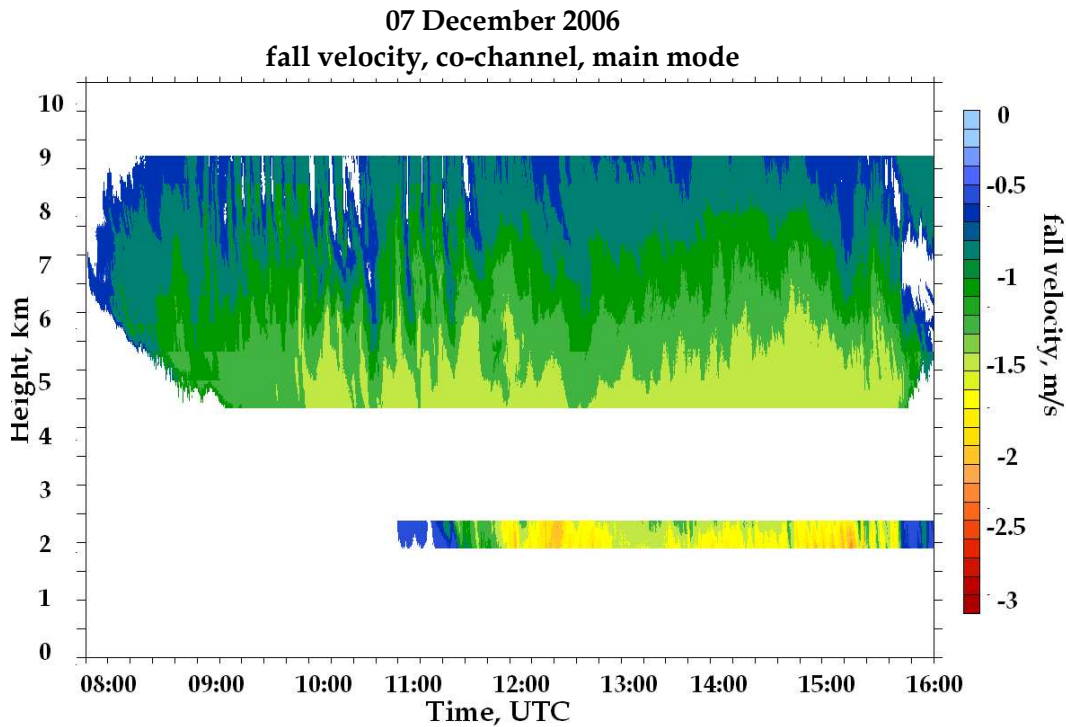


Figure 5.6: Fall velocity, co-channel, main mode, 7th December 2006, Hamburg, Germany. The reduction of vertical air motion is obtained by applying the method of Orr and Kropfli (1999), with height bins of 270 m, reflectivity bins of 1 dB, minimum number of points for the time averages equals to 500 points, minimum number for the power-law 5.2 best-fit equals to 10. Negative velocities are downwards.

which are parallel, indicate stable cloud systems, composed of particles that maintain similar shape and size distribution as they grow in their fall through the cloud layer. Strong changes in slope from one level to the adjacent one indicates, instead, that microphysical changes are occurring between these levels, such as aggregation or change of the particle phase.

To evaluate the performance of this method, let us consider the deep stratiform cloud structure in figure 5.4. To obtain the proper partition of the data before performing the best-fit with equation 5.2, one should proceed as follows. First, data are grouped in height bins i . Then, for every height layer, the data are further grouped in reflectivity bins j . Then the averages $\langle V_D \rangle_{i,j}$ and $\langle Z_e \rangle_{i,j}$ to be used in equation 5.3 can be evaluated. In order to obtain reliable velocity and reflectivity averages, each of these averages should contain an enough large number of data points. Therefore, to improve the vertical resolution by using a smaller value for the height bins, one has to loose resolution in cloud structure by using a larger value for the reflectivity bins. A reasonable number of points would be greater than some hundreds. The grouping of the data for our example of figure 5.4 is shown in figure 5.5, where every

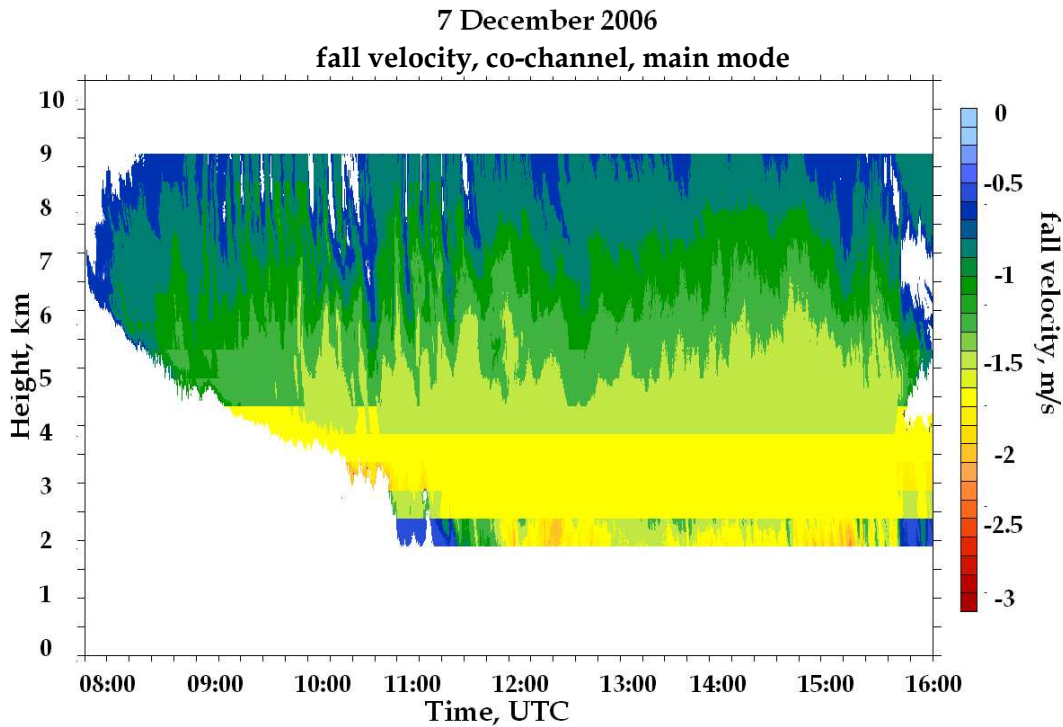


Figure 5.7: As figure 5.6, but with minimum number for the power-law 5.2 best-fit equals to 5. Negative velocities are downwards.

panel represents the scatterplot of V_D against Z_e for a height layer of 270 m centered at the indicated quote. We choose 1 dB for the reflectivity bins, and average only the groups with a minimum number of points of 500. The averages are indicated with a triangle in figure 5.5. When the number of averages for height layer is bigger than 10 we perform the best-fit and use the coefficients α_i and β_i to recalculate the fall velocity of the cloud particles in the i^{th} layer. The result of the application of this method is shown in figure 5.6.

At this point it is clear that, if the partitioned groups were not enough numerous to perform the time average this method could return empty layers for the air vertical motion-free cloud structure. In our example this happens below 4 km and above 9.5 km. Moreover, in one height layer, most of the reflectivity points could bunch in the same reflectivity bin, reducing further the number of points to perform the best-fit.

We apply then this method with different choices of the parameters. For less constraining limits, for example using only 5 points as minimum number for the power-law 5.2 best-fit, it is possible to reconstruct more layers of the cloud, but with a loss in cloud structure resolution (figure 5.7). A single spectra profile for this example is shown in figure 5.8.

In addition this method is of difficult application for automatized routines, because a

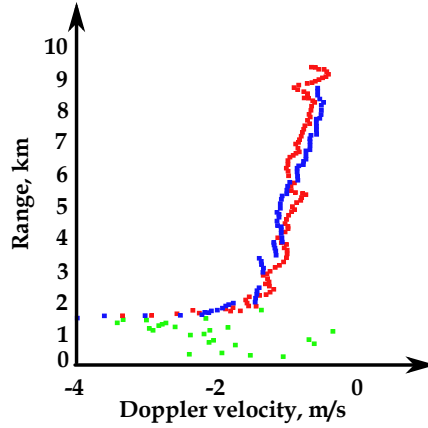


Figure 5.8: Fall velocity, co-channel, main mode, 7th December 2006, 11:49, Hamburg, Germany. Red dots: main mode-specific fall velocity; blue dots: main mode-specific fall velocity with reduction of vertical air motion; green dots: main mode-specific fall velocity for rain (not reliable). The reduction of vertical air motion is obtained by applying the method of Orr and Kropfli (1999), with height bins of 270 m, reflectivity bins of 1 dB, minimum number of points for the time averages equals to 500 points, minimum number for the power-law 5.2 best-fit equals to 5. Negative velocities are downwards.

proper choice for the width of the bins is required for every different case. For these reasons, even if interesting features on the cloud under analysis can be obtained, this method does not appear totally satisfactory.

We decide then for a simplified version of the method, by averaging our data only in time. Anyway, by using short averaging time intervals we still maintain small-scale variability in the cloud structure. Figures 5.9 show the fall velocity for the same example averaged for 5 minutes (upper panel) and 15 minutes (lower panel). The variability in the cloud structure is still recognizable in both cases.

In order to calculate the proper fall velocity and microphysical parameters, such as size and Ice Water Content, in the following we will average the measurements for 5 minutes, with the foresight to choose stable stratiform cloud structures.

We know that for an individual ice cloud particle the terminal fall velocity v_t is related to a size of the particle (for example the maximum dimension D_M) by the power law (see section 2.7, at page 22):

$$v_t(D_M) = \mathcal{A} D_M^{\mathcal{B}} \quad , \quad (5.5)$$

with \mathcal{A} and \mathcal{B} parameters depending on the kind of crystal.

On the other hand, atmospheric profilers (such as vertically pointing cloud radar systems) measure the vertical velocity of an ensemble of cloud particles, specifically the reflectivity weighted fall velocity (see section 3.9, page 53):

$$V_t = \frac{\int v_t S_{v_t}(v_t) dv_t}{\int S_{v_t}(v_t) dv_t} \quad . \quad (5.6)$$

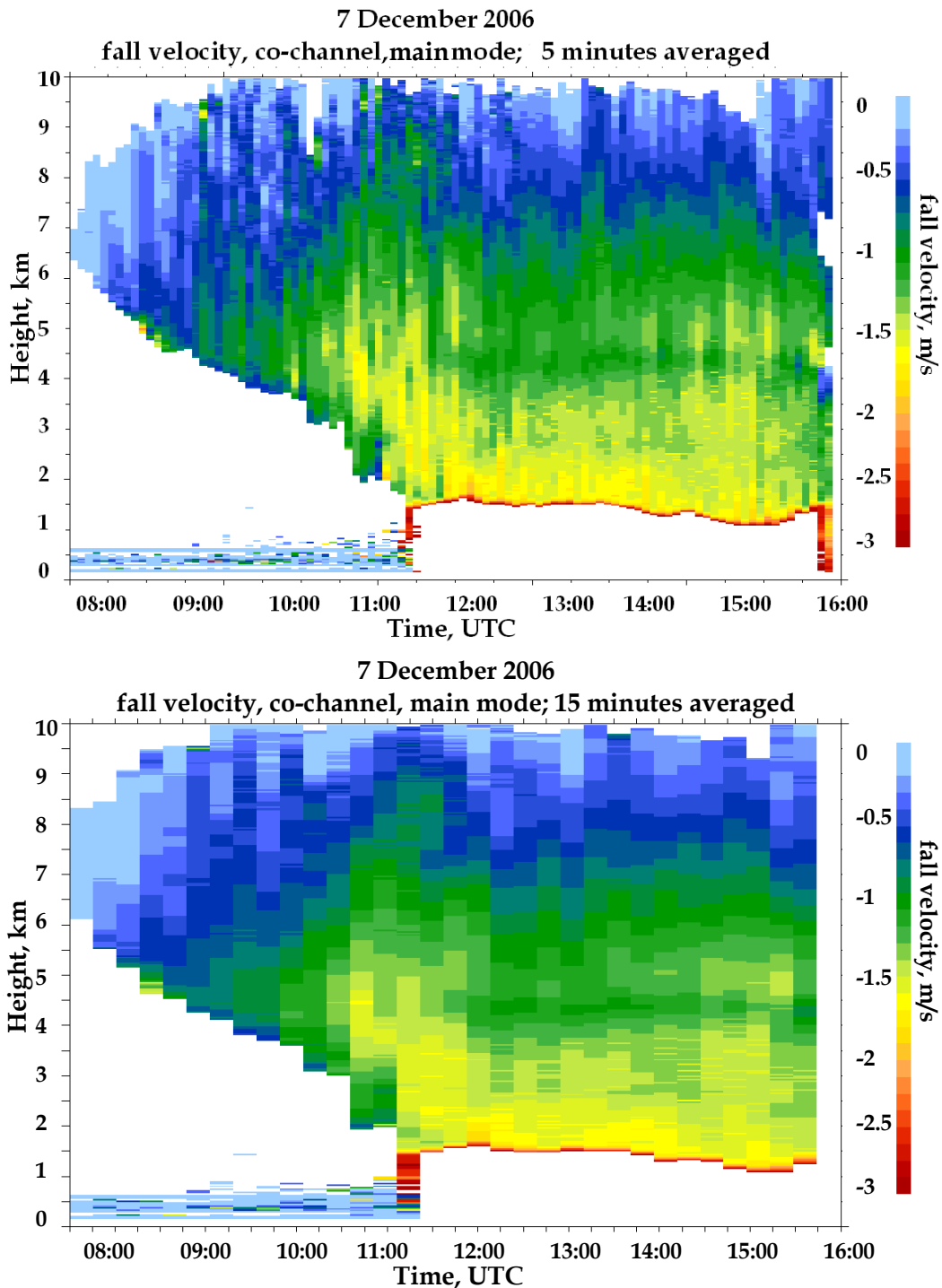


Figure 5.9: Fall velocity, co-channel, main mode, 7th December 2006, Hamburg, Germany. The reduction of vertical air motion is obtained by averaging the data in time: 5 minutes in the upper panel, 15 minutes in the lower panel. Negative velocities are downwards.

Note that we use capital letters for the velocity of the ensemble of particles to distinguish it from the velocity of one single particle.

Matrosov and Heymsfield (2000) have derived that in the Rayleigh scattering regime equation 5.6 can be rewritten as:

$$V_t = \mathcal{A} a_1(\mathcal{B}) D_0^{\mathcal{B}} \quad , \quad (5.7)$$

with D_0 the median volume diameter, which describes the particle size distribution of the ensemble of particles⁴.

In order to reach this result they have substituted in equation 5.6 the individual fall velocity with relation 5.5, and the reflectivity factor with relation 3.24 through 3.61:

$$V_t = \frac{\int K_\rho Q_r \mathcal{A} D_M^{\mathcal{B}} N(D_M) D_M^6 dD_M}{\int K_\rho Q_r N(D_M) D_M^6 dD_M} \quad , \quad (5.8)$$

where K_ρ and Q_r are corrections needed because with the particle diameter also bulk density and shape change.

The parameter K_ρ represents the changes of the complex reflective index of ice relative to the one of water, that can be approximated with the relation:

$$K_\rho \approx 0.23 \cdot \rho^2 \quad . \quad (5.9)$$

The shape parameter Q_r , r being the axis ratio of the particles, represents the tendency of non-spherical particles to scatter more radiation than spherical particles with the same volume. For oblate particles the shape parameter varies with the axis ratio as:

$$Q_r = r^{0.41 \cdot \rho} \quad , \quad (5.10)$$

with the density ρ expressed in g/cm³.

Matrosov and Heymsfield (2000) have considered the PSD being properly described by a gamma function distribution of order n :

$$N(D_M) = N_0 D_M^n e^{-\frac{3.67+n}{D_0} D_M} \quad , \quad (5.11)$$

with D_0 the median volume diameter.

Then equation 5.8 becomes:

$$V_t = \frac{\int K_\rho Q_r \mathcal{A} D_M^{\mathcal{B}} N_0 D_M^n e^{-\frac{3.67+n}{D_0} D_M} D_M^6 dD_M}{\int K_\rho Q_r N_0 D_M^n e^{-\frac{3.67+n}{D_0} D_M} D_M^6 dD_M} \quad . \quad (5.12)$$

Matrosov and Heymsfield (2000) have besides assumed that particle bulk density ρ , shape r , and coefficients \mathcal{A} and \mathcal{B} do not change with the size D_M . Then:

$$V_t = \frac{\mathcal{A} \int D_M^{\mathcal{B}+n+6} e^{-\frac{3.67+n}{D_0} D_M} dD_M}{\int D_M^{n+6} e^{-\frac{3.67+n}{D_0} D_M} dD_M} \quad . \quad (5.13)$$

⁴The median volume diameter D_0 of a distribution of particles is defined such that the particles with diameter less than D_0 contribute to half of the total mass.

With the substitution:

$$D = \frac{3.67 + n}{D_0} D_M \implies D_M = \frac{D_0}{3.67 + n} D$$

$$dD = \frac{3.67 + n}{D_0} dD_M \implies dD_M = \frac{D_0}{3.67 + n} dD$$

we obtain:

$$V_t = \mathcal{A} \frac{\int \left(\frac{D_0}{3.67+n}\right)^{\mathcal{B}+n+6} D^{\mathcal{B}+n+6} e^{-D \frac{D_0}{3.67+n}} dD}{\int \left(\frac{D_0}{3.67+n}\right)^{n+6} D^{n+6} e^{-D \frac{D_0}{3.67+n}} dD}$$

$$= \mathcal{A} \left(\frac{D_0}{3.67+n}\right)^{\mathcal{B}} \frac{\int D^{\mathcal{B}+n+6} e^{-D} dD}{\int D^{n+6} e^{-D} dD} .$$

Noting that the gamma function of order n is defined⁵ as:

$$\Gamma(n) = (n-1)! = \int x^{n-1} e^{-x} dx ,$$

the final result for equation 5.7 is:

$$V_t = \mathcal{A} \left(\frac{D_0}{3.67+n}\right)^{\mathcal{B}} \frac{\Gamma(\mathcal{B}+n+7)!}{\Gamma(n+7)!}$$

$$= \mathcal{A} \left(\frac{D_0}{3.67+n}\right)^{\mathcal{B}} \frac{(\mathcal{B}+n+6)!}{(n+6)!} , \quad (5.14)$$

that gives equation 5.7 with:

$$a_1(\mathcal{B}) = \left(\frac{1}{3.67+n}\right)^{\mathcal{B}} \frac{(\mathcal{B}+n+6)!}{(n+6)!} . \quad (5.15)$$

Through the analysis of a large data set, Matrosov and Heymsfield (2000) have found that \mathcal{B} is correlated to \mathcal{A} , and that \mathcal{A} decreases consistently with increasing size, in the extent of:

$$\mathcal{B} \approx 0.17 \mathcal{A}^{0.24}$$

$$\mathcal{A} = 3.5 \cdot 10^4 D_0^{-0.62} , \quad (5.16)$$

where \mathcal{A} and \mathcal{B} are in cgs units and D_0 in μm . Comparing equation 5.5 for a single ice particle with equation 5.7 for an ensemble of particles, one note that the terminal velocity vs. size relationships differ only in the proportionality coefficients a_1 .

⁵<http://mathworld.wolfram.com/GammaFunction.html>

5.4 Diameter and IWC

A measure of the diameter for an ensemble of particles can be given once that the terminal velocity has been retrieved.

When dealing with ice crystals we have to face with a number of values for the coefficients \mathcal{A} and \mathcal{B} for the different habits (see table 2.1), as every species of ice particles has its own relationship describing fall velocity versus diameter.

Matrosov et al. (2002) have overcome this problem by extrapolating a general rela-

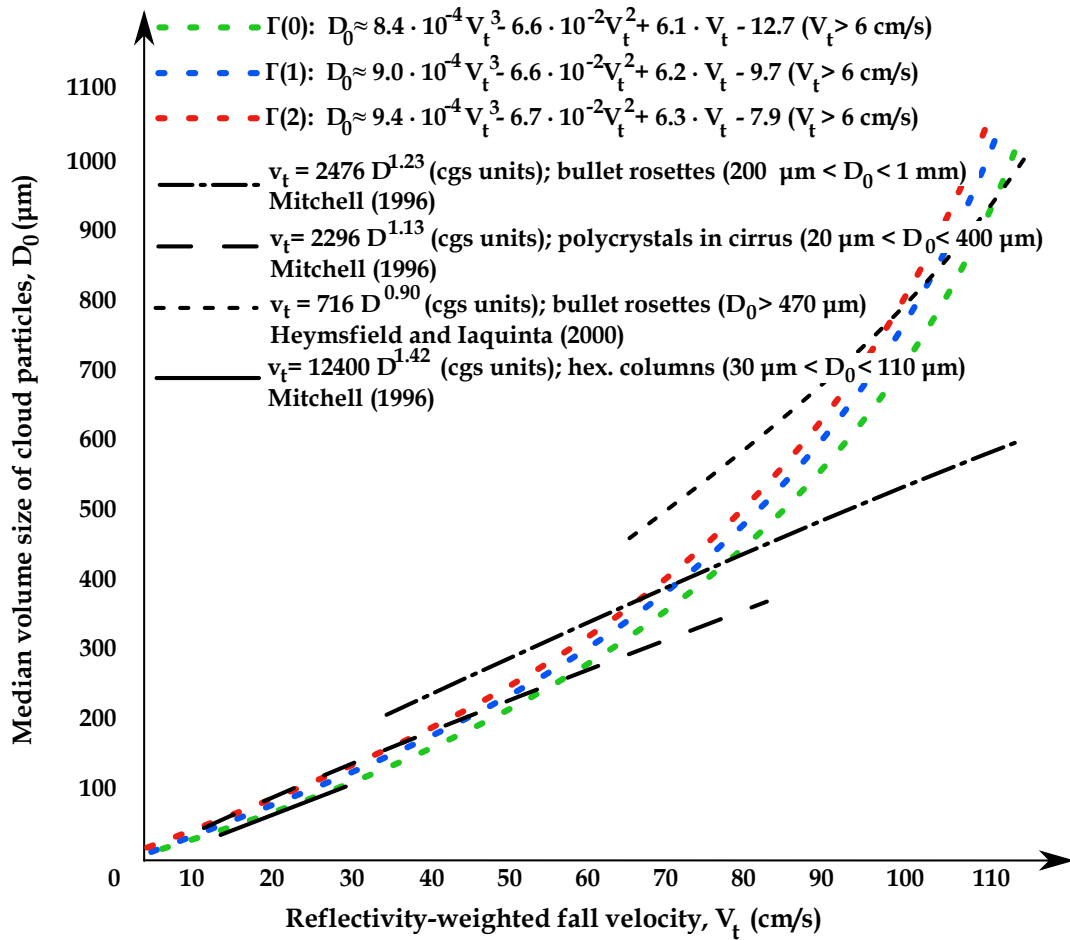


Figure 5.10: D_0 vs. V_t relations for different assumptions of the Particle Size Distribution. Colored dotted lines show the gamma–function Particle Size Distributions for $n = 0$ (green), $n = 1$ (blue), and $n = 2$ (red). Black lines show results of calculations using data from Mitchell (1996) and Heymsfield and Iaquinta (2000) with constant values of \mathcal{A} and \mathcal{B} . The best polynomial fit for the different values of n is given at the top of the figure. From Matrosov et al. (2002), with the permission of the author.

tionship which approximates fall velocity versus diameter with enough accuracy for most of the ice particles habits measurable with cloud radars.

The authors have considered equation 5.7, and have made use of equations 5.15 and 5.16 for a_1 and \mathcal{A} . They have calculated the values of fall velocity for different assumption for the Particle Size Distribution, by varying the order n of the gamma distribution. The curves obtained for $n = 0, 1, 2$ along all the range of variability for velocity and diameter describe satisfactory the experimental ones determined for different habits of ice crystal (figure 5.10). Being these curves of not easy inversion, one can simply perform a best polynomial fits for the different orders n . Kosarev and Mazin (1991) have shown that $n = 0, 1$, or 2 is suitable to describe observed particle size spectra in ice clouds. In this study we use the relationship found by Matrosov et al. (2002) for D_0 as function of V_t of order $n = 1$:

$$D_0 = 9.0 \cdot 10^{-4} V_t^3 - 6.6 \cdot 10^{-2} V_t^2 + 6.2 V_t - 9.7 \quad , \quad V_t \geq 6 \text{ cm/s} \quad . \quad (5.17)$$

Diameters calculated by following equation 5.17 for the example shown in figure 5.11 with 5 minutes average are shown in figure 5.12.

Figure 5.11 shows another case of deep raining stratiform cloud, with the melting layer at about 1 km ; the values below it are shadowed as not reliable (the decomposition algorithm is thought for cloud particles only). Again, as for the cloud structure shown in figure 5.4 we recognize double modes around the cloud boundaries, above the melting layer throughout the event, and in a big cell of 3 km between 00:00 and 06:00 UTC. The secondary mode-specific LDR is computable for this cell only, and it is about -10 dB , whereas the corresponding values for the main mode are about -20 dB . Therefore we have well separated values supporting the claim that this represents a mixed phase cell in the considered event.

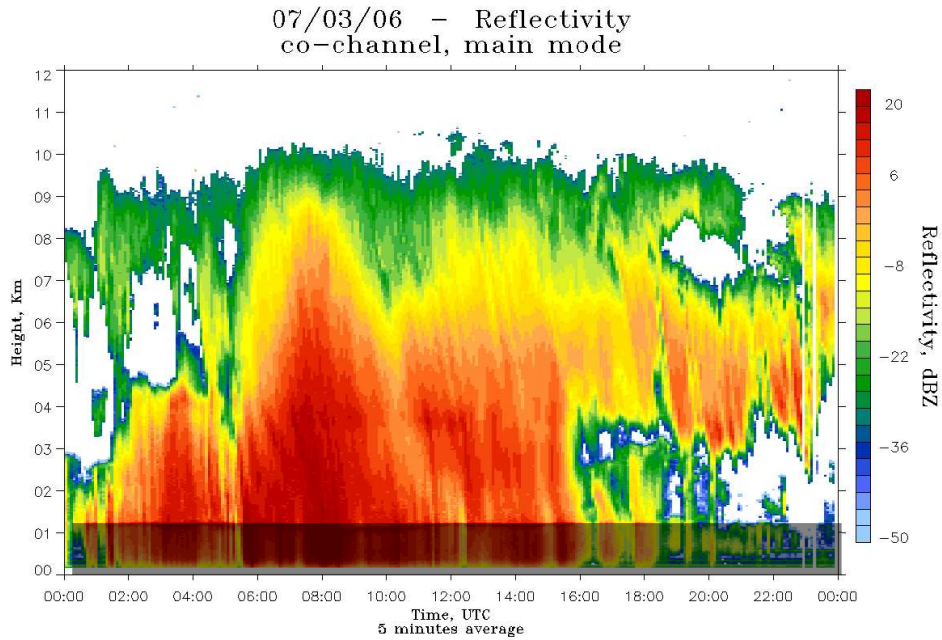
The most accepted way to evaluate Ice Water Content of ice clouds (or iced portions of clouds) is to use the relationship proposed by Atlas et al. (1995), that relate equivalent reflectivity factor with the median diameter of the particles:

$$Z_e = G D_0^3 \text{ IWC} \quad , \quad (5.18)$$

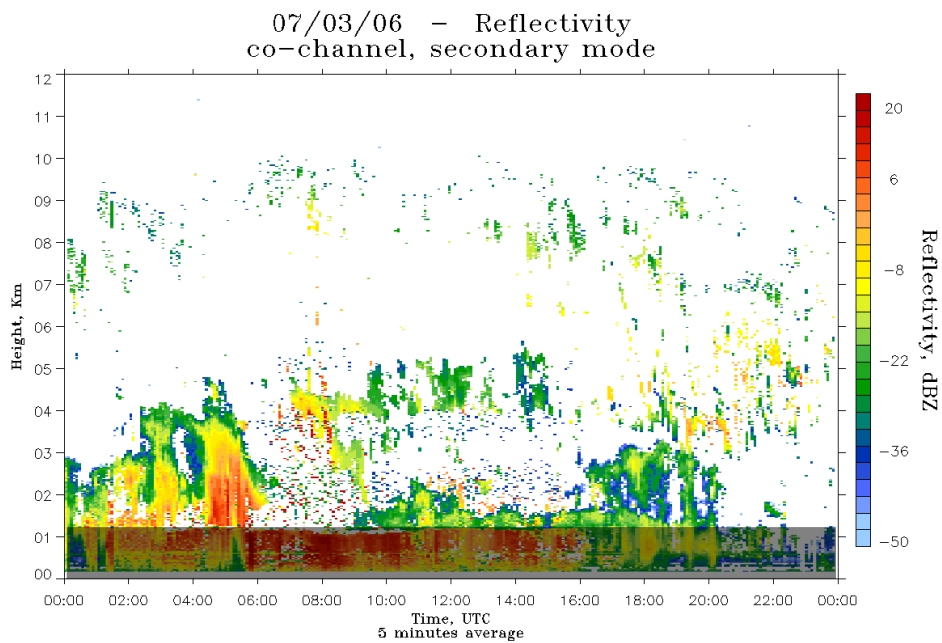
with Z_e in mm^6/m^3 , IWC in g/m^3 , and D_0 in μm . The coefficient G depends on shape and bulk density of the particles, and on the Particle Size Distribution. One can in reason consider the most little ice particles, i.e. with diameters shorter that $50 \mu\text{m}$, having solid ice density; in this case the value of G is constant and equal to 10^{-6} . Otherwise it decreases with the diameter as:

$$G = 7.5 \cdot 10^{-5} D_0^{-1.1} \quad . \quad (5.19)$$

An example of IWC evaluated by following equation 5.18 for the same case study of the previous sections is shown in figure 5.13.

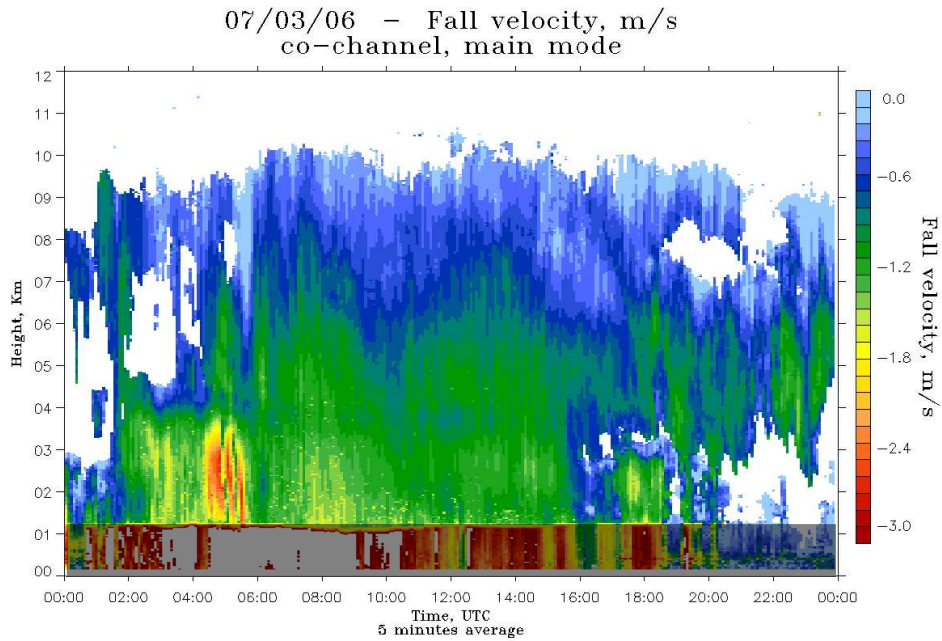


(a) Main mode reflectivity

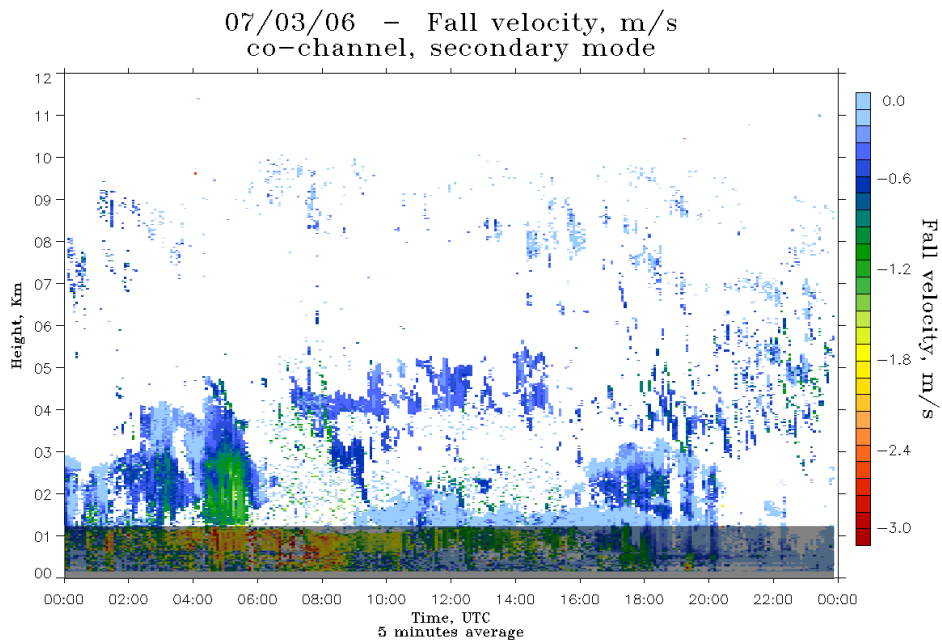


(b) Secondary mode reflectivity

Figure 5.11: Main and secondary mode-specific reflectivity, fall velocity and LDR for the 6th March 2007, Hamburg, Germany. Values below the melting layer at about 1 km are shaded as not reliable.

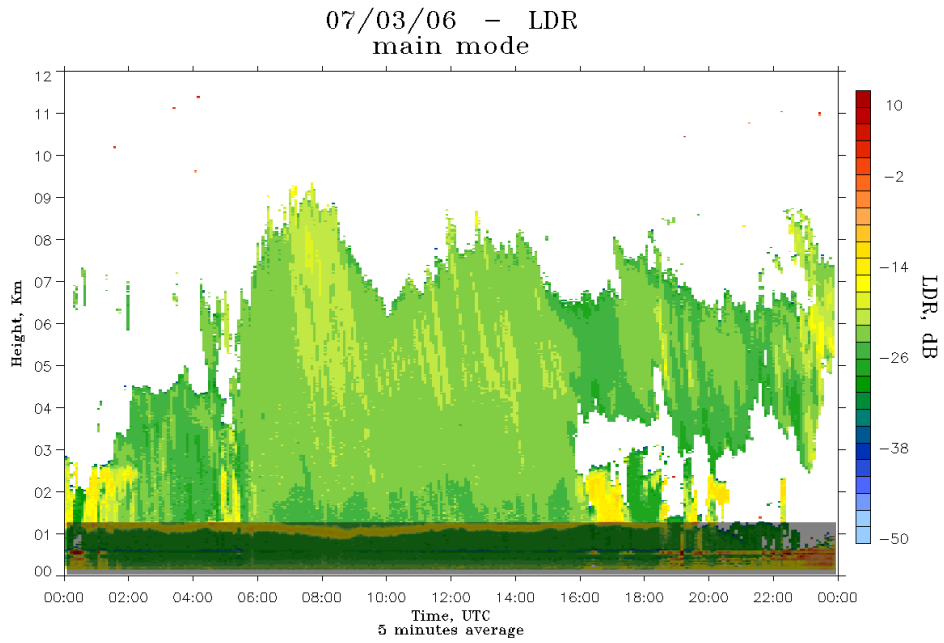


(c) Main mode fall velocity

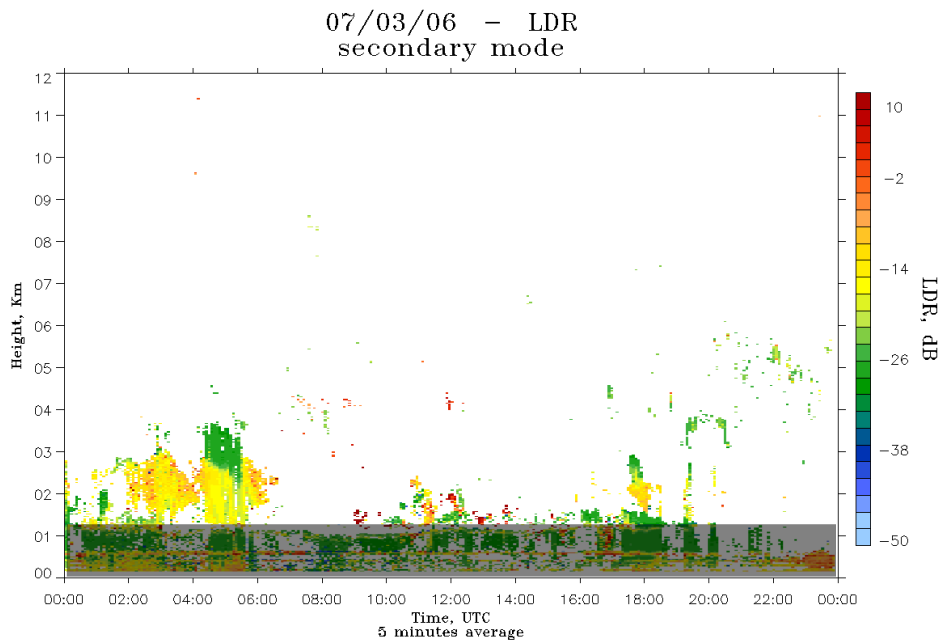


(d) Secondary mode fall velocity

Figure 5.11: Cont.



(d) Main mode LDR



(e) Secondary mode LDR

Figure 5.11: Cont.

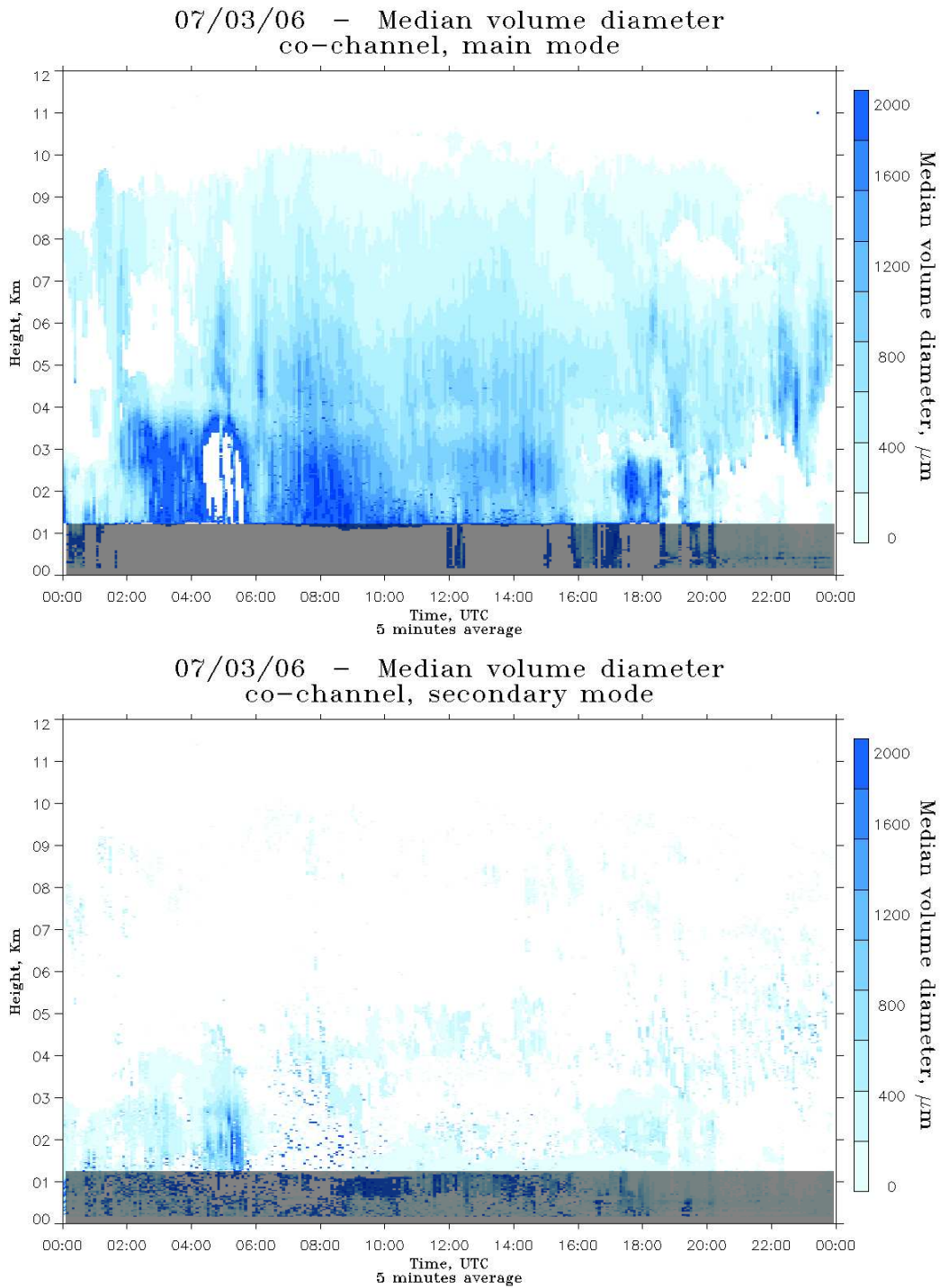


Figure 5.12: Particle diameters, co-channel, main and secondary mode, 6th March 2007, Hamburg, Germany. Evaluated applying equation 5.17 to the velocities shown in figures 5.12c and 5.12d. The shaded values below the melting layer are not reliable.

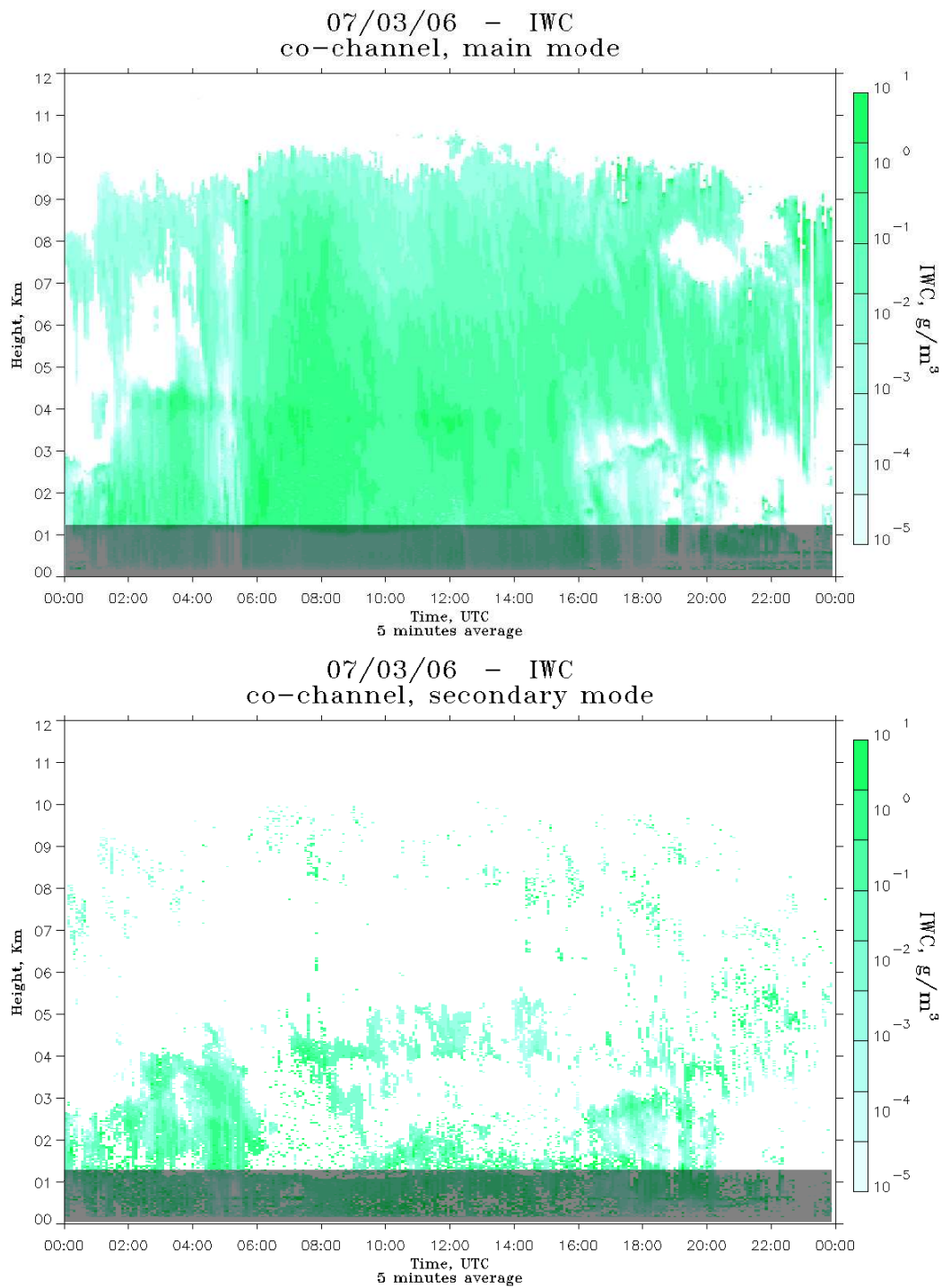


Figure 5.13: IWC, co-channel, main and secondary mode, 6th March 2007, Hamburg, Germany. Evaluated applying equation 5.18 to the data shown in figures 5.12. The shaded values below the melting layer are not reliable.

5.5 Rate of increasing of fall velocity in clouds

When developing the decomposition algorithm, our hypothesis was that every peak in a spectrum corresponds to a mode and that every mode corresponds to one class of cloud particles, which evolves descending to the surface. Therefore, if it would be possible to establish a relation within one mode along the height range on a spectra profile, we could improve our understanding of evolution processes for cloud particles.

Let us first consider the example of vertical profiles of fall velocity shown in figure 5.14. We note that the Doppler velocity of the main mode tends to constantly increase (i.e. it becomes more negative) while approaching the cloud base. In order to analyze systematically this behavior we fit, with a least absolute deviation method, the main mode-specific velocity values to a linear dependence on the vertical range:

$$V_D = V_{D0} + s \cdot H \quad , \quad (5.20)$$

with H the vertical range, and V_{D0} and s the coefficients for the linear fit.

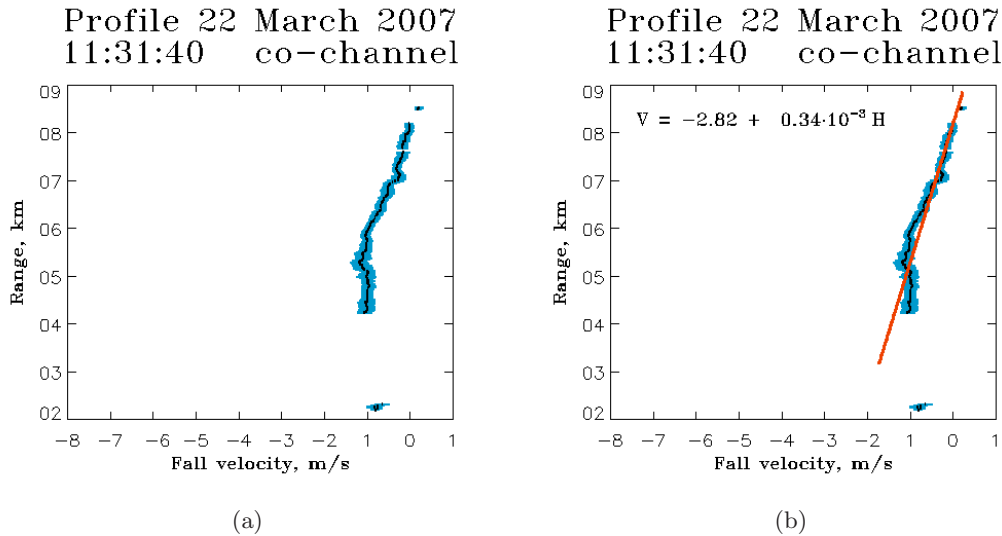


Figure 5.14: **(a)**: main and secondary mode-specific spectral moments (indicated respectively by black dots and blue bars). The main mode fall velocity (with negative velocities downwards) shows a constant increase in fall velocity from the cloud top to the cloud base. **(b)**: the main mode fall velocity is fitted along the vertical extension of the cloud. The result is illustrated by the red solid line, and the relative equation for the fit is given on the panel. Referring to equation 5.20, V_D is given in m/s, the intercept in m/s, the slope in s^{-1} , and H in m. The slope value of $0.34 \cdot 10^{-3} s^{-1}$ means that the fall velocity increases in average of 34 cm/s per kilometer fall path.

The slope s of the fit gives an indication of the increasing of fall velocity per unit path along the examined spectra profile, for example a mean value of about $0.10 \cdot 10^{-3} \text{ s}^{-1}$ corresponds to an increase of fall velocity of 10 cm/s per kilometer fall path. We interpret this behavior as the consequence of ice particles growth (see section 2.3).

In figure 5.14b the result of the fitting is presented. The vertical range for the fit extends from the cloud bottom up to the cloud top. We apply this analysis to different kind of cloud structures (figures 5.15, 5.16, and 5.17). In order to exclude data from raindrops, in case of raining clouds we choose as lower bound for the fit the level just above the melting layer (5.15 and 5.16)). Furthermore, we decide to not extend this analysis to secondary mode spectra profiles: cases in which there are enough points to obtain a reliable fit (at least one hundred), as in figure 5.16, are extremely rare.

At a first glance the downward direction of the Doppler velocity is surprising, because the mean vertical wind within active clouds should be directed upward with fast enough speed to carry cloud droplets upward, thus inducing their growth by condensation, as for the profile shown in figure 5.17. We explain the observed downward velocity with the very strong weighting of large hydrometeors in the radar echo (proportional to the 6th power of the diameter). In fact, the Doppler

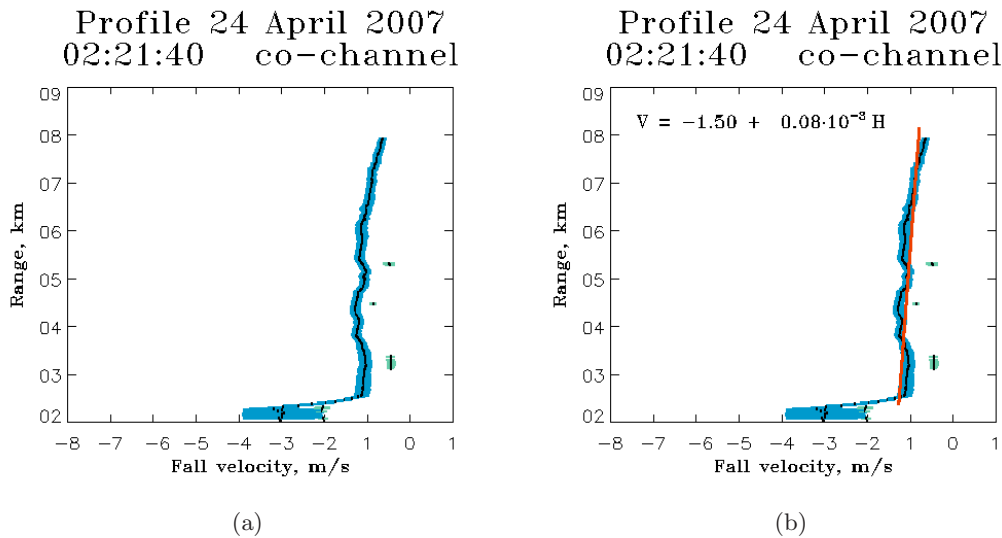


Figure 5.15: (a): main and secondary mode-specific spectral moments (see also figure 5.14); (b): the main mode fall velocity is fit along the vertical extension of the cloud up to the melting layer (red solid line).

The main mode fall velocity (with negative velocities downwards) shows a constant increase in fall velocity from the cloud top to the cloud base. The slope value of $0.08 \cdot 10^{-3} \text{ s}^{-1}$ means that the fall velocity increases in average of 8 cm/s per kilometer fall path.

velocity is mostly dominated by those hydrometeors which grow on their upward travel by a sufficient amount so that their terminal fall velocity exceeds the updraft of ambient air. Accordingly, the increasing Doppler velocity on the fall path may be explained as the consequence of particle-growth due to various microphysical interaction processes occurring on the encounter of other hydrometeors existing on the fall path.

The analysis of time series of slopes s reveals that the mean rate of increasing of fall velocity assumes a fairly constant value within the same cloud structure (as shown in figure 5.18), but may vary for different clouds. We believe that the observed (and fairly stable) rate of increasing of fall velocity in a cloud structure represents a useful parameter to be taken into consideration for the validation of modeling of related microphysical processes.

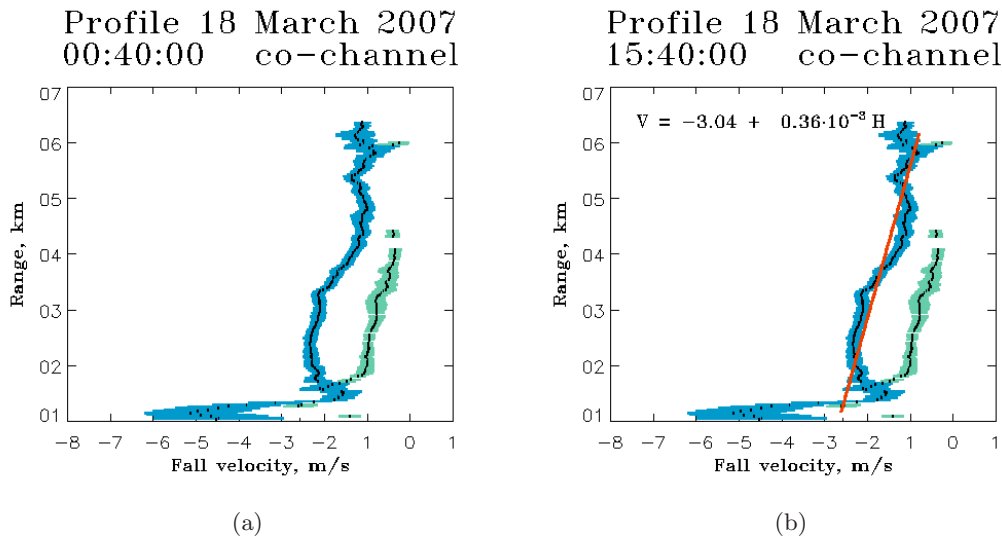


Figure 5.16: (a): main and secondary mode-specific spectral moments indicated respectively by black dots and blue or green bars (see also figure 5.14); (b): only the main mode fall velocity is fitted along the vertical extension of the cloud up to the melting layer (red solid line).

The main mode fall velocity (with negative velocities downwards) shows a constant increase in fall velocity from the cloud top (corrupted by turbulence) toward the cloud base and a slight decrease before the melting layer. The slope value of $0.36 \cdot 10^{-3} \text{ s}^{-1}$ means that the fall velocity increases in average of 36 cm/s per kilometer fall path.

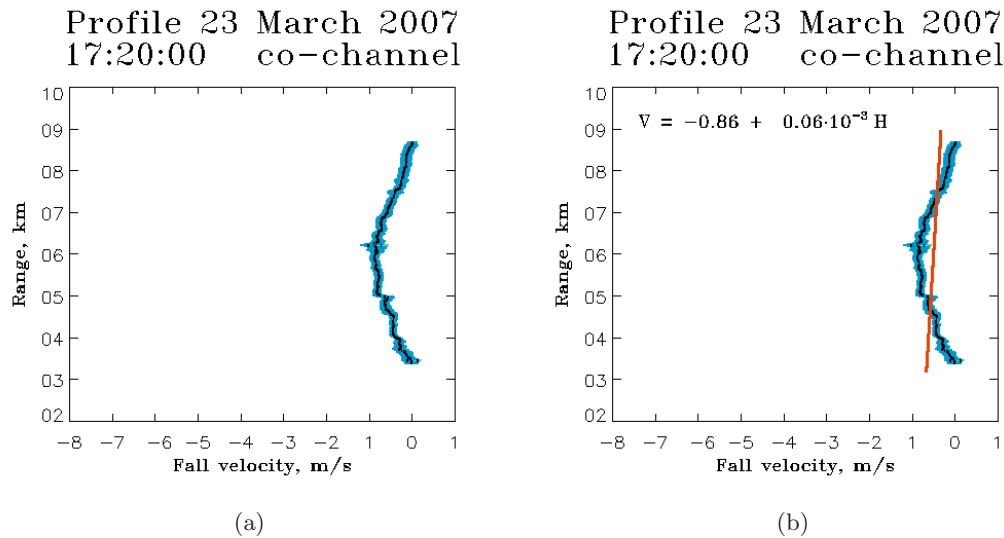


Figure 5.17: (a): main and secondary mode-specific spectral moments (see also figure 5.14); (b): the main mode fall velocity is fitted along the vertical extension of the cloud (red solid line). The main mode fall velocity (with negative velocities downwards) shows an increase in fall velocity from the cloud top to the center of the cloud, and then a decrease in its course to the cloud base.

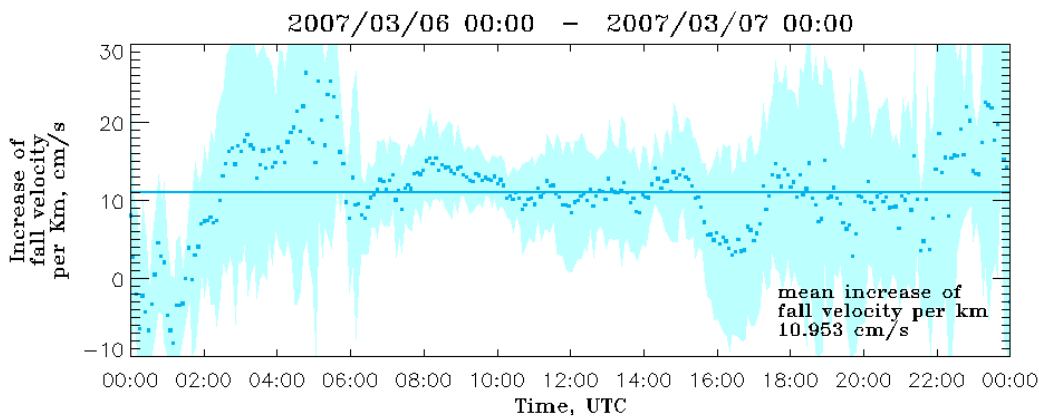


Figure 5.18: Time series of rate of increasing of fall velocity for the 6th March 2007 (THI for the fall velocity, co-channel, main mode, in figure 5.12c). The fit is repeated after reducing the vertical air motions. In the case here shown, the rate of increase of fall velocity per km fall path is stabilized at about 11 cm/s. Light blue points: increase of fall velocity per spectra profile; Light blue straight line: mean value of the increase of fall velocity; the vertical bars indicate the corresponding error for the fit 5.20, every profile consisting of at least 100 range gates. The mean values represent 360 profiles per hour.

Chapter 6

Application of the decomposition algorithm: comparison with model

Grad School:
It seemed better than getting a real job.
Jorge Cham

6.1 Introduction

In this chapter we show the comparison of the retrievals obtained by applying the decomposition algorithm developed in chapters 4 and 5 with the ones predicted by a non operational configuration of the COSMO-DE model, particularly for one case study.

The COSMO model (Consortium for Small-Scale Modelling) is a limited-area atmospheric prediction model. In nature several physical processes are likely to take place for the formation and growth of cloud particles, especially in mixed-phase clouds (see chapter 2). The configuration of the model here used includes the explicit microphysical parametrization of processes taking place between cloud droplets and raindrops, including cloud droplets nucleation (see section 2.2.1), and of processes between cloud droplets and ice phase, where cloud ice, snow flakes and graupel are distinguished.

This cloud microphysical scheme predicts then the mixing ratio of five hydrometeor types, nominally cloud droplets, raindrops, cloud ice, graupel, and snowflakes in terms of number as well as mass densities and number concentration.

For details about the model configuration see Seifert and Beheng (2006).

We will consider microphysical properties such as size and Ice Water Content (IWC) and the growing rate of hydrometeors along the vertical cloud extension.

A proper parameterization of cloud microphysical processes for Numerical Weather Prediction (NWP) and for climate modeling is an actual issue, as every cloud represents a complex system to be described with a numerical physically consistent treatment. More detailed the mathematical description, more computationally costly the prediction results.

We believe that the retrievals here shown combined with model predictions will bring us to a deeper understanding of the microphysical processes that are happening within a mixed-phase cloud.

6.2 Case study: 7 December 2006

During the 7th December 2006 a warm front associated to a low pressure system passed over Hamburg (figure 6.1). Over the day a moderate precipitation rate and temperatures at the ground ranging from 4°C to 8°C were registered.

The application of the decomposition algorithm to this case is discussed in chapter 5; particularly some results are outlined in sections 5.2 and 5.3.

Although vertical air motions could be obtained with 5 minutes averages, here it is obtained by 15 minutes averages, to conform to the time resolution of the model. The mode-specific fall velocities, diameters, and Ice Water Content for the co-channel are shown in figures from 6.2 to 6.4.

Looking at the main mode-specific retrievals, we deduce this being an ice cloud, with ice crystals of some hundreds micron growing along the vertical downwards to snow crystals of 3 mm. The fall velocity increases correspondingly up to 1.8 m/s before melting at about 1.5 km to form rain (non indicated in figures as the results of the decomposition are not correct in case of raindrops).

From the secondary mode-specific plots, we discover the presence of second modes on the cloud top boundary, in a layer of one kilometre above the melting layer between 11:00 and 14:00 UTC, and at 4 km between 14:30 and 15:30 UTC. As discussed in the previous chapter, secondary modes at the cloud top are due to turbulence.

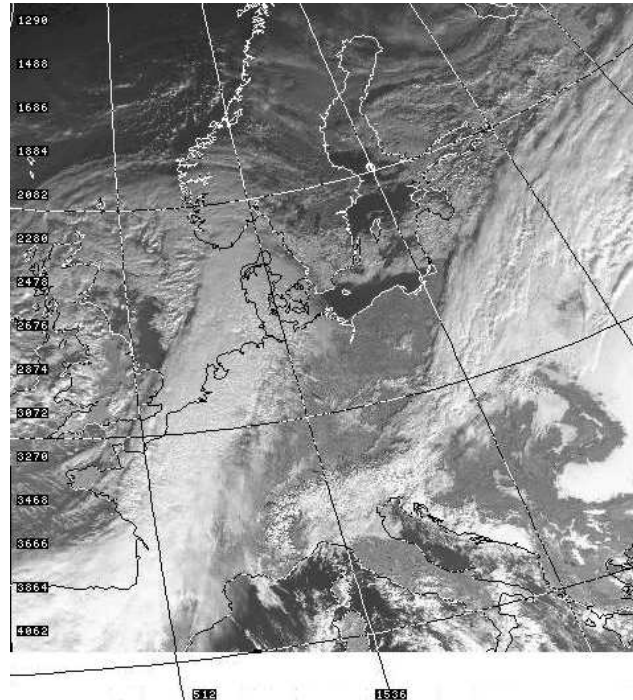


Figure 6.1: Satellite image over East Europe on the 7th December 2006 (Dundee Quicklook for AVHRR, channel 2, near infrared, 07 December 2006 at 10:06 UTC).

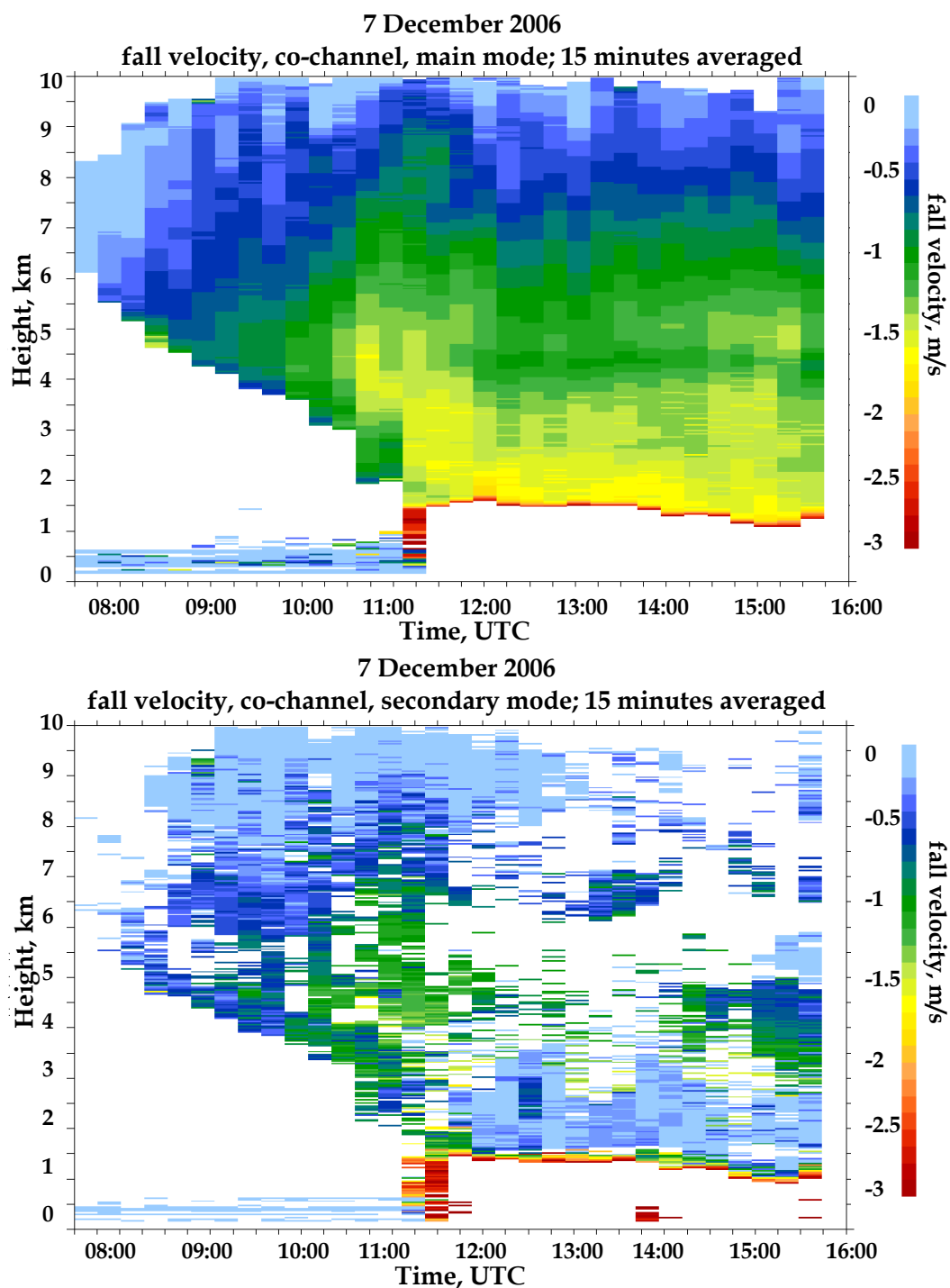
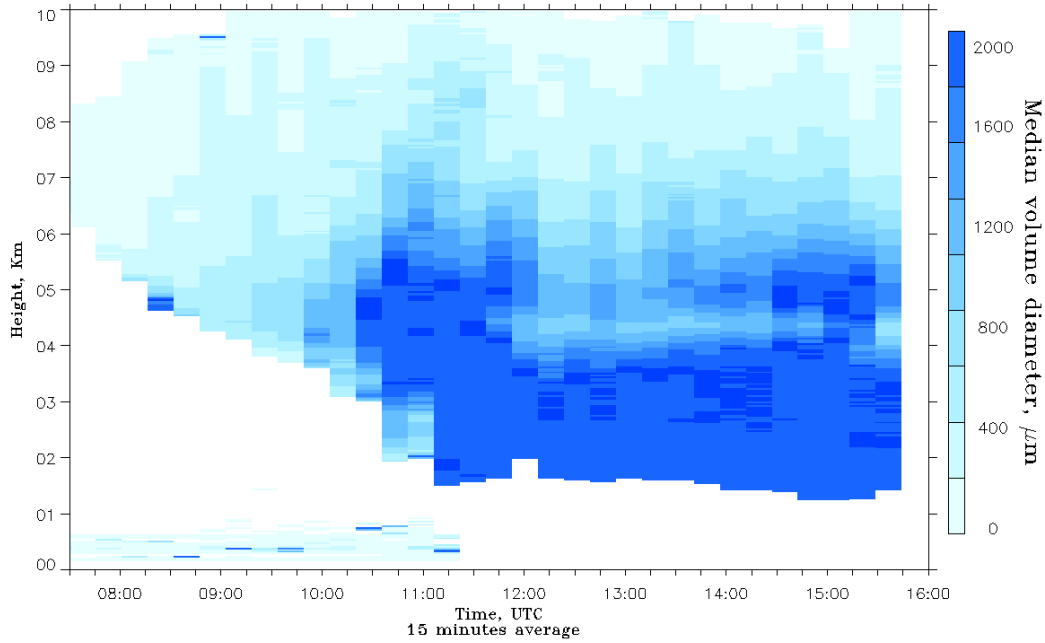


Figure 6.2: Mode-specific fall velocity, co-channel, 15 minutes averaged to reduce the vertical air motions. 7 December 2006, Hamburg, Germany

2006/12/07 07:30 – 2006/12/07 16:00 – Median diameter
co-channel, main mode



2006/12/07 07:30 – 2006/12/07 16:00 – Median diameter
co-channel, secondary mode

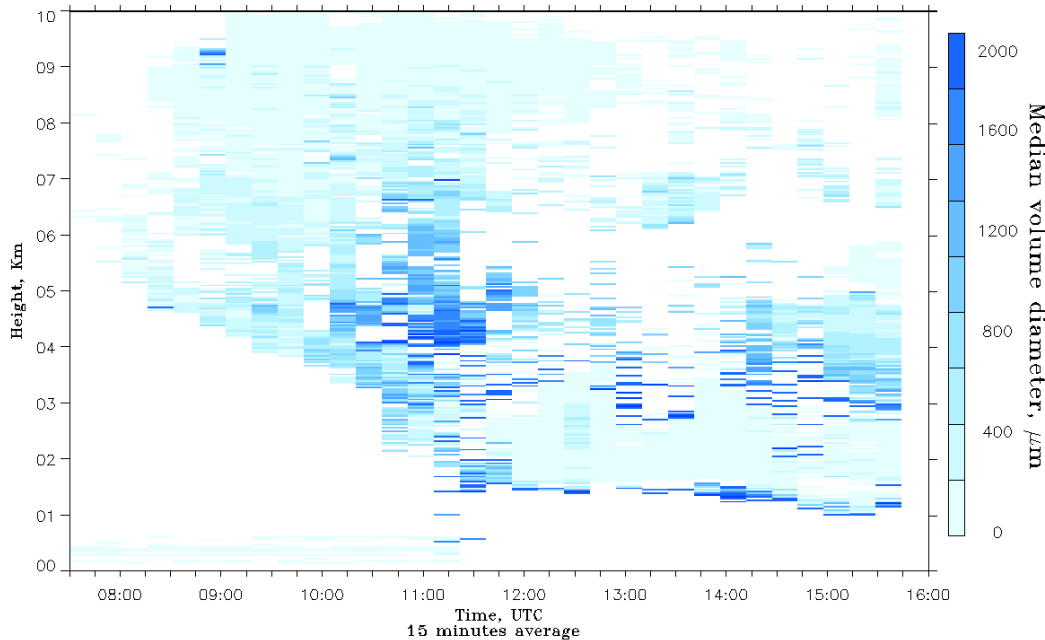
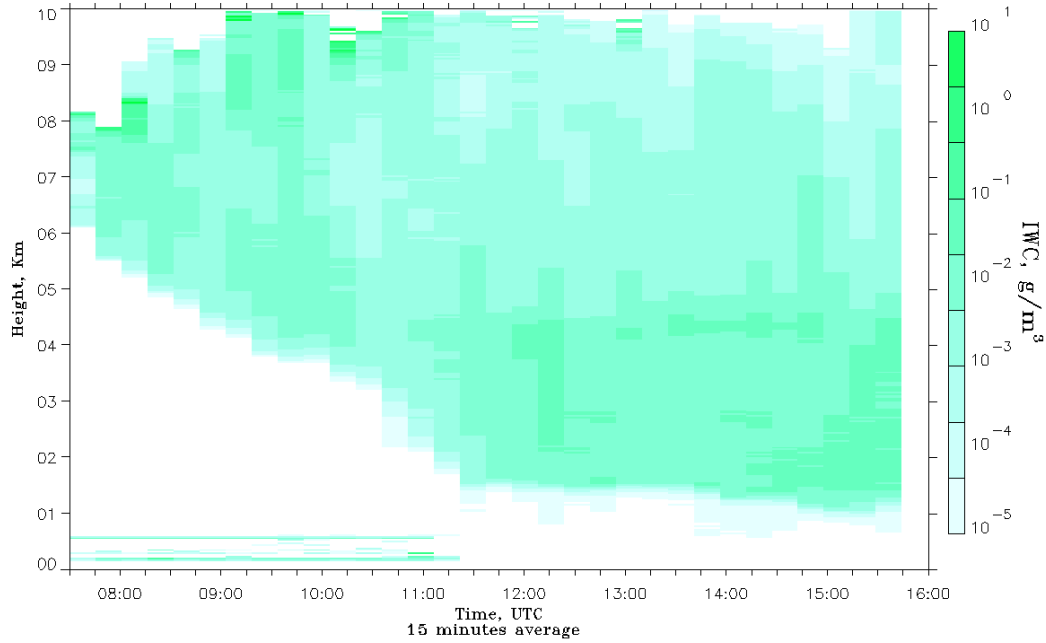


Figure 6.3: Mode-specific median volume diameter, co-channel, 15 minutes averaged to reduce the vertical air motions. 7 December 2006, Hamburg, Germany

2006/12/07 07:30 - 2006/12/07 16:00 - IWC
co-channel, main mode



2006/12/07 07:30 - 2006/12/07 16:00 - IWC
co-channel, secondary mode

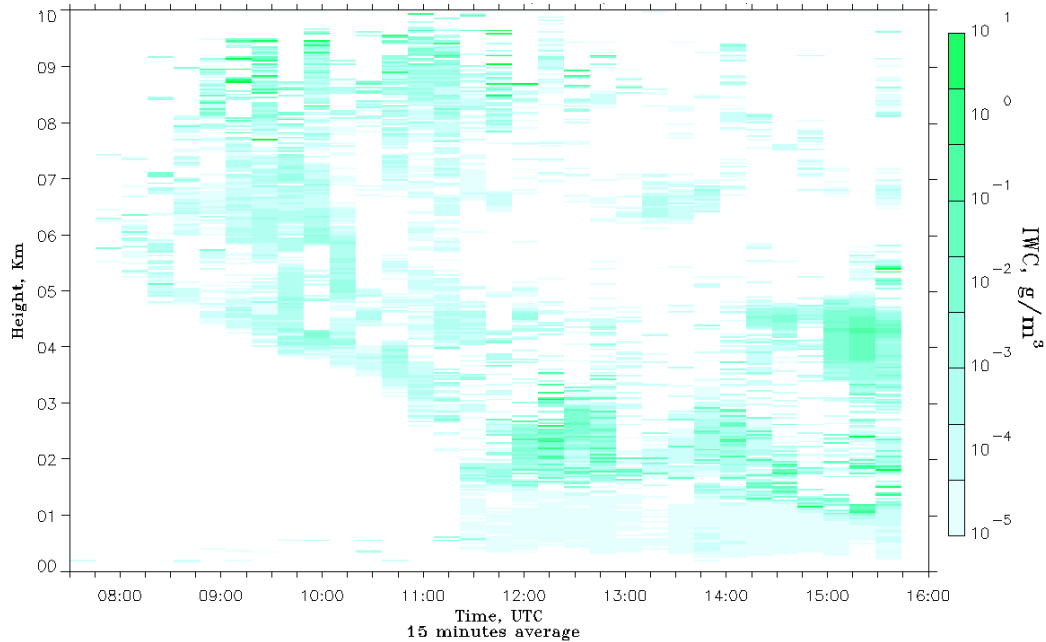


Figure 6.4: Mode-specific IWC, co-channel, 15 minutes averaged to reduce the vertical air motions. 7 December 2006, Hamburg, Germany

At 15:00 UTC the secondary modes are likely due to stronger air motions within the cloud; the visible change in the melting layer height supports this hypothesis. Above the melting layer we face a mixed-phase layer. Behind the doubled fall velocity values, the LDR values are coherently structured along the vertical, suggesting that we deal with two different groups of particles. Let us recall that mixed-phase layers are connected with secondary production of ice (Hallett and Mossop effect, see 2.4.1). This process needs temperatures around -7°C and the presence of both snow crystals and supercooled droplets: snow crystals, rimed by the droplets, splinter out pristine ice crystals. Above the melting layer right conditions of temperature exist that allow this secondary production of ice to occur, because here the temperature decreases from 0°C with increasing height. With cloud radar only we can detect snow crystals (main mode), and supercooled droplets or ice crystals (secondary mode). In order to distinguished among the two, we use the qualitative method suggested by Zawadzki et al. (2001), as seen in section 5.2.

Looking in the model prediction results illustrated in figure 6.5, we note a layer between 1 and 4 km from 12:00 to 18:00 UTC where the model predicts the presence of cloud liquid water along with production of a little amount of graupel. This result further supports our hypothesis about the occurrence of secondary ice production.

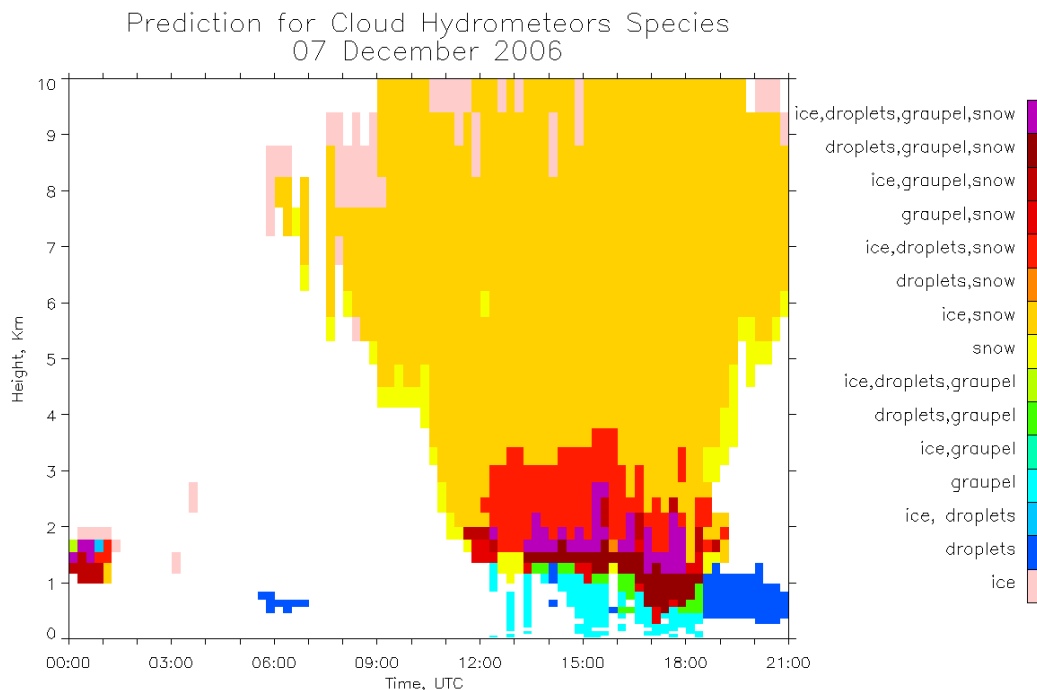


Figure 6.5: Prediction for the different hydrometeors between 00:00 and 21:00 UTC, 7 December 2006, Hamburg, Germany. Red and purple design the areas with cloud droplets and snow or ice crystals.

Whereas the measured velocities are reflectivity weighted, that means with the 6th power of the diameter, the model velocities are weighted with the mass, that means with the 3rd power of the diameter. Although the velocities are weighted differently, the vertical velocities are similar, as one can see in the comparison provided in figures 6.6.

The time series for the increase of the fall velocity evaluated by the model prediction and the one retrieved from the radar data are shown in figure 6.7. The fall velocity of cloud particles increases with an average of about 15 cm/s per kilometre fall path. This value is consistent with the result of the cloud resolving model COSMO-DE, that is about 11.5 cm/s per kilometre fall path. The point values get closer for the deeper part of the cloud, after 10:00 UTC; instead, between 07:00 UTC and 10:00 UTC, the model result do not have enough point values along the vertical to make the fit reliable.

Switching on one growing process at time in the model, such as growth by water vapor deposition, by collection processes, or by freezing of water drops, we shall understand which one is critical in the evolution of the bigger particles in the cloud.

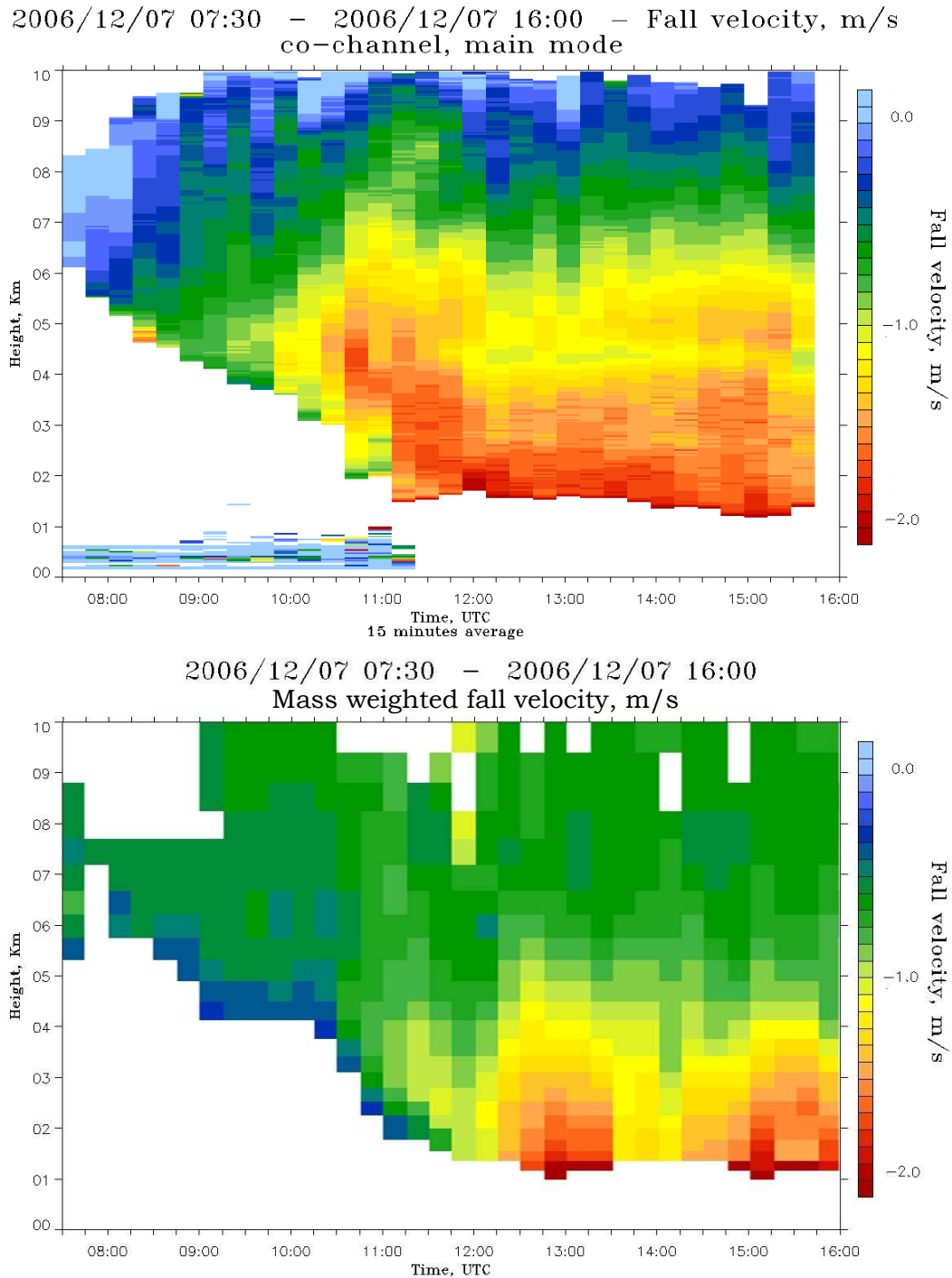


Figure 6.6: Model prediction for the fall velocity 07:30 and 16:00 UTC, 7 December 2006, Hamburg, Germany (lower panel). Comparison with the result retrieved from radar data (upper panel). Negative velocities are downwards.

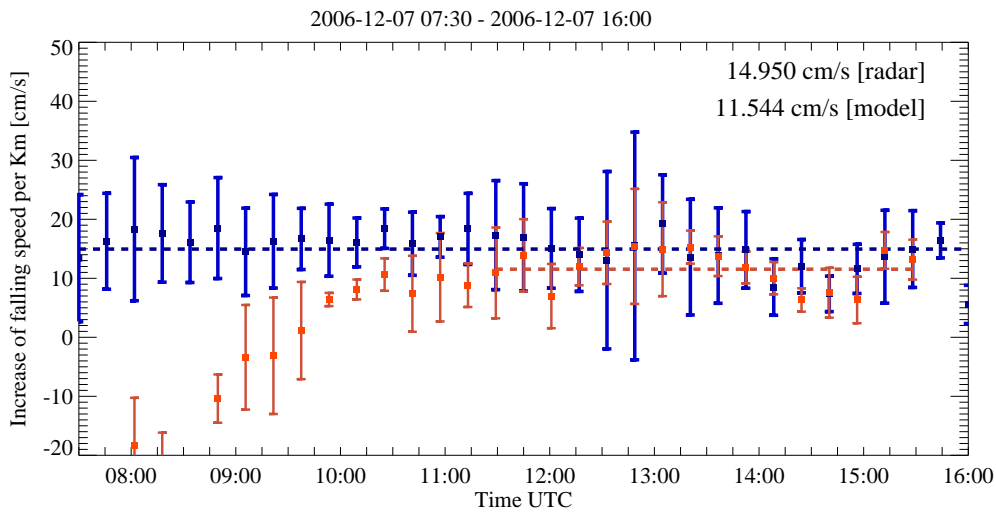


Figure 6.7: Time series of rate of increasing of fall velocity for the 7th December 2006 (see also section 5.5). Blue points: measured increase of fall velocity per spectra profile after reduction of vertical air motion (15 minutes averages); red points: increase of model predicted fall velocity per spectra profile; vertical bars indicate the corresponding mean absolute deviation between the points of each profile and its fit 5.20. Dotted lines: mean value for the increase of fall velocity for measurements and model prediction, red and blue respectively. Mean values are based on 4 values per hour. The model predicted mean value is evaluated considering only the time gates where there are enough point values – at least 20 – to make the fit reliable; that means the model predicted mean value is evaluated for the deeper part of the cloud only.

6.3 Acknowledgments

The author is grateful to Axel Seifert (DWD) for running the cloud model for the benefit of this study.

The authors thank the NERC Earth Observation Data Acquisition and Analysis Service (NEODAAS) for supplying data for this study.

Chapter 7

Summary and Outlook

Cloud radars have an excellent sensitivity to detect cloud particles, but their potential to investigate them is still not fully developed. Against a complex structure of the measured Doppler radar spectra, robust techniques for resolving it do not still exist.

In this work we have described a new operational algorithm which we have developed to decompose in up to two modes Doppler radar spectra.

The rationale of the algorithm is that an ensemble of cloud particles of the same species — the same thermodynamic phase, analogous shape and size — produces a Gaussian spectrum with characteristic parameters, which are related to the moments of the Doppler spectrum.

More ensembles of cloud particles in the same radar resolution volume produce a spectrum that is due to the linear superposition of the Gaussian signals which they would produce singularly.

With the aid of radar polarimetric measurements, each mode can be associate to a different type of cloud particle.

The purpose of the proposed method is the requirement to evaluate mode-specific moments, in contrast with the traditional global moments, in order to retrieve exhaustive information on the microphysical structure of clouds and on the dynamics of cloud systems.

Cloud properties evaluated by cloud radars are size, shape, phase, orientation, concentration, and motion.

We extracted further pieces of information on the properties of the cloud particles by linearly fitting the main mode-specific velocity as a function of the altitude.

The gradient of this fit gives a picture on the growing behaviour of the particles along the vertical.

Therefore physical processes responsible for formation, growth, and evolution of cloud particles can be studied.

This analysis turned to be particularly useful in the recognition and study of mixed-phase layers in deep convective stratiform cloud structures.

Mixed-phase clouds (or sections of clouds) are composed by snowflakes, supercooled droplets, and pristine ice crystals.

Depending on their size, these different classes of particles may show a comparable fall velocity; therefore, with decomposed cloud radar measurements we are able to identify only the two dominant classes.

Nevertheless, for the considered measurements, the melting layer is well visible, and then it is possible to guess the temperature gradient within the vertical extension of the cloud. The detection of double modes together with the study of the ambient conditions allow us to claim the ice secondary nucleation process in mixed-phase layers as responsible for the double modes revealed by the decomposition algorithm.

The algorithm has been developed on measurement taken by a vertically pointing polarimetric Doppler cloud radar MIRA-36, operating at the frequency of 35.5 GHz. The radar was placed in Hamburg, Germany.

The potentiality of the method is illustrated by applying it on radar measurements of deep stratiform convective cloud structures, for which a layer of double modes shows up for a persistent lapse of vertical and temporal extension.

By using measurements taken by more instruments, such as lidars, it would be possible to extend the study to other cloud structures, and a subject of future studies is to understand if the described behaviour is common to clouds of the same type.

For a case study the microphysical results we obtained are compared with the prediction obtained by the COSMO-DE model, showing a suitable agreement. We considered microphysical properties such as size, Ice Water Content, and the growing rate of hydrometeors along the vertical cloud extension.

As this model includes an explicit cloud microphysical parametrization, the use of radar decomposed spectra in numerical cloud models should be considered for testing the current knowledge of the processes involved and for validation and refinement of numerical cloud models itself.

Anyway, the retrieved microphysical properties, i.e. particle diameter and Ice Water Content, require to be validate with in situ data. In this way, also shapes different from a Gaussian for the modeled double spectra, as the exponential one, could be considered and tested.

Bibliography

- Atlas D., R. C. Srivastava, and R. S. Sekhon: Doppler radar characteristics of precipitation at vertical incidence; *Reviews of Geophysics and Space Physics*, **11(1)**, 1-35, 1973.
- Atlas D., S. Y. Matrosov, A. J. Heymsfield, M. Chou, and D. B. Wolff: Radar and radiation properties of ice clouds; *Journal of Applied Meteorology*, **34**, 2329–2345, 1995.
- Bauer-Pfundstein M. R. and U. Görndorf: Target separation and classification using cloud radar doppler–spectra. In *Proceedings 33rd Intern. Conf. on Radar Meteorology*, Cairns, 2007.
- Bergeron, T.: On the physics of clouds and precipitation; Proc. 5th Assembly U.G.G.I., Lisbon, Portugal, **2**, 156–180, 1935.
- V. N. Bringi and V. Chandrasekar. *Polarimetric Doppler Weather Radar: Principles and Applications*. Cambridge University Press, 2001.
- Cantrell W. and A. Heymsfield: Production of ice in tropospheric clouds: a review; *Bulletin of the American Meteorological Society*, **86(6)**, 795–807, 2005.
- Delanoë J., A. Protat, D. Bouniol, A. J. Heymsfield, A. Bansemer, and P. Brown: The characterization of ice clouds properties from Doppler radar measurements; *Journal of Applied Meteorology and Climatology*, **46**, 1682–1698, 2007.
- R. J. Doviak and D. S. Zrnić. *Doppler Radar and Weather Observations*. Academic Press, 1993.
- Findeisen, W.: Kolloid-meteorologische Vorgänge bei Niederschlagsbildung (Colloidal meteorological processes in the formation of precipitation); *Meteorologische Zeitschrift*, **55**, 121-133, 1938.
- U. Görndorf. *Cloud radar*. In: EUR 24172 COST Action 720 Integrated Ground-Based Remote-Sensing Stations for Atmospheric Profiling, 2009.
- Gossard E. E., J. B. Snider, E. E. Clothiaux, B. Martner, J. S. Gibson, R. A. Kropfli, and A. S. Frisch: The potential of 8-mm radars for remotely sensing cloud drop size distributions; *Journal of Atmospheric and Oceanic Technology*, **14**, 76-87, 1997.

- Gunn K. L. S. and T. W. R. East: The microwave properties of precipitation particles; Quarterly Journal of the Royal Meteorological Society, **80**, 522–545, 1954.
- Gunn R. and G. D. Kinzer: The terminal velocity of fall for water droplets in stagnant air; Journal of Meteorology, **6(4)**, 243–248, 1949.
- Hallett J. and S. Mossop: Production of secondary ice particles during the riming process; Nature, **249**, 26–28, 1974.
- Herbert, F.: Relations for H₂O–saturation equilibrium in cloud air; Fischer, G. (ed.), in The Landolt-Brnstein Database, 1987
- Heymsfield, A. J., and J. Iaquina: Cirrus crystal terminal velocities; Journal of the Atmospheric science, **57**, 916–938, 2000.
- Heymsfield A. J., P. C. Kennedy, S. Massie, C. Schmitt, Z. Wang, S. Haimov, and A. Rangno: Aircraft–induced hole punch and canal clouds: inadvertent cloud seeding; Bulletin of the American Meteorological Society, **91(6)**, 753–766, 2010.
- Hildebrand P. H., and R. S. Sekhon: Objective determination of the noise level in Doppler spectra; Journal of Climate and Applied Meteorology, **13**, 808–811, 1974.
- Hitschfeld W. and J. Bordan: Error inherent in the radar measurement of rain fall at attenuation wavelengths; Journal of Meteorology, **11**, 58–67, 1954.
- Hogan R. J. and E. J. O’Connor: Facilitating cloud radar and lidar algorithms: the CloudNet Instrument Synergy/Target Categorization product. CloudNet Project Documentation, 2004.
- Hufford G. A.: A model for the complex permittivity of ice at frequencies below 1 THz; International Journal of Infrared and Millimeter Waves, **12**, 677–682, 1991.
- Illingworth A. J., R. J. Hogan, E. J. OConnor, D. Bouniol, M. E. Brooks, J. Delanoë, D. P. Donovan, J. D. Eastment, N. Gaussiat, J. W. F. Goddard, M. Haeffelin, H. K. Baltink, O. A. Krasnov, J. Pelon, J.–M. Piriou, A. Protat, H. W. J. Russchenberg, A. Seifert, A. M. Tompkins, G.–J. van Zadelhoff, F. Vinit, U. Willen, D. R. Wilson, and C. L. Wrench: Cloudnet continuous evaluation of cloud profiles in seven operational models using groundbased observations; Bulletin of the American Meteorological Society, **88**, 883–898, 2007.
- IPCC (Intergovernmental Panel on Climate Change). *Contribution of Working Group I to the Fourth Assessment Report of the Intergovernmental Panel on Climate Change, 2007*. Cambridge University Press, England, 2007.
- Khvorostyanov V. I. and J. A. Curry: Terminal velocities of droplets and crystals: power laws with continuous parameters over the size spectrum; Journal of the Atmospheric Science, **59**, 1872–1884, 2002.

- Kneifel S., U. Löhnert, A. Battaglia, S. Crewell, and D. Siebler: Snow scattering signals in ground-based passive microwave radiometer measurements; *Journal of Geophysical Research*, **115**, 2010.
- Köhler, H.: The nucleus in the growth of hygroscopic droplets; *Transactions of the Faraday Society* , **32**, 1152-1161, 1936.
- Kollias P., E. E. Clothiaux, M. A. Miller, B. A. Albrecht, G. L. Stephens, and T. P. Ackerman: Millimetre-wavelength radars, new frontier in atmospheric cloud and precipitation research; *Bulletin of the American Meteorological Society*, 1608–1624, 2007.
- Korolev A. V.: Limitations of the Wegener–Bergeron–Findeisen mechanism in the evolution of mixed-phase clouds; *Journal of the Atmospheric Sciences*, **64**, 3372–3375, 2007.
- Korolev A. V. and I. P. Mazin: Supersaturation of water vapor in clouds; *Journal of the Atmospheric Sciences*, **60**, 2957-2974, 2003.
- Kosarev, A. L., and I. P. Mazin: An empirical model of the physical structure of upper layer clouds; *Atmospheric Research*, **26**, 213-228, 1991.
- Kowalewski S. and G. Peters: Analysis of ZR relations based on LDR signatures within the melting layer; *Journal of Atmospheric and Oceanic Technology*, **27**, 1555-1561, 2010.
- Lhermitte R.: Attenuation and scattering of millimeter wavelength radiation by clouds and precipitation; *Journal of Atmospheric and Oceanic Technology*, **7**, 464–479, 1990.
- Liebe H. J., G. A. Hufford, T. Manabe: A model for the complex permittivity of water at frequencies below 1 THz; *International Journal of Infrared and Millimeter Waves*, **12**, 659-674, 1991.
- Luke, E. and P. Kollias: A high resolution hydrometeor phase classifier based on analysis of cloud radar Doppler spectra; *Proceedings of the 33rd Conference on Radar Meteorology*, Cairns, Australia, American Meteorological Society, 2007.
- Magono C. and C. W. Lee: Meteorological classification of natural snow crystals; *Journal of the Faculty of Science, Hokkaido University*, **2**, 321–335, 1966.
- Marchand R., J. Haynes, G. G. Mace, T. Ackerman, and G. Stephens: A comparison of simulated cloud radar output from the multiscale modeling framework global climate model with CloudSat cloud radar observations; *Journal of Geophysical Research*, **114**, 2009.
- Matrosov, S. Y. and A. J. Heymsfield: Use of Doppler radar to assess ice cloud particle fall velocity size relations for remote sensing and climate studies; *Journal of Geophysical Research*, **105**, 22427–22436, 2000.

- Matrosov S. Y., A. V. Korolev, and A. J. Heymsfield: Profiling cloud ice mass and particle characteristic size from Doppler radar measurements; *Journal of Atmospheric and Oceanic Technology*, **19**, 1003–1018, 2002.
- Melchionna S., M. Bauer, and G. Peters: A new algorithm for the extraction of cloud parameters using multipeak analysis of cloud radar data – first application and preliminary results; *Meteorologische Zeitschrift*, **17**, 613–620, 2008.
- MIRA36–S user documentation. METEK, 2006.
- Mie, G.: Beitrage zur Optik trüber Medien, speziell kolloidaler Metallösungen; *Annalen der Physik*, **30**, 377–442, 1908.
- Mitchell D. L.: Use of mass– and area–dimensional power laws for determining precipitation particle terminal velocities; *Journal of the Atmospheric Science*, **53**, 1710–1723, 1996.
- Mossop S.: Production of secondary ice particles during the growth of graupel by riming; *Quarterly Journal of the Royal Meteorological Society*, **102**, 45–57, 1976.
- Mossop S.: The influence of drop size distribution on the production of secondary ice particles during graupel growth; *Quarterly Journal of the Royal Meteorological Society*, **104**, 323–330, 1978.
- Mossop S.: The origin and concentration of ice crystals in clouds. *Bulletin of the American Meteorological Society*, **66**, 264–273, 1985.
- Mossop S. and J. Hallett: Ice crystal concentration in cumulus clouds: influence of the drop spectrum; *Science*, **186**, 632–634, 1974.
- Orr, B. W. and R. A. Kropfli: A method for estimating particle fall velocities from vertically pointing Doppler radar; *Journal of Atmospheric and Oceanic Technology*, **16**, 29–37, 1999.
- Peters G.: Fallgeschwindigkeitsverteilung in ruhender Luft (Fall velocity distribution in still air); in: METEK and ZIB, AiF-Projekt KLARA, KLAssifikation von WolkenRADarsignalen. Gemeinsamer abschlussbericht, 2009.
- G. Peters. *Phase noise or “in-band” dynamic range of a magnetron Doppler radar*. Technical note, 2009.
- G. Peters. *Expressing the spectral reflectivity factor by measured variables and the radar calibration constant*. Technical note, 2010
- H. R. Pruppacher and J. D. Klett. *Microphysics of clouds and precipitation*, 2nd edn. Kluwer Academic, 1997.

- Rambukkange M. P., J. Verlinde, E. W. Eloranta, C. J. Flynn, and E. E. Clothiaux: Using Doppler spectra to separate hydrometeor populations and analyze ice precipitation in multilayered mixed-phase clouds; *IEEE Geoscience and Remote Sensing Letters*, **8**, 2011.
- Rangno A. L. and P. V. Hobbs: Production of ice particles in clouds due to aircraft penetrations; *Journal of Climate and Applied Meteorology*, **22**, 214-232, 1983.
- H. Russchenberg and R. Boers. *Radar sensor synergy for cloud studies; case study of water clouds*. In: *Weather Radar; Principles and Advanced Applications*. P. Meischner ed., 2003.
- Seifert A. and K. D. Beheng: A two-moment cloud microphysics parametrization for mixed-phase clouds. Part 1: Model description; *Meteorology and Atmospheric Physics*, **92**, 45–66, 2006.
- Shupe M. D., P. Kollias, S. Y. Matrosov, and T. L. Schneider: Deriving mixed-phase cloud properties from Doppler radar spectra; *Journal of Atmospheric and Oceanic Technology*, **21**, 660-670, 2004.
- Shupe M. D., J. S. Daniel, G. De Boer, E. W. Eloranta, P. Kollias, C. N. Long, E. Luke, D. D. Turner, and J. Verlinde: A focus on mixed-phase clouds: The status of ground-based observational methods; *Bulletin of the American Meteorological Society*, **87**, 1549–1562, 2008.
- M. I. Skolnik. *Radar Handbook*, 2nd edn. McGraw-Hill, 1990.
- Smith P. L.: Equivalent radar reflectivity factors for snow and ice particles; *Journal of Climate and Applied Meteorology*, **23**, 1258-1260, 1984.
- Spek A. L. J., C. M. H. Unal, D. N. Moisseev, H. W. J. Russchenberg, V. Chandrasekar, Y. Dufournet: A new technique to categorize and retrieve the microphysical properties of ice particles above the melting layer using radar dual-polarization spectral analysis; *Journal of Atmospheric and Oceanic Technology*, **25**, 482–497, 2008.
- Stephens G. L., S. C. Tsay, P. W. Stackhouse Jr., and P. J. Flatau: The relevance of the microphysical and radiative properties of cirrus clouds to climate and climatic feedback; *Journal of Atmospheric Science*, **47**, 1742-1753, 1990.
- Stephens G. L., D. G. Vane, R. J. Boain, G. G. Mace, K. Sassen, Z. Wang, A. J. Illingworth, E. J. O'Connor, W. B. Rossow, S. L. Durden, S. B. Miller, R. P. Austin, A. Benedetti, C. Mitrescu, and the CloudSat Science Team: The CloudSat mission and the A-Train: a new dimension of space-based observations of clouds and precipitation; *Bulletin of the American Meteorological Society*, **83**, 1771–1790, 2002.

- Verlinde J., J. Y. Harrington, G. M. McFarquhar, V. T. Yannuzzi, A. Avramov, S. Greenberg, N. Johnson, G. Zhang, M. R. Poellot, J. H. Mather, D. D. Turner, E. W. Eloranta, B. D. Zak, A. J. Prenni, J. S. Daniel, G. L. Kok, D. C. Tobin, R. Holz, K. Sassen, D. Spangenberg, P. Minnis, T. P. Tooman, M. D. Ivey, S. J. Richardson, C. P. Bahrmann, M. Shupe, P. J. DeMott, A. J. Heymsfield, and R. Scholfield: The Mixed-Phase Arctic Cloud Experiment; *Bulletin of the American Meteorological Society*, **88**, 205-221, 2007.
- Wakasugi K., A. Mizutani, M. Matsuo, S. Fukao, and S. Kato: A direct method for deriving Drop-Size Distribution and vertical air velocities from VHF Doppler radar spectra; *Journal of Atmospheric and Oceanic Technology*, **3**, 623–629, 1986.
- Wallace J. M. and P. V. Hobbs. *Atmospheric science: an introductory survey*, 2nd edn. Academic Press, 1996.
- A. Wegener. *Thermodynamik der Atmosphäre (in German)*. Leipzig, J. A. Barth, 1911.
- Wulfmeyer V., A. Behrendt, H.-S. Bauer, C. Kottmeier, U. Corsmeier, A. Blyth, G. Craig, U. Schumann, M. Hagen, S. Crewell, P. Di Girolamo, C. Flamant, M. Miller, A. Montani, S. Mobbs, E. Richard, M. W. Rotach, M. Arpagaus, H. Russchenberg, P. Schlüssel, M. König, V. Gärtner, R. Steinacker, M. Dorninger, D. D. Turner, T. Weckwerth, A. Hense, and C. Simmer: The Convective and Orographically-induced Precipitation Study: a research and development project of the World Weather Research Program for improving quantitative precipitation forecasting in low-mountain regions. *Bulletin of the American Meteorological Society*, **89(10)**, 1477–1486, 2008.
- K. C. Young. *Microphysical processes in clouds*. New York, Oxford University Press, 1993.
- Zawadzki I., F. Fabry, and W. Szyrmer: Observations of supercooled water and secondary ice generation by a vertically pointing X-band Doppler radar; *Atmospheric Research*, **59-60**, 343-359, 2001.

